Energy, Environment, and Sustainability
Series Editor: Avinash Kumar Agarwal

Akhilendra Pratap Singh
Pravesh Chandra Shukla
Joonsik Hwang
Avinash Kumar Agarwal *Editors*

Simulations and Optical Diagnostics for Internal Combustion Engines

Current Status and Way Forward

Springer

Energy, Environment, and Sustainability

Series Editor

Avinash Kumar Agarwal, Department of Mechanical Engineering, Indian Institute of Technology Kanpur, Kanpur, Uttar Pradesh, India

This books series publishes cutting edge monographs and professional books focused on all aspects of energy and environmental sustainability, especially as it relates to energy concerns. The Series is published in partnership with the International Society for Energy, Environment, and Sustainability. The books in these series are edited or authored by top researchers and professional across the globe. The series aims at publishing state-of-the-art research and development in areas including, but not limited to:

- Renewable Energy
- Alternative Fuels
- Engines and Locomotives
- Combustion and Propulsion
- Fossil Fuels
- Carbon Capture
- Control and Automation for Energy
- Environmental Pollution
- Waste Management
- Transportation Sustainability

More information about this series at http://www.springer.com/series/15901

Akhilendra Pratap Singh ·
Pravesh Chandra Shukla ·
Joonsik Hwang · Avinash Kumar Agarwal
Editors

Simulations and Optical Diagnostics for Internal Combustion Engines

Current Status and Way Forward

Springer

Editors
Akhilendra Pratap Singh
Department of Mechanical Engineering
Indian Institute of Technology Kanpur
Kanpur, Uttar Pradesh, India

Pravesh Chandra Shukla
Department of Mechanical Engineering
Indian Institute of Technology Bhilai
Bhilai, Chhattisgarh, India

Joonsik Hwang
Sandia National Laboratory
Livermore, CA, USA

Avinash Kumar Agarwal
Department of Mechanical Engineering
Indian Institute of Technology Kanpur
Kanpur, Uttar Pradesh, India

ISSN 2522-8366 ISSN 2522-8374 (electronic)
Energy, Environment, and Sustainability
ISBN 978-981-15-0334-4 ISBN 978-981-15-0335-1 (eBook)
https://doi.org/10.1007/978-981-15-0335-1

This Springer imprint is published by the registered company Springer Nature Singapore Pte Ltd.
The registered company address is: 152 Beach Road, #21-01/04 Gateway East, Singapore 189721, Singapore

Preface

Energy demand has been rising remarkably due to increasing population and urbanization. Global economy and society are significantly dependent on energy availability because it touches every facet of human life and activities. Transportation and power generation are two major examples. Without transportation by millions of personalized and mass transport vehicles and availability of 24×7 power, human civilization would not have reached contemporary living standards.

The International Society for Energy, Environment and Sustainability (ISEES) was founded at Indian Institute of Technology Kanpur (IIT Kanpur), India, in January 2014 with an aim to spread knowledge/awareness and catalyze research activities in the fields of energy, environment, sustainability and combustion. The Society's goal is to contribute to the development of clean, affordable and secure energy resources and a sustainable environment for the society and to spread knowledge in the above-mentioned areas and create awareness about the environmental challenges, which the world is facing today. The unique way adopted by the society was to break the conventional silos of specialications (engineering, science, environment, agriculture, biotechnology, materials, fuels, etc.) to tackle the problems related to energy, environment and sustainability in a holistic manner. This is quite evident by the participation of experts from all fields to resolve these issues. The ISEES is involved in various activities such as conducting workshops, seminars and conferences in the domains of its interests. The society also recognizes the outstanding works done by the young scientists and engineers for their contributions in these fields by conferring them awards under various categories.

Third International Conference on "Sustainable Energy and Environmental Challenges" (III-SEEC) was organized under the auspices of ISEES from December 18–21, 2018, at Indian Institute of Technology Roorkee. This conference provided a platform for discussions between eminent scientists and engineers from various countries including India, USA, Norway, Finland, Sweden, Malaysia, Austria, Hong Kong, Bangladesh and Australia. In this conference, eminent speakers from all over the world presented their views related to different aspects of energy, combustion, emissions and alternative energy resource for sustainable development and cleaner environment. The conference presented five high voltage

plenary talks from globally renowned experts on topical themes, namely "The Evolution of Laser Ignition Over more than Four Decades" by Prof. Ernst Wintner, Technical University of Vienna, Austria; "Transition to Low Carbon Energy Mix for India", Dr. Bharat Bhargava, ONGC Energy Center; "Energy Future of India," by Dr. Vijay Kumar Saraswat, Hon. Member (S&T) NITI Aayog, Government of India; "Air Quality Monitoring and Assessment in India" by Dr. Gurfan Beig, Safar and "Managing Large Technical Institutions and Assessment Criterion for Talent Recruitment and Retention" by Prof. Ajit Chaturvedi, Director, IIT Roorkee.

The conference included 24 technical sessions on topics related to energy and environmental sustainability including five plenary talks, 27 keynote talks and 15 invited talks from prominent scientists, in addition to 84 contributed talks and 50 poster presentations by students and researchers. The technical sessions in the conference included Advances in IC Engines, Solar Energy, Environmental Biotechnology, Combustion, Environmental Sustainability, Coal and Biomass Combustion/ Gasification, Air and Water Pollution, Biomass to Fuels/Chemicals, Combustion/Gas Turbines/Fluid Flow/Sprays, Energy and Environmental Sustainability, Atomization and Sprays, Sustainable Transportation and Environmental Issues, New Concepts in Energy Conservation, Waste to Wealth. One of the highlights of the conference was the Rapid Fire Poster Sessions in (i) Engine/Fuels/Emissions, (ii) Renewable and Sustainable Energy and (iii) Biotechnology, where 50 students participated with great enthusiasm and won many prizes in a fiercely competitive environment. 200+ participants and speakers attended this four-day conference, which also hosted Dr. Vijay Kumar Saraswat, Hon. Member (S&T) NITI Aayog, Government of India, as the chief guest for the book release ceremony, where 14 ISEES books published by Springer, Singapore, under a special dedicated series "Energy, environment and sustainability" were released. This was the second time in a row that such significant and high-quality outcome has been achieved by any society in India. The conference concluded with a panel discussion on "Challenges, Opportunities and Directions for National Energy Security," where the panelists were Prof. Ernst Wintner, Technical University of Vienna, Prof. Vinod Garg, Central University of Punjab, Bhatinda; Prof. Avinash Kumar Agarwal, IIT Kanpur; and Dr. Michael Sauer, Boku Univ. fo Natural resources, Austria. The panel discussion was moderated by Prof. Ashok Pandey, Chairman, ISEES. This conference laid out the road map for technology development, opportunities and challenges in energy, environment and sustainability domain. All these topics are very relevant for the country and the world in the present context. We acknowledge the support received from various funding agencies and organizations for the successful conduct of the third ISEES conference III-SEEC, where these books germinated. We would therefore like to acknowledge NIT Srinagar, Uttarakhand (TEQIP) (Special thanks to Prof. S. Soni, Director, NIT, UK), SERB, Government of India (Special thanks to Dr. Rajeev Sharma, Secretary); UP Bioenergy Development Board, Lucknow (Special thanks to Sh. P. S. Ojha), CSIR and our publishing partner Springer (Special thanks to Swati Meherishi).

The editors would like to express their sincere gratitude to a large number of authors from all over the world for submitting their high-quality work in a timely manner and revising it appropriately at a short notice. We would like express our

special thanks to Dr. Atul Dhar, Dr. Pravesh Chandra Shukla, Dr. Nirendra Nath Mustafi, Prof. V. S. Moholkar, Prof. V. Ganeshan, Dr. Joonsik Hwang, Dr. Biplab Das and Dr. Veena Chaudhary, Dr. Jai Gopal Gupta, Dr. Chetan Patel, who reviewed various chapters of this monograph and provided their valuable suggestions to improve the manuscripts.

This book is based on combustion simulations and optical diagnostics techniques, which are currently used in internal combustion engines. This book includes a variety of simulation techniques including in-cylinder combustion, numerical investigations of fuel spray and effects of different fuels and engine technologies. This book includes a few chapters on alternative fuels such as DEE, biomass and alcohols which provides valuable information related to alternative fuel utilization in IC engines. Few chapters based on the use of combustion simulations and optical techniques in advanced techniques such as microwave-assisted plasma ignition and laser ignition are another important aspect of this book. Chapters include recent results and more focussed on current trends of the automotive sector. In this book, readers will get the idea about the combustion simulations and optical diagnostics, which will help them in analyzing various issues related to in-cylinder combustion, pollutant formation and alternative fuels. Few chapters of this book are based on a review of state-of-the-art models for combustion, with special focus on the theory, development and applications of these combustion models in internal combustion systems. We hope that the book would be of great interest to the professionals, postgraduate students involved in fuels, IC engines, engine instrumentation and environmental research.

Kanpur, India — Akhilendra Pratap Singh
Bhilai, India — Pravesh Chandra Shukla
Livermore, CA, USA — Joonsik Hwang
Kanpur, India — Avinash Kumar Agarwal

Contents

Part I General

1 Introduction to Combustion Simulations and Optical Diagnostic Techniques for Internal Combustion Engines 3
Akhilendra Pratap Singh, Pravesh Chandra Shukla, Joonsik Hwang and Avinash Kumar Agarwal

Part II Simulations in Internal Combustion Engines

2 Modelling Aspects for Adaptation of Alternative Fuels in IC Engines 9
Hardikk Valera, Dhananjay Kumar, Akhilendra Pratap Singh and Avinash Kumar Agarwal

3 Simulation and Optical Diagnostics for Internal Combustion Engines 27
Koji Yasutomi, Tsukasa Hori and Jiro Senda

4 Numerical Investigations on Water-Ethanol-Diesel Emulsified Fuel 37
Rabinder Singh Bharj, Vishal Vasistha, Narinder Singh and Gurkamal Nain Singh

Part III Optical Diagnostics in IC Engines

5 Optical Diagnostics of Spray Development in Diesel Engines 53
Ashutosh Jena

6 Investigation of Influence of Injection Pressure on Gasoline Fuel Spray Characteristics Using Numerical Simulation 69
Sandip Wadekar

7 Cavitation in Injectors: A Brief Review of the Diagnostics of Liquid-Vapour Flow Within Injector Nozzles 85
Aditya Saurabh

8 Multiphase Phenomena in Diesel Fuel Injection Systems 95
Ioannis K. Karathanassis, Foivos (Phoevos) Koukouvinis and Manolis Gavaises

Part IV Miscellaneous

9 Improvement of Flame Kernel Growth by Microwave-Assisted Plasma Ignition 129
Joonsik Hwang, Wooyeong Kim and Choongsik Bae

10 Laser Ignition Technology for Gaseous Fuelled Automotive Engines 143
Dhananjay Kumar and Avinash Kumar Agarwal

Editors and Contributors

About the Editors

Dr. Akhilendra Pratap Singh is working at IIT Kanpur. He received his Masters and Ph.D. in Mechanical Engineering from Indian Institute of Technology Kanpur, India, in 2010 and 2016, respectively. His areas of research include advanced low-temperature combustion; optical diagnostics with special reference to engine endoscopy and PIV; combustion diagnostics; engine emissions measurement; particulate characterization and their control; and alternative fuels. Dr. Singh has edited seven books and authored 21 book chapters, 40 research articles in international journals and conferences. He has been awarded "ISEES Best Ph.D. Thesis Award" (2017), "SERB Indo-US Postdoctoral Fellowship" (2017) and "IEI Young Engineer Award" (2017). He is a member of numerous professional societies, including SAE, ASME and ISEES.

Dr. Pravesh Chandra Shukla is Assistant Professor in the Department of Mechanical Engineering at Indian Institute of Technology Bhilai. Dr. Shukla received his PhD from Indian Institute of Technology Kanpur. Prior to joining IIT Bhilai, he was a postdoctoral researcher in the Division of Combustion Engines, Department of Energy Sciences, Lund University, Sweden. He briefly worked in Ecole Centrale de Nantes, France, in the field of dual-fuel combustion. He is a recipient of Young Scientist Award from the International Society for Energy, Environment and Sustainability. Dr. Shukla mainly works in the field of Internal Combustion Engines and Alternative fuels for transportation. He worked on the development of additives for high compression ratio heavy duty engines fueled with alcohol. He is involved in investigating the emission characteristics for alternative fuels like biodiesel, HVO and alcohols for conventional and advanced heavy duty compression ignition engines. During his doctoral, he was mainly involved in physico-chemical characterization of diesel engine exhaust using non-noble metal-based mixed oxides diesel oxidation catalysts. Till now, he has published more than 24 technical articles in international journals and conference proceedings.

Dr. Joonsik Hwang is currently a postdoctoral fellow in Sandia National Laboratory, USA. He received his Masters and Ph.D. in Mechanical Engineering from Korea Advanced Institute of Science and Technology (KAIST), Daejeon, Korea. His areas of research include advanced low-temperature combustion; combustion diagnostics; spray and combustion characteristics; particulate characterization; and alternative fuels. Dr. Hwang has published more than 25 research articles in international journals and conferences. He has been awarded “ISEES Best Ph.D. Thesis Award” (2017) and several travel fellowship awards.

Prof. Avinash Kumar Agarwal joined IIT Kanpur in 2001. He worked at the Engine Research Center, UW-Madison, USA, as a postdoctoral fellow (1999 – 2001). His interests are IC engines, combustion, alternate and conventional fuels, lubricating oil tribology, optical diagnostics, laser ignition, HCCI, emissions and particulate control and large bore engines. Prof. Agarwal has published 270+ peer-reviewed international journal and conference papers, 35 edited books, 63 books chapters and has 7850+ Scopus and 11900+ Google scholar citations. He is associate editor of ASME Journal of Energy Resources Technology. He has edited "Handbook of Combustion" (5 Volumes; 3168 pages), published by Wiley–VCH, Germany. Prof. Agarwal is a Fellow of SAE (2012), Fellow of ASME (2013), Fellow of NASI (2018), Fellow of Royal Society of Chemistry (2018), Fellow of ISEES (2015) and Fellow of INAE (2015). He is a recipient of several prestigious awards such as Clarivate Analystics India Citation Award-2017 in Engineering and Technology, NASI-Reliance Industries Platinum Jubilee Award-2012; INAE Silver Jubilee Young Engineer Award-2012; Dr. C. V. Raman Young Teachers Award: 2011; SAE Ralph R. Teetor Educational Award -2008; INSA Young Scientist Award-2007; UICT Young Scientist Award-2007; and INAE Young Engineer Award-2005. Prof. Agarwal received Prestigious Shanti Swarup Bhatnagar Award-2016 in Engineering Sciences.

Contributors

Avinash Kumar Agarwal Engine Research Laboratory, Department of Mechanical Engineering, Indian Institute of Technology Kanpur, Kanpur, India

Choongsik Bae Department of Mechanical Engineering, Korea Advanced Institute of Science and Technology (KAIST), Daejeon, Republic of Korea

Rabinder Singh Bharj Department of Mechanical Engineering, Dr. B. R. Ambedkar, National Institute of Technology, Jalandhar, India

Manolis Gavaises School of Mathematics, Computer Science & Engineering, Northampton Square, City, University of London, London, UK

Joonsik Hwang Sandia National Laboratory, Albuquerque, CA, USA; Department of Mechanical Engineering, Korea Advanced Institute of Science and Technology (KAIST), Daejeon, Republic of Korea

Ashutosh Jena Department of Mechanical Engineering, Indian Institute of Technology Kanpur, Kanpur, UP, India

Ioannis K. Karathanassis School of Mathematics, Computer Science & Engineering, Northampton Square, City, University of London, London, UK

Wooyeong Kim Department of Mechanical Engineering, Korea Advanced Institute of Science and Technology (KAIST), Daejeon, Republic of Korea

Foivos (Phoevos) Koukouvinis School of Mathematics, Computer Science & Engineering, Northampton Square, City, University of London, London, UK

Dhananjay Kumar Engine Research Laboratory, Department of Mechanical Engineering, Indian Institute of Technology Kanpur, Kanpur, India

Aditya Saurabh Department of Mechanical Engineering, Indian Institute of Technology Kanpur, Kanpur, India

Jiro Senda Doshisha University, Kyoto, Japan

Pravesh Chandra Shukla Department of Mechanical Engineering, Indian Institute of Technology Bhilai, Raipur, India

Akhilendra Pratap Singh Engine Research Laboratory, Department of Mechanical Engineering, Indian Institute of Technology Kanpur, Kanpur, India

Gurkamal Nain Singh Department of Mechanical Engineering, Dr. B. R. Ambedkar, National Institute of Technology, Jalandhar, India

Narinder Singh Department of Mechanical Engineering, Dr. B. R. Ambedkar, National Institute of Technology, Jalandhar, India

Tsukasa Hori Osaka University, Suita, Osaka, Japan

Hardikk Valera Engine Research Laboratory, Department of Mechanical Engineering, Indian Institute of Technology Kanpur, Kanpur, India

Vishal Vasistha Department of Mechanical Engineering, Dr. B. R. Ambedkar, National Institute of Technology, Jalandhar, India

Sandip Wadekar Chalmers University of Technology, Gothenburg, Sweden

Koji Yasutomi Hino Motors Ltd., Tokyo, Japan

Part I
General

Chapter 1
Introduction to Combustion Simulations and Optical Diagnostic Techniques for Internal Combustion Engines

Akhilendra Pratap Singh, Pravesh Chandra Shukla, Joonsik Hwang and Avinash Kumar Agarwal

Abstract In the last few decades, application of advanced combustion technologies, engine design modifications, after-treatment techniques, etc. have improved engine performance and reduced exhaust emissions. However, advancement in technologies introduced a large number of parameters, which need to be optimised for satisfactory results. This increases the system complexity therefore it become very difficult to perform experiments for optimization of each parameter. In recent years, simulation techniques have shown their potential to resolve this issue. Simulation techniques can optimize such complex systems and provide optimized solution with less effort involvement. Optical diagnostic techniques are the other important area for internal combustion engines. These techniques can provide information about in-cylinder conditions, spray parameters, fuel-air mixing and combustion, which is not possible with conventional techniques. This book is based on these simulation and optical diagnostic techniques and provides case studies to resolve several technical issues involved with internal combustion engines. Few chapters based on advanced topics such as microwave-assisted plasma ignition, laser ignition, etc. are the important aspect of this book. Chapters are based on review of state-of-the-art models for combustion, with special focus on the theory, development and applications of these combustion models in internal combustion systems make this book suitable for researchers, working in the area of alternative fuels and advanced combustion techniques.

Keywords Combustion simulations · Optical diagnostics · Fuel spray · Numerical techniques · Advanced combustion techniques

A. P. Singh · A. K. Agarwal (✉)
Department of Mechanical Engineering, Indian Institute of Technology Kanpur, Kanpur, India
e-mail: akag@iitk.ac.in

P. C. Shukla
Department of Mechanical Engineering, Indian Institute of Technology Bhilai, Raipur, India

J. Hwang
Sandia National Laboratory, Albuquerque, CA, USA

A. P. Singh et al. (eds.), *Simulations and Optical Diagnostics for Internal Combustion Engines*, Energy, Environment, and Sustainability,
https://doi.org/10.1007/978-981-15-0335-1_1

Rapid depletion of petroleum and associated environmental pollution lead to sustainability issues for internal combustion (IC) engines. Various techniques such as advanced combustion techniques, alternative fuels, aftertreatment devices, etc. have successfully reduced exhaust emissions from IC engines however, these techniques are complex and have several limitations (Singh and Agarwal 2018). It is very difficult to perform IC engine experiments using all these techniques to optimize the combustion, performance and emission characteristics simultaneously because this is a time consuming process. Lack of understanding of different in-cylinder processes such as fuel spray evolution, fuel-air mixing, etc. also play important role in engine performance. Therefore, it become necessary to take these processes into consideration during performance and emission optimization. These processes can be investigated using different optical diagnostic techniques. This book is focussed on all such techniques including simulations and optical diagnostics. This book has been divided into four sections, starting with introduction chapter as first section.

Second section of this book is based on simulation techniques. First chapter of this section gives an idea about the simulation technique in internal combustion engines. Inclusion of strategies for adaptation of alternative fuels such as methanol, ethanol, biodiesel, etc. makes this chapter more important for IC engine researchers. Discussion about the design aspects of the after-treatment devices is another important aspect of this chapter by which better emission results can be achieved from IC engines. This chapter discusses about the modelling aspects in the entire complex engine system by discussing the critical components of the system comprehensively. Second chapter of this section emphasizes on the application of modelling and optical diagnostic techniques for IC engines. In this chapter, a droplet breakup model has been developed and optimized under non-evaporative diesel spray with a large-eddy simulation. This chapter describes about a hybrid breakup model, which combines the Kelvin–Helmholtz and modified Taylor analogy breakup model, which are used for the primary and secondary breakup models, respectively. For validating these models, spray simulations were performed under non-evaporative condition and results showed a good agreement with the simulation results of Kelvin–Helmholtz–Modified Taylor analogy breakup models. Third chapter of this section discusses about the emulsified fuel technology for reducing the pollutant emitted from IC engines and to slow down the rate of conventional fuel consumption. This technology is based on blending of water or some other alternative fuel such as alcohols in conventional fuel. This technology has significant impact on oxides of nitrogen (NOx) and particulate matter (PM) reduction. This chapter presents the numerical analysis of emulsified fuel utilization in compression ignition (CI) engines.

Third section of this book is based on different optical diagnostic techniques used for spray investigations in CI and spark ignition (SI) engines. First chapter of this section discusses about the development of spray in CI engines. Main objective of this chapter is to emphasize on fuel spray impingement on the cylinder wall and piston top because it affects hydrocarbon (HC) and PM emissions. This chapter reviews several experimental investigations such as phase Doppler interferometry (PDI), spray imaging etc. to get idea about different physical processes involved with fuel spray in a diesel engine. Second chapter in based on spray evolution in a

gasoline direct injection (GDI) engine. Main objective of this chapter is to investigate the effects of fuel injection pressure (FIP) on spray characteristics because spray characteristics at high FIPs affect engine performance and emission characteristics. This chapter presents a combined investigation using both simulation as well experimental techniques. Simulation experiments were performed in an optical accessible constant volume chamber and results were analysed using large-eddy simulation (LES) method and a standard Lagrangian spray model. The fuel spray atomization was modelled using the Kelvin Helmholtz–Rayleigh Taylor (KH-RT) model, and droplet size distribution followed the Rosin-Rammler distribution function. For validating the simulation results, results such as liquid penetration length of spray, the mean droplet sizes such as arithmetic mean diameter and Sauter mean diameter (SMD) of the spray droplets were compared with the measured droplet sizes as a function of pressure. Third chapter of this section shows the cavitation process, which is a common phenomenon of high pressure fuel injectors. This chapter presents both the advantages as well as disadvantages of cavitation process. This chapter reviews different studies related to cavitation process and emphasizes the importance of this process in fuel spray. Last chapter of this section discusses about the complexity involved with the fuel injection equipment's of modern CRDI system. The operation of these devices is highly unsteady, involving moving geometries such as needle valves. Phase change or transition from subcritical to transcritical/supercritical state of matter is another difficulty involved with fuel injectors. This chapters deals with all these issues and discusses the techniques to resolve these issues.

Last section of this book includes two chapters covering two different aspects related to IC engines. First chapter is based on development of laser ignition (LI) technology for multi-cylinder engines, which can deliver higher engine efficiency and has potential to reduce harmful gaseous emissions such as NOx (Agarwal et al. 2017). This chapter emphasizes the application of laser ignition technology in gaseous fuelled engines and adaptation in for implementation in automotive sector. LI technology is capable of igniting leaner fuel-air mixture which is not possible by conventional spark plugs. Second chapter is based on flame kernel growth by microwave-assisted plasma ignition (MSPI). This chapter describes the application of non-thermal plasma ignition system, which seems to be a promising path to develop efficient and clean gasoline vehicles. This chapter presents different aspects involved in the development of microwave-assisted plasma ignition with customized electric components and igniter. Inclusion of high-speed shadowgraph imaging and hydroxyl ($^{-}$OH) radical imaging under various air-fuel ratio, ambient pressure, and ignition strategy conditions are another important aspect of this chapter.

Specific topics covered in the monograph include:

- Introduction to combustion simulations and optical diagnostic techniques for internal combustion engines
- Engine modelling aspects for adaption of alternative fuel
- Advanced techniques for combustion simulations and optical diagnostics in internal combustion engines
- Numerical investigations on water-ethanol-diesel emulsified fuel

- Optical diagnostics of spray development in diesel engines
- Investigation of influence of injection pressure on gasoline fuel spray characteristics using numerical simulation
- Cavitation in Injectors: A brief review of the diagnostics of liquid-vapour flow within injector nozzles
- Multiphase Phenomena in Diesel Fuel Injection Systems
- Laser ignition technology for gaseous fuelled auto-motive engines
- Improvement of flame kernel growth by microwave-assisted plasma ignition.

The topics are organized in four different sections: (i) General, (ii) Simulations in Internal Combustion Engines, (iii) Optical Diagnostics in IC Engines, and (iv) Miscellaneous.

References

Agarwal AK, Singh AP, Pal A (2017) Effect of laser parameters and compression ratio on particulate emissions from a laser ignited hydrogen engine. Int J Hydrogen Energy 42(15):10622–10635

Singh AP, Agarwal AK (2018) Evaluation of fuel injection strategies for biodiesel-fueled CRDI engine development and particulate studies. J Energy Res Technol 140(10):102201

Part II
Simulations in Internal Combustion Engines

Chapter 2
Modelling Aspects for Adaptation of Alternative Fuels in IC Engines

Hardikk Valera, Dhananjay Kumar, Akhilendra Pratap Singh and Avinash Kumar Agarwal

Abstract Deteriorating environment and stricter emission norms are motivating researchers for finding sustainable transport solutions. Researchers are focusing on two approaches namely adaptation of alternative fuels, and exhaust gas after-treatment. Utilization of alternate fuels such as methanol, ethanol, and biodiesel etc. in internal combustion (IC) engines reduces inherent chemical components present in conventional fossil fuels. These chemical species are a major source of harmful pollutants such as particulate matter (PM), polycyclic aromatic hydrocarbons (PAHs), PM bound trace metals, etc. Advancement in after-treatment technologies such as optimization of hexagonal cells of substrate, use of noble metals, etc. are also effective in reducing pollutants from engine tail-pipe. However, developments for adaptation of these technologies in existing engines is a challenging task. For adaptation of any alternative fuel, engine components need to be modified according to fuel properties. However, optimization of design parameters of thousands of engine components is a tedious task, which cannot be done experimentally. This can be done easily using modelling techniques, in which a prototype engine can be developed to investigate the effect of engine design parameters and fuel properties on the engine performance and emission characteristics. In last few years, 1-D and 3-D simulation tools have been extensively explored for engine design and performance optimization. This chapter discusses basic modelling techniques, which can be used for engine research. This chapter also presents heat transfer models, which are important for in-cylinder combustion analysis. Few fluid-flow models have also been discussed in this chapter, which are mainly used for in-cylinder air-flow investigations, fuel flow in the fuel injection system, etc. Overall, this chapter discusses modelling aspects related to engine design so that alternative fuels can be adapted.

Keywords Transportation sector · Engines · Modelling · 1-D modelling · 3-D modelling

H. Valera · D. Kumar · A. P. Singh · A. K. Agarwal (✉)
Engine Research Laboratory, Department of Mechanical Engineering, Indian Institute of Technology Kanpur, Kanpur 208016, India
e-mail: akag@iitk.ac.in

A. P. Singh et al. (eds.), *Simulations and Optical Diagnostics for Internal Combustion Engines*, Energy, Environment, and Sustainability,
https://doi.org/10.1007/978-981-15-0335-1_2

2.1 Introduction

Internal combustion (IC) engines are primary choice for transport sector due to their proven durability, reliability, cost, and user friendliness. Now-a-days, new technologies such as electric vehicles (EVs), hybrid vehicles, etc. have been introduced in transport sector, however, these vehicles have certain limitations such as cost, complexity, limited range, etc. Therefore, IC engines still are the main choice in the transport sector. Since last few decades, IC engines are facing bad press because of energy security and environmental issues. To resolve these issues, IC engines have changed remarkably due to advancement in engine technologies, introduction of new fuels and development of emission compliance technologies. Development of oxidation catalysts for SI engines reduced carbon monoxide (CO) emission significantly. Introduction of three-way catalytic (TWC) converter reduced the toxic exhaust gases hydrocarbons (HC), oxides of nitrogen (NO_X), and CO emissions. However, these interventions are not enough for meeting upcoming emission norms.

Rapidly depleting fossil fuels and continuously increasing demand for these fossil fuels are the other challenges. International Energy Agency (IEA) reported that demand for petroleum may increase by 20% by 2035 compared to 2010 (Statistics by International Energy Agency 2018). In such a critical situation, automotive industry is desperately looking for alternative energy sources, which would improve ambient air quality, reduce greenhouse gas (GHG) emissions and contribute to national energy security (Knothe 2010; https://www.e-education.psu.edu/egee439/node/684; Agarwal 1998; Agarwal and Das 2001; Urja 2013). Therefore, researchers are exploring sustainable alternative fuels, which can be utilized in new engines as well as existing engines. Design of existing engines is the main constraint for adaption of alternative fuels because current engines are designed to operate on conventional fuels, which have fuel properties quite different from the alternate fuels. Therefore, 100% replacement of fossil fuels with alternate fuels is very challenging. In such a scenario, it is important to modify the design of engine component so that engines fuelled by alternative fuels can be operated efficiently and in an eco-friendly manner. These engine modifications are tedious tasks because an engine consists of hundreds of components. Modelling and simulation techniques make this task relatively easier compared to experimental techniques. Modelling is generally regarded as the process of describing the physical phenomena in a particular model with the help of mathematical equations and solution of these equations predicts the effects of new fuel, without actually performing any engine experiment. Using these techniques, initial effects of alternative fuels on engine performance and emissions can be predicted by making the computational models of the physical process involved in the engine using different simulation tools. Using sophisticated modelling techniques, more extensive analysis is also possible, which helps in understanding various phenomenons such as fuel-air chemical kinetics, fuel sprays, in-cylinder combustion, etc.

In last few decades, engine modelling efforts have primarily concentrated on engine performance improvements and reduction of emissions. There are numerous

modelling studies available in open literature, which show the potential of modelling and simulations in the domain of IC engine research. Initially, researchers used these techniques for preliminary research studies however now-a-days, these techniques are used for solving complex engine problems, which are not solvable by experiments. Some features of modelling techniques are given below:

- Opens the door for exploring solutions, which never appeared in reality.
- Provides opportunity to generate new ideas and takes innovative decisions based on prepared models.
- Helps to understand the effects of proposed solution on each engine parts such as on the piston, cylinder, fuel injection equipment, muffler, etc.
- Provides comparison among different possible solutions using graphics/animations.
- Allows to perform tests on physical models without preparing expensive and complex engine test cells.
- Perform experiments without harming the person or the ambient environment.
- Modelling can show simultaneous effects of new design of different engine parts.

Basic procedure for engine modelling to study the effects of alternative fuels in an IC engine is given below:

Step 1: Conduct the engine experiments using baseline fuel and collect engine performance and emissions data at selected operating conditions.
Step 2: Prepare an engine model in 1-D/3-D simulation softwares and compute the engine performance and emissions data at tested conditions.
Step 3: Validate the computational model using the experimental data. Use calibration procedures, if required.
Step 4: Replace baseline fuel with alternative fuel in the validated engine model to compute the results.
Step 5: Analyse the effects of alternative fuels on engine performance and emissions.

Due to extensive research in IC engines, several commercial simulation softwares such as GT-Power, Converge, and KIVA, etc. are available, which are especially designed for solving problems related to IC engines, combustion and fluid flow. These softwares have a number of modules, which can solve complex problems of IC engines using governing mathematical equations (https://www.gtisoft.com/gt-suite-applications/propulsion-systems/gt-power-engine-simulation-software/, https://convergecfd.com/, https://www.mechanicalbooster.com/2017/10/spark-ignition-engine.html). Currently 1-D and 3-D modelling softwares are the most used simulation tools in the domain of IC engines. 1-D Modelling is used to simulate complex behaviour of entire engine systems as a whole, such as fuel injection system, gas exchange system, turbocharger, etc. On the other hand, 3-D Modelling focuses on a single component of the system (such as cylinder, injector, etc.) without considering their dynamic interaction with other components.

This chapter is based on these two modelling techniques with greater emphasis on 1-D modelling. This chapter includes general description of these modelling

techniques and covers different modelling aspects of the IC engines. Thrust is given on modelling of essential components such as injectors, cylinders, valves, etc. using 1-D modelling. Required comprehensive details for each component has also been discussed. Attention is given to the heat transfer model since it calculates how the heat will transferred to the combustion chamber walls. In the last section, a 1-D model using GT-Power software is demonstrated.

2.2 General Architecture of IC Engines

There are two types of engines used in transportation sector. First type is spark ignition (SI) engines, operating on Otto cycle using a spark plug as an ignition source. SI engines use either carburetor or port fuel injectors for supplying the fuel in the engine intake manifold. Second type is compression ignition (CI) engines in which the engines, operating on diesel cycle and ignition is initiated by high-pressure and temperature generated during the compression stroke. In CI engines, fuel injectors are used to inject fuel directly into combustion chamber. During combustion, chemical energy of fuel is released and transferred as mechanical work to the piston, through which power comes as an output to move the wheels. Fuel supply system is the most important part of an engine, which supplies the required amount of fuel at a certain point of time in each engine cycle.

2.2.1 SI Engine

SI engines require an ignition source such as spark plug, which creates the spark inside the combustion chamber (https://www.mechanicalbooster.com/2017/10/spark-ignition-engine.html). Spark engines use gasoline like fuels (high octane fuels). Working of a typical SI engine is summarized below:

(i) Suction stroke: Air-fuel mixture enters the cylinder.
(ii) Compression stroke: Air-fuel mixture get compressed, resulting in high pressure and temperature.
(iii) Power stroke: Power generation due to combustion of fuel-air mixture.
(iv) Exhaust stroke: Burnt gases evacuate out of the engine.

Generally the fuel is injected via carburetor during the suction stroke, and is shown in Fig. 2.1.

Some essential features of the SI engines are mentioned below:

- The compression ratio of the engine is between 6 and 10.
- Lightweight makes these engines suitable for light-duty applications such as motorcycles and lawnmovers.

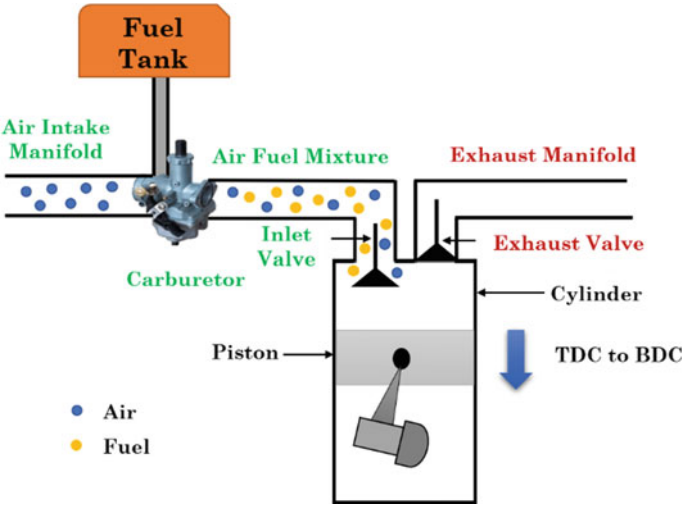

Fig. 2.1 Schematic of a SI engine system

- Higher maximum engine speed can be achieved due to their lightweight construction.
- Fuels having high self-ignition temperature (high octane fuels) are suitable for SI engines.

2.2.2 CI Engine

In CI engines, fuel is ignited due to its injection in the heated and pressurised air at the end of the compression stroke (https://www.howacarworks.com/basics/how-a-diesel-engine-works). In CI engines, diesel like fuels with high cetane numbers are preferred due to their low knock tendency. General working of diesel engines is given below:

(i) Suction stroke: Air enters into the cylinder.
(ii) Compression stroke: Air is compressed, and fuel is directly injected into the cylinder in high temperature and pressure air at the end of the compression stroke.
(iii) Power stroke: Power generation due to combustion of fuel-air mixture.
(iv) Exhaust stroke: Piston pushes the burnt gases out of the engine cylinder.

Generally fuel is injected directly into the combustion chamber through an injector at the end of the compression stroke (Fig. 2.2). Other features of the CI engines are given below:

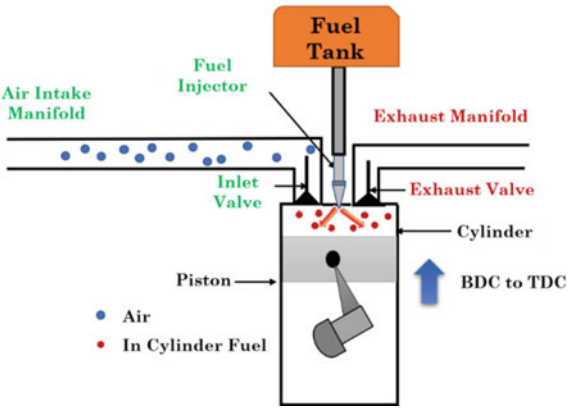

Fig. 2.2 Schematic of a CI engine system

- Compression ratio of the engine is between 14 and 22.
- Heavyweight due to high injection pressure makes it suitable for heavy-duty applications such as buses, trucks and tractors.
- Relatively low engine speeds are preferred due to its heavy-weight construction.
- Fuel having low self-ignition temperature are desirable.

In the next section, modelling of different engine sub-systems are discussed.

2.3 Modelling of IC Engines

The engine consists a large number of components such as fuel injector, cylinder, cranktrain, valves, etc. Each part affects the performance and emission characteristics of the engine. Therefore it is very important to model each part carefully for simulating the engine experiments. Simulation softwares require a set of minimum information about each part before starting the modelling. Next sub-section discusses required critical information about the engine components and explains the modelling aspects of these components.

2.3.1 Fuel Injector

Fuel injector is used to deliver the fuel into the port or into the engine cylinder for powering the engine. Injector contains one needle, which acts as a valve to open or close the injector passage hole through which fuels comes out at certain fuel injection pressure (FIP). Injector nozzle performs two important functions namely fuel atomization and fuel distribution inside the combustion chamber. Fuel distribution is also affected by several other parameters such as FIP, ambient air density at the time of fuel injection, and physical properties of the fuel. High FIP leads

to improved fuel atomization and fuel spray penetration however, high air density inside the combustion chamber results in superior dispersion of fuel. Fuel properties such as vapour pressure, viscosity, and self-ignition temperature also play a vital role in fuel spray characteristics. In a pressure-activated injector, one end is exposed to the fuel pressure, and the another end is exposed to preloaded spring. Needle is in closed condition, when spring force is greater than the fuel pressure. Fuel pump is connected to injectors via a high pressure pipe. Fuel injection starts with upward movement of needle from the needle seat, until the fuel pressure is sufficient to overcome the spring force. In a pneumatically-activated injector, one end is exposed to the fuel pressure, and the other end is connected to the needle. Opening and closing of the needle can be done by changing the hydraulic pressure. Injector modelling requires some essential inputs, as shown in Table 2.1.

2.3.2 Cylinder

Cylinder is the most critical part of engine, which can be sleeved and sleeveless. Sleeved cylinders are lined with a harder metal compared to block metal, and sleeveless cylinders are coated with wear resistant materials. A cylinder's displacement is calculated by multiplying its cross-sectional area and stroke length. Multi-cylinders

Table 2.1 Required inputs for injector modelling

Parameter	Description
Start of injection (SoI)	Time at which fuel injection starts. Usually expressed as crank angle degree (CAD) relative to TDC
End of injection (EoI)	Time at which fuel injection stops. Usually expressed as CAD relative to TDC
Injected fuel mass	Mass of fuel injected into the cylinder. Usually expressed in terms of mg/stroke or mg/cycle
Injection duration	Time period during which fuel is injected into the combustion chamber. Injection duration can be expressed as time difference between EoI and SoI
Injection profile	Fuel injection rate, which can be expressed as injection shape such as boot, ramp, square etc.
Nozzle discharge coefficient	It is a correction factor used to define the actual mass injected into the cylinder
Number of holes	Number of holes available at the nozzle tip
Type of fluid	Diesel, gasoline, methanol, ethanol, etc.
Injected fuel temperature	Temperature of fuel at the time of injection
Nozzle/atomizer hole diameter	Individual nozzle hole diameter
Injector location	In case of port injection, it is the distance between injector and the intake valve/port

displacement is calculated by following the above mentioned procedure and further multiplying with the number of cylinders. Modelling of cylinders is quite complex because it involves the simultaneous motion of several components. Generally, three combustion models are used for cylinder modelling (Hariram and Bharathwaaj 2016).

(i) Zero-dimensional model
(ii) Quasi-dimensional model
(iii) Multi-dimensional model

Zero-dimensional models are the most suitable and simple models for understanding the effects of engine operating parameters on overall heat release rates and in-cylinder pressure. These models use various assumptions and simplifications and do not consider complex flow-field dimensions. Zero-dimensional model is an open system, which generally evaluates the instantaneous in-cylinder combustion characteristics such as pressure, temperature, heat release rate, etc. by utilizing mass and energy conservation equations (Payri et al. 2011). Single composition of the cylinder contents and uniform state is assumed throughout the control volume, which leads to limitation in terms of emission predictions. Overall, this is a good tool for predicting combustion parameters for different engines and operating conditions (Payri et al. 2011). Due to complications of the engine, various input constraints such as injection timing/spark timing, EGR, etc., can not be incorporated in this model, leading to inaccurate predictions. Zero-dimensional models are further classified into single-zone models, two-zone models and multi-zone models (Neshat et al. 2017). Single zone models are the ones, in which working fluid is considered as one thermodynamic system, and energy released from the fuel combustion is calculated by using first law of thermodynamics applied to the system. In two-zone models, the working fluid is considered in two zones, namely burned zone and unburned zone (Fig. 2.3). These zones act like two different thermodynamic systems with energy and mass interactions having common surrounding of cylinder walls. However, two-zone models have several assumptions as mentioned below.

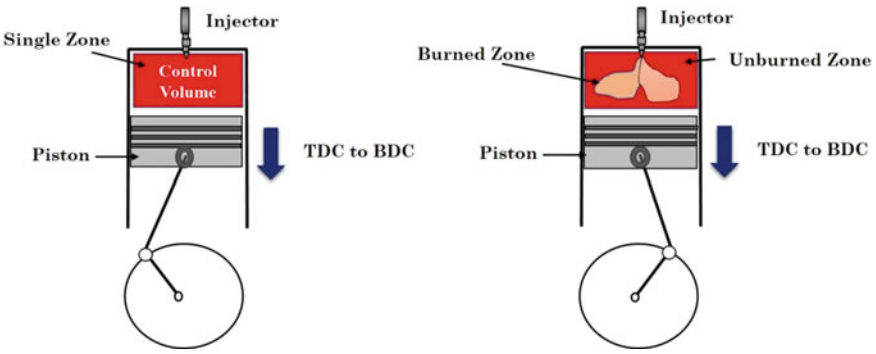

Fig. 2.3 Burned and unburned zones in the engine cylinder

- The burned and unburned zones are modelled as ideal gases with different physical properties.
- Unburned zone is modelled as a premixed fuel-air mixture. Therefore it is more accurate/realistic to model SI engine combustion rather than CI combustion.
- Characteristic gas constants for both zones do not vary with temperature and pressure in the modelling. If it varies up to certain extent, then it is modelled using explicit relationship between gas constant and involved gas properties (T, P, etc.)
- Heat does not transfer from burned to unburned zone and vice versa in modelling.
- Enthalpy of fuel is ignored during modelling, since it is not significant.
- Crevice losses are not considered.
- Instantaneous pressure in both zones is considered to be the same.

Based on the assumptions as mentioned earlier, combustion is modelled in the following manner using two different equations.

1. Cylinder acts like two divided chambers namely burned zone and unburned zone. It also contains residual gases from the previous cycle (https://www.gtisoft.com).
2. As combustion progresses, air-fuel mixture is transferred from the unburned zone to the burned zone. Rate of transfer of air-fuel mixture from unburned zone to burned zone is considered as 'burn rate', which is an important parameter for modelling.
3. Chemical equilibrium calculations start once air-fuel mixture transfers from the unburned zone to the burned zone and calculate thirteen combustion product species, i.e., H_2O, CO_2, N, O, H, CO, H_2, OH, NO, SO_2, Air, N_2, O_2.

Governing Equation for Unburned Zone (https://www.gtisoft.com):

$$\frac{d(m_{ub}e_{ub})}{dt} = -p\frac{dV_{ub}}{dt} - Q_{ub} + \left(\frac{dm_f}{dt}h_f + \frac{dm_a}{dt}h_a\right) + \frac{dm_{fi}}{dt}h_{fi} \tag{2.1}$$

where,
m_{ub} = Mass of the unburned zone, v_{ub} = Volume of zone
m_f = Mass of fuel, Q_{ub} = Heat transfer rate in unburned zone
m_{fi} = Mass of injected fuel, h_a = Enthalpy of air mass
m_a = Mass of air, h_f = Enthalpy of fuel mass
e_{ub} = Unburned zone energy, h_{fi} = Enthalpy of injected fuel mass
m_a = Mass of air, h_f = Enthalpy of fuel mass
e_{ub} = Unburned zone energy, h_{fi} = Enthalpy of injected fuel mass
p = Cylinder Pressure
ub denotes the unburned zone.

Governing Equation for Burned Zone (https://www.gtisoft.com):

$$\frac{d(m_be_b)}{dt} = -p\frac{dV_b}{dt} - Q_b + \left(\frac{dm_f}{dt}h_f + \frac{dm_a}{dt}h_a\right) \tag{2.2}$$

where b denotes the burned zone, and remaining symbols are similar to that of unburned zone.

Multi-zone models give results closer to reality since it considers the energy and mass balance between the two zones. However for modeling, some additional parameters are required as shown in Table 2.2.

2.3.3 Heat Transfer Models

There are various heat transfer models used for 1-D modelling. In GT Power, WoschniGT model is used for calculating the heat transfer coefficients if measured swirl data is not available. This model uses following equation for calculating the heat transfer coefficient (Heywood 1988).

$$h_c = \frac{3.01426 p^{0.8} w^{0.8}}{D^{0.2} T^{0.50}} \tag{2.3}$$

Table 2.2 Required input parameters for cylinder modeling

Parameter	Description
Fluid initial state	Initial condition of the cylinder
Wall temperature	Initial temperature of cylinder before starting of combustion
Heat transfer model	There are some models, which are used to calculate the heat transfer coefficients such as WoschniGT, WoschniClassic, WoschniSwirl, WoschniHuber and Hohenberg. These models use different coefficients to calculate heat transfer in the cylinder
Flow object	Comprehensive data of piston geometry is used for calculating the inside flow behavior
Combustion object	Object which gives fuel burn rate profile as input
Head initial temperature	Initial temperature of head mass, which are in contact with the combustion gases
Piston initial temperature	Initial temperature of entire piston including piston rings
Cylinder initial temperature	Initial temperature of the cylinder liner
Inlet valve initial temperature	Initial temperature of an inlet valve including associated valve guides
Exhaust valve initial temperature	Initial temperature of an exhaust valve including associated valve guides
Cylinder coolant temperature	Temperature of the coolant, which flows on the back-side of the cylinder walls
Head oil temperature	Temperature of the lubricating oil, which flows over the head surface
Head oil heat transfer coefficient	Heat transfer coefficient of the oil, which flows over the head surface

The WoschniClassic model calculates the heat transfer coefficient without considering the effect of swirl and uses the following equation for calculating the heat transfer coefficient (Heywood 1988).

$$h_c = \frac{3.26 p^{0.8} w^{0.8}}{D^{0.2} T^{0.53}} \tag{2.4}$$

where,
h_c = Convective heat transfer coefficient (WK/m^2)
D = Cylinder bore (m)
p = Cylinder pressure (kPa)
T = Cylinder temperature (K)
W = Average cylinder gas velocity (m/s)

WoschniSwirl and WoschniHuber model uses the same equation as used by WoschniClassic model, but these models utilize swirl number from the center region.

2.3.4 Engine Crank-Train

Crank-train translates the reciprocating motion of the pistons into the rotary motion. This is comprised of three parts namely connecting rod, crankshaft and flywheel. Connecting rod is modeled as a simple beam, which connects the piston and the crankshaft via rotating bearing. Crankshaft drives the cooling system and valve train of the system.

It is a most stressed component of the system as it is subjected to the high tensile, bending and compressive stresses. Flywheel performs multiple functions in the engine. It adds additional inertia on the crankshaft to minimizes the cyclic variations produced by the reciprocating motion of the piston. Some additional parameters have to be defined for modelling the crank-train (Table 2.3).

2.3.5 Valves

Accuracy in valve modelling is very important because it affects the volumetric efficiency, engine noise, mechanical friction and pumping loss. Valve controls the inlet and outlet movements of charge and exhaust gases in the cylinders concerning different piston positions. Valves are located in the cylinder head on all the engines. The most popular shape of poppet-valve for automobile application is a small cup at one end of the stem. A valve stem is placed in a circular passage in the cylinder head. Valve disc head basically opens and closes the ported passage during the in and out movement of the stem. However, some additional parameters have to be defined for modelling the valvestrain as shown in Table 2.4.

2.3.6 *Orifice Connection*

Orifice connections is used to measure the flow rate of fuel or exhaust gas, which mainly work on the differential pressure measurement principle. This connection is used at the location, where flow-rate measurements are required. The orifice connection offers the following advantages.

- It measures a wide range of flow rates in a pipe.
- Most suitable for measuring the fuel and exhaust flow rates.
- Offers very small amount of pressure drops across the sides of orifice plates.

For modeling, some additional parameters are required as given in Table 2.5.

2.4 Model Demonstration

This section describes the simple model preparation using commercialized 1-D software GT-Power. GT-SUITE have a comprehensive set of automotive components in their libraries, which are used to simulate the physics of fluid flow, thermal,

Table 2.3 Required input for crank-train modelling

Parameter	Description
Engine type	2-stroke; 4-stroke
Speed or load specifications	It depends on the study objective of the model. Either it is for different speeds or percentage of total load
Start of cycle (CA at IVC)	It is a value after the closing of the inlet valve and before the start of combustion
Cylinder geometry	It is a detailed geometry of the cylinder such as bore, stroke and compression ratio
Firing order	This value is necessary during the modelling of multi-cylinder engine
Cylinder number	It shows the sequence of cylinder firing
Firing intervals	It is an angle of the firing relative to the preceding cylinder
Geometry of connecting rod	All dimensions are required such as big end bore, main rod length and connecting rod length

Table 2.4 Required inputs for valves

Parameter	Description
Cam timing angle	Angle between the cam timing anchor reference and cam timing lift array
Valve lift	Distance through which valve is opened maximum from its seated position
Valve lash	Clearance between valve and camshaft

Table 2.5 Modelling of orifice connections

Parameter	Description
Hole diameter	Diameter of the orifice
Geometric area	Total area of the orifice
Forward discharge coefficient	Discharge coefficient of the orifice in the forward direction
Reverse discharge coefficient	Discharge coefficient of the orifice in the reverse direction

mechanical, electrical, magnetic properties of materials and controls (https://www.gtisoft.com/). These libraries are used to build accurate models of entire vehicle, engine, driveline, transmission, general powertrain, mechanical systems, hydraulics, lubrication, friction, thermal management, cooling, chemistry, after treatment and much more (https://www.gtisoft.com/). GT-SUITE provides 1-D modeling solutions for real-time, HiL/SiL, and control system simulations. Also, a broad array of built-in advanced features such as design of experiments (DoE), optimization. In addition, distributed and parallel processing enhance user productivity and effectiveness. The software is designed around a series of icons and connectors that define each engine components and a logical interface for their use (Kmec et al. 2009). There are two main operating domains of this software called GT-ISE and GT-POST. GT-ISE provides an environment, where various components are taken out in project map to make the model, simulations setting are declared, simulations are launched in single or batch mode. 1-D model is then prepared using the following steps where dummy values are selected to present the demonstration model. Typical view of the model is shown in Fig. 2.4.

Step 1: Inlet end environment is selected from the template library and different boundary conditions such as pressure, temperature, humidity are defined in the inputs.

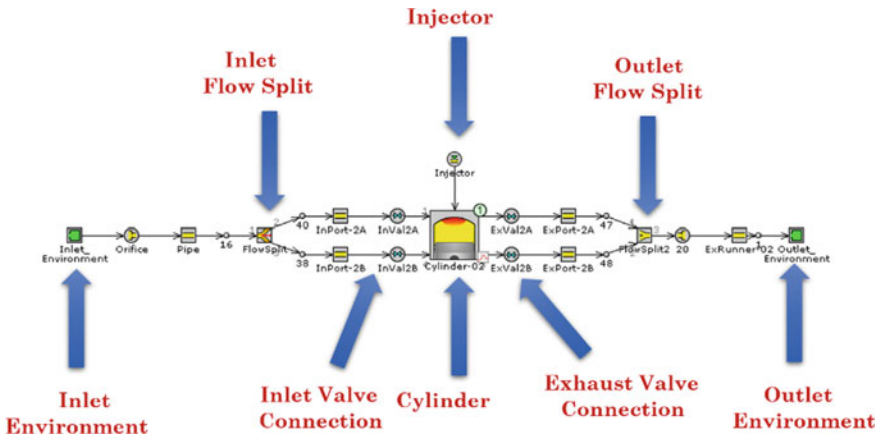

Fig. 2.4 Typical map view of the 1-D model of a single cylinder engine

Step 2: Pipe round object is selected to define a pipe connections, which are generally used in the air intake. Cross-section area is given as input.
Step 3: Bend pipe round is selected to define a bend pipe connections, where bend angle is given as input.
Step 4: Orifice is selected from the library to calculate the mass flow rate between the adjacent flow volumes, where orifice diameter and discharge coefficients are given as inputs.
Step 5: Cylinder is selected from the library to specify the attributes of the engine cylinder. Required inputs are given as mentioned in Table 2.2.
Step 6: Valve cam connections are selected to define characteristics of a cam-driven valve where essential inputs such as geometry, lift profile, and flow characteristics are defined.
Step 7: Engine crank-train is selected from the library to model the kinematics and rigid dynamics of a common reciprocating IC engine crank-train. Required inputs are given as mentioned in Table 2.3.
Step 8: Injector is selected to define the required parameters such as injection of a periodic mass flow rate or pressure profile of fuel.

Da Silva Trindade and dos Santos prepared 1-D model using GT-Power to validate the simulation results. Figure 2.5 (da Silva Trindade and dos Santos 2018) shows the in-cylinder pressure variations w.r.t. crank angle degree (CAD) position of an engine fuelled with BU40 (60% gasoline and 40% butanol on volume basis) and gasoline. Good correlation between experimental and computational results was reported (8% deviation between experimental and simulation results). The maximum value of

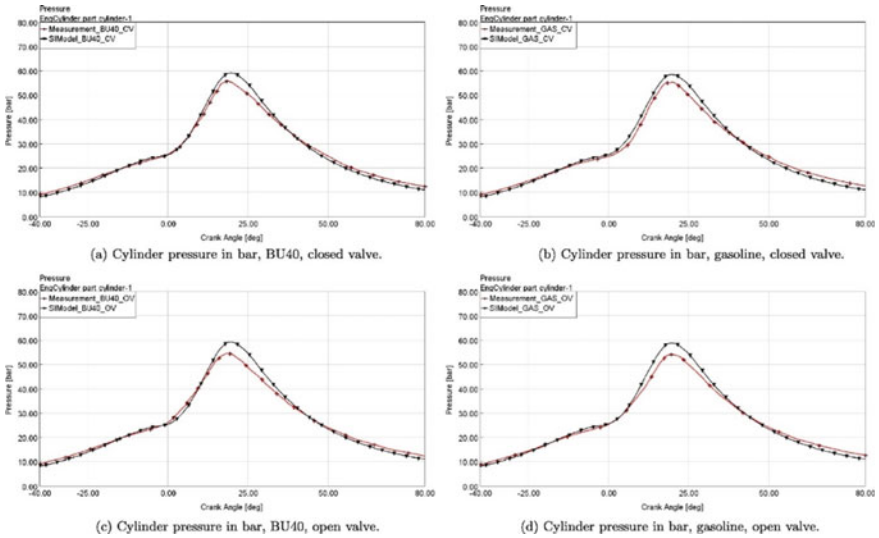

Fig. 2.5 In-cylinder pressure versus CAD for BU40 and gasoline (da Silva Trindade and dos Santos 2018) (experimental results: red lines and computational results: black lines)

experimental results was slightly lower than simulation results because of pressure losses in the real engine.

Several other researchers performed comparative investigations of alternate fuels vis-à-vis baseline petroleum based fuels to investigate the effects on engine performance parameters. Table 2.6 shows the modelling results for performance and emissions of the engines fuelled with different alternative fuels. Preliminary results of modelling can be validated using experimental results and after the validation of model, more extensive investigations can be done using modelling and simulation tools, making the development process quicker and cheaper.

2.5 Conclusions

Modelling techniques help extensively in feasibility studies and preliminary investigations of new fuels in IC engines and these studies can be done without extensive engine experiments. This chapter presents a review of the requirements IC engine modelling. Suitability of methanol in CI engines is also discussed in this chapter briefly. Two main tools namely 1-D modelling and 3-D modelling are touched upon. 1-D modelling shows the effects of possible alternate fuels on engine performance and emissions however, 3-D modelling provides a platform for exploring the effect of alternate fuels on specific engine components. Using 3-D modelling, different components of the engine such as injector, cylinder head, etc. can be optimally designed to improve the engine performance and lower emissions. Finally, modelling in engine research can reduce the efforts required for adaptation of alternate fuels. These techniques help in preliminary investigations of performance and emissions studies of alternative fuels and play an important role in feasibility studies for new technology adaption.

Table 2.6 Typical results of 1-D simulation studies

Team	Aim	Procedure followed for modelling	Results
Chougule et al. (2013)	Determine the potential of dual fuel (CNG and Diesel) to improve the engine fuel economy	**Step 1**: Experiments were performed using diesel in a 4-cylinder, 2500 cc engine	Deviations between the experimental and simulation results were less than 10% and 5% for torque and BSFC respectively
		Step 2: Engine model was prepared using GT-Power	

(continued)

Table 2.6 (continued)

Team	Aim	Procedure followed for modelling	Results
		Step 3: Validation of simulation results using experimental results	
		Step 4: CNG was injected along with diesel in the validated engine model	BSFC increased by 13 and 9 for 50 and 70% load respectively using CNG as fuel
		Step 5: Results of engine performance were discussed	Fuel economy improved by 10% in a dual fuel engine, where diesel was injected as a pilot
Mtui (2013)	Determine the performance of dual fuel (Natural Gas/diesel) using 1-D/3-D simulations	**Step 1**: 1-D model of 18-cylinder engine was prepared using GT-Power	Natural gas can be used as a fuel for replacement of up to 60% baseline fuel
		Step 2: Prepared model was coupled with 3-D based KIVA software to provide accurate boundary conditions to the intake and exhaust valves during transients	Beyond 40% diesel replacement, engine power output decreased
Jadhav et al. (2017)	Determine the engine performance of dual fuel (Diesel-CNG) using GT Power	**Step 1**: Experiments on diesel fuel using 4-cylinder, 3000 cc engine	**Performance**: BSFC, and volumetric efficiency decreased by 8% and 5% respectively for dual fuel model compared to baseline fuel model **Emissions**: CO and HC emissions increased for dual fuel model, whereas PM emissions increased compared to baseline fuel model
		Step 2: Baseline 1-D model was prepared	
		Step 3: Simulation results were validated with the experimental results	
		Step 4: CNG was injected along with diesel in a validated baseline model (Port Injection)	

(continued)

Table 2.6 (continued)

Team	Aim	Procedure followed for modelling	Results
Soid et al. (2015)	Determine the performance of methane-fuelled engine	**Step 1**: Experiments on 4-stroke, single cylinder, 100 cc SI engine **Step 2**: Baseline 1-D model was prepared using the engine data **Step 3**: Simulation results were validated using calibration methods **Step 4:** Methane was injected in a validated baseline model using port fuel injection method	Engine torque, BMEP, brake power, and peak cylinder pressure decreased for methane-fuelled model compared to gasoline-fuelled model Optimization was done using different inlet valve openings and outlet valve openings They retarded exhaust valve timing by 10° and found comparable results to gasoline-fuelled model

References

Statistics by International Energy Agency. https://www.iea.org/weo2018/

Knothe G (2010) Biodiesel and renewable diesel: a comparison. Prog Energy Combust Sci 36(3):364–373. https://doi.org/10.1016/j.pecs.2009.11.004

Web Source: https://www.e-education.psu.edu/egee439/node/684

Agarwal AK (1998) Vegetable oils versus diesel fuel: development and use of biodiesel in a compression ignition engine. Tide 8(3):191–204

Agarwal AK, Das LM (2001) Biodiesel development and characterization for use as a fuel in compression ignition engines. J Eng Gas Turbines Power 123(2):440–447. https://doi.org/10.1115/1.1364522

Urja A (2013) Ministry of New and Renewable Energy, Government of India, New Delhi, vol 7(1)

GT Power Software. https://www.gtisoft.com/gt-suite-applications/propulsion-systems/gt-power-engine-simulation-software/

Converge Software. https://convergecfd.com/

KIVA Software. https://en.wikipedia.org/wiki/KIVA_(software)

SI Engine. https://www.mechanicalbooster.com/2017/10/spark-ignition-engine.html

CI Engine. https://www.howacarworks.com/basics/how-a-diesel-engine-works

Hariram V, Bharathwaaj R (2016) Application of zero-dimensional thermodynamic model for predicting combustion parameters of CI engine fuelled with biodiesel-diesel blends. Alexandria Eng J 55(4):3345–3354. https://doi.org/10.1016/j.aej.2016.08.021

Payri F, Olmeda P, Martín J, García A (2011) A complete 0D thermodynamic predictive model for direct injection diesel engines. Appl Energy 88(12):4632–4641. https://doi.org/10.1016/j.apenergy.2011.06.005

Neshat E, Honnery D, Saray RK (2017) Multi-zone model for diesel engine simulation based on chemical kinetics mechanism. Appl Therm Eng 121:351–360. https://doi.org/10.1016/j.applthermaleng.2017.04.090

Engine Performance Manual. https://www.gtisoft.com
Heywood JB (1988) Internal combustion engine fundamentals
Gamma Technologies. The standard in multi-physics system. https://www.gtisoft.com/
Kmec JF, Kassebaum DA, Noerenberg RL (2009) First-time experience with engine simulation software in an internal combustion engines course. College of Technology, Purdue University, West Lafayette, IN, 47907
da Silva Trindade WR, dos Santos RG (2018) 1D modeling of SI engine using n-butanol as fuel: adjust of fuel properties and comparison between measurements and simulation. Energy Convers Manag 157:224–238. https://doi.org/10.1016/j.enconman.2017.12.003
Chougule VP, Vora KC, Suryavanshi Y (2013) Design and Simulation of 2.5 L Dual Fuel (Diesel-CNG) Engine for Performance Parameters (No. 2013-01-2885). SAE Technical Paper. https://doi.org/10.4271/2013-01-2885
Mtui PL (2013) Performance and emissions modeling of natural gas dual fuelling of large diesel engines. Int J Sci Technol Res 2(11):317–323
Jadhav AA, Hulwan DB (2017) Simulation of dual fuel (Diesel-CNG) engine of off road vehicle. Simulation 1(3)
Soid S, Amir S, Ismail M, Hamid M, Amzari M, Said M (2015). Simulation studies on the performance of small engine fuelled by methane and the effect of various valve timings. Indian J Sci Technol 8. https://doi.org/10.17485/ijst/2015/v8i30/87250

Chapter 3
Simulation and Optical Diagnostics for Internal Combustion Engines

Current Status and Way Forward

Koji Yasutomi, Tsukasa Hori and Jiro Senda

Abstract Enhancing the predictability of diesel spray numerical simulation, a droplet breakup model has been developed and optimized under non-evaporative diesel spray with a large-eddy simulation. In the spray simulation community, the model called Kelvin–Helmholtz and Rayleigh–Taylor model has been widely used even nowadays, both of which are modeled for high Weber number conditions. While upstream region of spray considers as high Weber number thanks to high injection pressure, downstream of the spray represents by low Weber number region. In this study, a hybrid breakup model which combines the Kelvin–Helmholtz and modified Taylor analogy breakup has been proposed. The Kelvin–Helmholtz and modified Taylor analogy breakup models are used to the primary and secondary breakup models, respectively. For validating the breakup model, one of the unique optical diagnostics techniques has been introduced to capture both macroscopic and microscopic spray characteristics at the same time. The system called super high spatial resolution photography lens is able to capture sufficient area of the spray with having a 5 μm spatial resolution. Spray simulations under non-evaporative condition were performed to validate the Kelvin–Helmholtz–modified Taylor analogy breakup model. It is found that the simulation results of Kelvin–Helmholtz–Modified Taylor analogy breakup are in good agreement with experimental measurements of droplet distribution under non-evaporative spray.

K. Yasutomi (✉)
Hino Motors Ltd., 3-1-1 Hino-dai, Hino-shi, Tokyo, Japan
e-mail: ko.yasutomi@hino.co.jp

T. Hori
Osaka University, 1-1 Yamadaoka, Suita, Osaka, Japan

J. Senda
Doshisha University, 1-3 Tatara Miyakodani, Kyotanab-shi, Kyoto, Japan

A. P. Singh et al. (eds.), *Simulations and Optical Diagnostics for Internal Combustion Engines*, Energy, Environment, and Sustainability,
https://doi.org/10.1007/978-981-15-0335-1_3

3.1 Introduction

Development of internal combustion engines (ICE) is strongly progressed by optical observations of in-cylinder spray and combustion. Especially, the advancement of the illumination source has been contributed to measure spray and combustion dynamics as in situ; it is non-contact, non-destructive, and not affected the observation field. Since physics in ICE is a quite short period, high time resolution measurement technique is also necessary to capture time-development of spray and combustion characteristics. However, to obtain enough time resolution limits spatial resolution to capture entire spray fields. Depending on the observation target, it is necessary to choose the proper photographic technique and setting.

A result of an experiment is utilized to develop a predictable model and for the validation of numerical simulation (computational fluid dynamics: CFD). Until recently CFD is highly limited by computational resource, most of all CFD has been used Reynolds averaged Navier–Stokes (RANS) simulation. The result of RANS simulation considers as ensemble average, it is crucial for engine design in automotive manufactures, but lack of instant information is a challenge to understand physics and develop future high-efficiency engines. Thanks to the development of computer performance, large eddy simulation (LES) has been utilized for ICE simulation. Depending on computer resources, cycle simulation also can be done by LES (Pasunurthi et al. 2017; Masouleh et al. 2018; Goryntsev et al. 2009; Granet et al. 2012; Enaux et al. 2011). Coupling with the machine learning technique, it extracts the important design factor for improving engine performance (Kodavasal et al. 2018; Di Mauro et al. 2019).

In this chapter, one of the unique optical diagnostics has been introduced to obtain characteristics of the fundamental diesel spray (Marubayashi et al. 2011). As mentioned in earlier, there is a trade-off relation between capturing macroscopic (e.g., spray penetration and spray angle) and microscopic (e.g., droplet diameter and distribution) characteristics of the diesel spray at the same time. With using a unique lens system and large-film, it is able to measure both features. LES simulation also performs to simulate non-evaporative spray. Each technique and simulation is mentioned briefly, and please note that it does not represent all-optical diagnostics technique and numerical simulation. Following is mainly extracted briefly from reference paper and journal (Kitaguchi et al. 2012, 2014; Fujii et al. 2015).

3.2 Optical Diagnostics of Super High Spatial Resolution Photography (Kamata et al. 2008)

General optical measurement techniques are challenged to have both macroscopic and microscopic characteristics. To make it an open possibility to over-come this problem, one of the unique optical diagnostics techniques called super high spatial resolution photography (SHSRP) is introduced to the diesel spray. Detail lens system

with SHSRP and a thinner depth of field can be found in Kitaguchi et al. (2014) and Kamata et al. (2008). Since the length of the lens system has achieved to design only 204 mm, it can minimize the total experimental setups with maintaining a 5 μm spatial resolution, 400 mm working distance, 2.7–5.0 magnification range, and 100 μm depth of fields.

The optical setup for the spray injection experiments also founds in Kitaguchi et al. (2014) and Kamata et al. (2008). Unlike to use the high-speed camera as a measuring device, the image is taken on a large-sized film (Kodak: TMAX100), 254 mm (10 in.) in height and 202 mm (8 in.) in width, with resolution ranging from 63 to 200 line/mm.

3.2.1 *Image Analysis Technique (Marubayashi et al. 2011; Kamata et al. 2008)*

As post-processing for evaluating the droplet in this optical system, following evaluation are performed: (1) droplet position, (2) circle-equivalent diameter, (3) relative dispersion, and (4) average intensity gradient (ADG) of the periphery of droplet images. Applying (2) to (4) evaluations to each droplet, blurred droplet images and background noise are eliminated from the results of the measurement. Circle equivalent diameter is calculated as:

$$D = \sqrt{\frac{4A}{\pi}}, \tag{3.1}$$

where A is the area of droplet image. Relative dispersion of L/L_O is used isoperimetric inequality $s^2/A \geq 4\pi$:

$$\frac{L}{L_O} = \frac{S^2/A}{4\pi}, \tag{3.2}$$

here S is perimeter, L is degree of dispersion, L_O is degree of dispersion circularity. Since droplet images are an elongated shape with increasing L/L_O, droplet images are eliminated from observation target considered as droplet overlapping or background noise when the $L/L_O \geq 1.2$.

In this technique, spray images are scanned into the computer by film scanner (EPSON: GT-X970). Image resolution while scanning is set 0.98 μm/pixel to resolve 5 μm droplet diameter. For minimizing the background noise, averaged intensity gradient (ADG) is used to eliminate the blur droplet. Because the depth of fields in this system is 100 μm, image processing field was defined ±50 μm from the focus position of this lens system.

Image samples of SHSRP and droplet distribution after the image analysis are displayed in Fig. 3.1. Macroscopic spray information is represented in Fig. 3.1a and enlarged spray microscopic information is in Fig. 3.1c. Figure 3.1b and d are

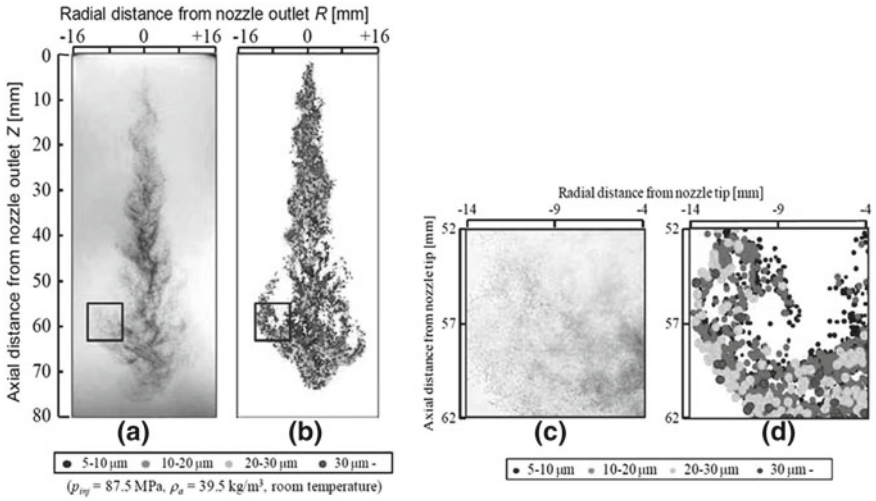

Fig. 3.1 Image samples of SHSRP and droplet distribution after the image analysis: **a** Row image and **b** After the image processing for macroscopic spray and **c** Row image and **d** After the image processing for macroscopic spray surrounded by black lines in (**a**) and (**c**). Kitaguchi et al. (2014)

corresponding with after the image processing against Fig. 3.1a and c, respectively. As mentioned in earlier, both macroscopic and microscopic characteristics of diesel spray at the same time can capture by this technique. Thanks to this optical diagnostic technique, the relation between large vortex structure and droplet distribution are clearly represented in this image. While relatively big droplets are distributed in the periphery of the vortex structure, small droplet follows the vortex flow, because of smaller Stokes number. The SHSRP results were used for validating the spray break-up model by comparing droplet size distribution and entire spray distribution.

3.3 Simulation Setups

Large-eddy simulation (LES) is introduced into the KIVA code to produce KIVA-LES (Sone et al. 2000a, b, 2001), spray simulation had done in this code. While similar simulation can be done by various commercial simulation code such as ANSYS Fluent, AVL Fire, Convergent science Converge, Riccardo Vectis and Siemens Star-CCM, etc., one of the advantages using KIVA is derived from open-source code. Recently OpenFOAM is also a useful code to simulate spray and combustion simulation as referenced in Hanasaki et al. (2015) and Nguyen et al. (2014).

Detail governing equation for KIVA-LES is described in Fujii et al. (2015) and Sone et al. (2000b).

3.3.1 Breakup Model

The purpose of this chapter is summarized as spray characteristics comparison using breakup models including the KH–RT (Beale and Reitz 1999) and the KH–MTAB (Kitaguchi et al. 2012, 2014; Fujii et al. 2015) hybrid model. A fuel injection events are strongly dominated by distributions of Weber number which is high in nozzle exit whereas relatively low as leaving from the nozzle exit. It is a reasonable to use a hybrid model of KH model developed based on high Weber number region and MTAB model designed based on low Weber number region. Breakup model equations are summarized in Fujii et al. (2015).

Both KH-RT and KH-MTAB models are a hybrid model of KH and RT model, and KH and MTAB model, respectively, it requires a hybrid scheme to switch the primary breakup model to secondary breakup model. In the KH-RT model, the KH model simulates the primary breakup below the breakup length and the RT model represents the secondary breakup beyond the breakup length. Breakup length is defined by Levich theory (1963),

$$L_b = C_l d_0 \sqrt{\frac{C_l}{\rho_a}}, \tag{3.3}$$

where d_0 and C_1 are the nozzle diameter and the experimental constant, respectively. The value of C_1 is given by 10 in this chapter (Hori et al. 2007). The threshold of the breakup is found near Weber number $We = 450$; therefore, in the KH–MTAB model, KH model is used for primary breakup at $We > 450$ and the MTAB model for secondary breakup at $We \leq 450$. Because of the result of optimization, there is no physical mean that We is 450. The Weber number is given by

$$We = \frac{\rho_d U_r^2 d_p}{\sigma}, \tag{3.4}$$

where ρ_d is the droplet density, U_r is relative velocity between the gas and the liquid, and d_p is the droplet diameter.

3.3.2 Computational Scheme and Condition

A blob model was applied to fuel injection so that the diameter of the injected fuel droplet is equivalent to the nozzle diameter. The effects of the collision and coalescence of droplets in the spray were not considered. The momentum exchange between the gas phase and the droplets was considered using a source term in the momentum equation. To calculate the drag coefficient, $C_{D,\ sphere}$ was assumed as a rigid sphere of a droplet

Table 3.1 Numerical setups

Ambient gas	Ideal gas
Convective terms in the momentum equation Space derivatives	Central difference
Convective terms in the momentum equation Time derivatives	Forth-order Runge-Kutta
Other space derivatives of the convective term	QSOU
Other time derivatives of the convective term	Euler's forward
Computational domain	30 mm diameter × 100 mm height
Computational grid resolutions	60 × 60 × 200
Total number of cells	720,000
Wall boundary conditions	Non-slip wall

$$C_{D,\ sphere} = \begin{cases} \frac{24}{Re_l}\left(1 + (1/6)Re_l^{2/3}\right), & Re_l < 1000 \\ 0.424, & Re_l \geq 1000 \end{cases} \tag{3.5}$$

Since KH-MTAB model was used the TAB based model as secondary break up, distortion of the droplet also needed to take into account. Therefore, Liu et al.' (1993) equation employed for KH-MTAB model

$$C_D = C_{D,sphere}(1 + 2.632y), \tag{3.6}$$

where y is the length of deformation of the droplet computed from the TAB model. Numerical setups were summarized in Table 3.1.

3.3.3 Computational and Experimental Conditions

Computational and experimental conditions in a non-evaporative spray field were executed under main and pilot sprays. The injection duration of the main and pilot sprays were 1.30 and 0.45 ms, respectively. With changing the injection duration, fuel amount was 12.0 and 3.72 mg for main and pilot sprays, respectively. single hole 0.20 mm diameter of the diesel injector was employed and the n-C13H28 with 77 MPa injection pressure was injected. Fuel temperature was kept 300 K. For the purpose of observing the effect of ambient density under the non-evaporative spray, ambient gas was used CO_2. Ambient pressure was changed from 1.8 to 2.7 MPa, it is corresponding with 35.5 to 55.7 kg/m^3 under 300 K ambient gas temperature.

3.4 Results and Discussion

Effectiveness of spray breakup model was validated for macroscopic spray characteristics (e.g., Spray penetration) as well as droplet size and distribution from SHSRP.

One of the distinct differences between KH-MTAB and KH-RT models could be found from the particle-size distribution frequency (PDF) of droplet diameters against the entire spray range during injection (0.65 ms) and the end of injection as shown in Fig. 3.2. Both data were taken with an ambient density of 48.4 kg/m^3 under main spray conditions. The concentration of small droplets tends to decrease in KH–RT and KH–MTAB with developing the spray. As a low Weber number region in the spray increases with time, there is observed that the decreasing of the frequency of small droplets. In addition, the result using KH-RT model is difficult to reproduce a spray structure as shown in Fig. 3.1, because most droplets break up to a very small diameter.

In diesel spray, Weber number is high in the region near the nozzle as opposed to the downstream of the spray, resulting in a high number of small-diameter particles. On the other hand, the PDF distribution of the droplet de-rived from KH-MTAB model is evenly distributed, the droplet spatial distribution in the diesel spray represents the spray structure more accurately.

Verifying the effect of breakup model more detail, SHSRP image taken at $t/t_{inj} = 7.0$ (normalized time by injection duration) was used due to this photographic technique is challenging to apply high number density region such as during injection.

The results of LES and the experimentally obtained droplet spatial distribution using SHSRP under the pilot spray condition at $t/t_{inj} = 7.0$ are shown in Fig. 3.3. Distribution images are plotted from the center of gravity of droplets, which are divided into four classes: 7.8–10, 10–20, 20–30 mm, and more than 30 mm. This classification of particle size was also used in the LES.

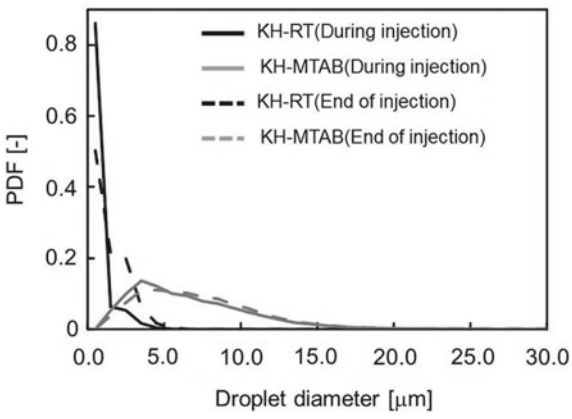

Fig. 3.2 PDF distribution of droplet diameter in the spray during injection and the end of injection. Kitaguchi et al. (2014)

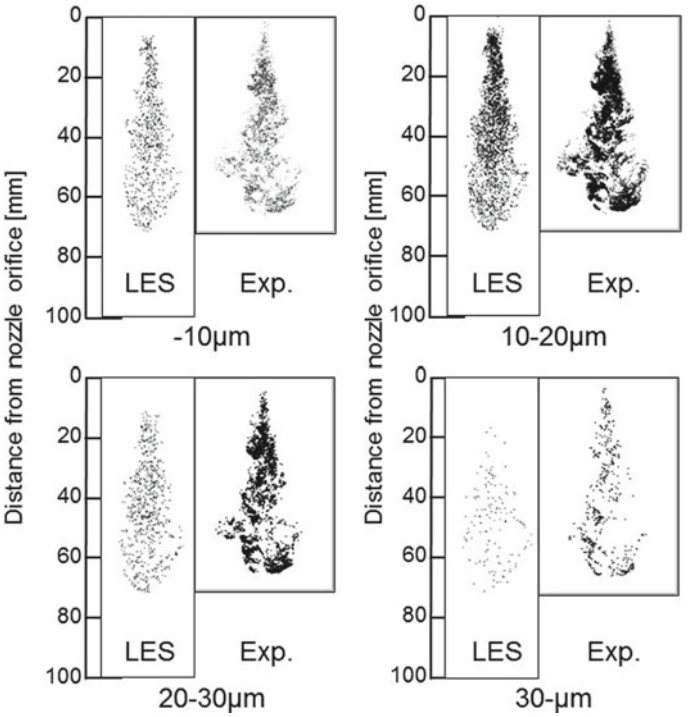

Fig. 3.3 Spray images organized by droplet range from LES and SHSRP

In the LES and experimental results, the small droplets are distributed over the entire region, whereas there is a high proportion of droplets with diameters of >30 μm at the spray tip because large droplet with high momentum is difficult to follow the ambient gas through the central axis of the spray and to stay near the spray tip. For supporting these findings, Stokes number was introduced to each droplet sizes.

The Stokes number is defined by the following equation

$$\mathrm{S}_t = \frac{\tau_A}{\tau_F}, \tag{3.7}$$

where τ_A is the response time for the flow field and τ_F is the characteristic turbulence time

$$\tau_A = \frac{\rho_p d_p^2}{18\mu}, \tag{3.8}$$

$$\tau_F = \frac{\delta(x)}{U(x)}, \tag{3.9}$$

where ρ_p is the droplet density, d_p is the droplet diameter, and μ is the coefficient of viscosity of the gas ambient. $\delta(x)$ is defined as the average of the spread of the spray in the radial direction and $U(x)$ is defined as the average relative velocity at t/t_{inj}= 7.0. There has not conducted particle image velocimetry (PIV) type measurement in this setups before, velocity information for experimental data are also employed from simulation results. In this result, there is a strong correlation between droplet diameter of >30 μm and St ≥ 1. While droplet smaller than 30 μm are evenly distributed in the spray, there is strongly suggested that St ≥ 1 droplets are present in the periphery of the spray and vortex structure.

3.5 Conclusion

In this chapter, the unique optical technique called super high spatial resolution photography (SHSRP) was introduced to capture both macro and microscopic spray characteristics at the same time. Under diesel engine conditions, obtaining macroscopic spray characteristics during the injection periods are challengeable in especially high number density region, but applying this technique revealed that large droplets were distributed periphery of the large vortex structure and the tip of the spray. Coupling with the Stokes number analysis, such droplet represents more than 30 μm droplets.

For improving the numerical simulation accuracy, KIVA based large-eddy simulation was also conducted to optimize the spray break up model by comparing experimental results from SHSRP. In diesel sprays, the region near the nozzle orifice is considered as higher Weber number, middle and downstream of the spray consists of lower Weber number as exchanging the momentum with ambient gas.

In this study, the breakup model call KH-MTAB hybrid model was employed instead of the famous KH-RT breakup model. While both KH and RT breakup models are designed from high Weber number phenomenon, applying MTAB model as for secondary breakup instead of RT model consider as more representing a real-world spray physics. This hybrid model was applied into the non-evaporative spray and compared to KH-RT model under wide-range of ambient density.

Using KH-MTAB model, droplet distribution in the diesel spray is able to reproduce experimental results more accurately, which large droplet more existing tip of the spray and periphery of the large vortex structure.

For developing a numerical engine spray and combustion model, it is always important to have reliable experimental results obtained by proper optical diagnostics and validated by numerical simulation.

Acknowledgements This work was supported by Grants-in-Aid for Scientific Research (B) (17360102). In addition, part of this work was supported by "Academic frontier promotion work" through an academic research promotion grant to private universities by the Ministry of Education, Culture, Sports, Science and Technology to support "Next-generation zero-emission energy-conversion system" (S0901038: 2009–2013).

References

Beale JC, Reitz RD (1999) Modeling spray atomization with the Kelvin-Helmholtz/Rayleigh-Taylor hybrid model. Atomizat Sprays 9(6):623–650

Di Mauro A, Chen H, Sick V (2019) Neural network prediction of cycle-to-cycle power variability in a spark-ignited internal combustion engine. Proc Combust Inst 37(4):4937–4944

Enaux B, Granet V, Vermorel O, Lacour C, Pera C, Angelberger C, Poinsot T (2011) LES study of cycle-to-cycle variations in a spark ignition engine. Proc Combust Inst 33(2):3115–3122

Fujii Tatsunori, Kitaguchi Koji, Hatori Soichi, Hori Tsukasa, Senda Jiro (2015) Development of breakup model for large eddy simulation of diesel spray. J Energy Power Eng 7(12):2312–2320

Goryntsev D, Sadiki A, Klein M, Janicka J (2009) Large eddy simulation based analysis of the effects of cycle-to-cycle variations on air-fuel mixing in realistic DISI IC-engines. In: Proceedings of the combustion institute, vol 32 II, no 2, pp 2759–2766

Granet V, Vermorel O, Lacour C, Enaux B, Dugué V, Poinsot T (2012) Large-Eddy Simulation and experimental study of cycle-to-cycle variations of stable and unstable operating points in a spark ignition engine. Combust Flame 159(4):1562–1575

Hanasaki M, Komae J, Hori T, Matsumura E, Senda J (2015) Large Eddy Simulation of diesel spray using OpenFOAM. Trans Soc Autom Eng Japan 47(2):20155110

Hori T, Kuge T, Senda J, Fujimoto H (2007) Large Eddy simulation of diesel spray combustion with Eddy-dissipation model and CIP method by use of KIVALES. SAE Technical Paper 2007-01-0247

Kamata S, Katsuta K, Hori T, Senda J, Fujimoto H (2008) Visualization of diesel spray by using direct photography with high spatial resolution. Atomiza J ILASS-Japan 17(58):23–30

Kitaguchi K, Hatori S, Hori T, Senda J (2012) Optimization of breakup model using les of diesel spray. Atomizat Sprays 22(1):57–77

Kitaguchi K, Fujii T, Hatori S, Hori T, Senda J (2014) Effect of breakup model on large-eddy simulation of diesel spray evolution under high back pressures. Int J Engine Res 15(5):522–538

Kodavasal J, Moiz AA, Ameen M, Som S (2018) Machine learning analysis of factors impacting cycle-to-cycle variation in a gasoline spark-ignited engine. In: Proceedings of the ASME 2017 internal combustion engine division fall technical conference ICEF2017 October 15–18, 2017, Seattle, Washington, USA, 2017, November 2018

Levich VG (1963) Physicochemical hydrodynamics. J Chem Educ 40(10):A827

Liu AB, Mather D, Reitz RD (1993) Modeling the effects of drop drag and breakup on fuel sprays. SAE Technical Paper, 930072

Marubayashi N, Yano T, Hori T, Senda J, Fujimoto H (2011) The time sequence measurement of diesel spray by using of super high resolution photography. Atomizat J ILASS-Japan 20(70):106–113

Masouleh MG, Keskinen K, Kaario O, Kahila H, Karimkashi S, Vuorinen V (2018) Modeling cycle-to-cycle variations in spark ignited combustion engines by scale-resolving simulations for different engine speeds. Appl Energy 250:801–820

Nguyen T, Janas P, Lucchini T, D'Errico G, Kaiser S, Kempf A (2014) LES of flow processes in an SI engine using two approaches: OpenFoam and PsiPhi. SAE Technical Paper 2014-01-1121

Pasunurthi S, Jupudi R, Wijeyakulasuriya S, Gubba SR, Im HG, Jaasim M, Primus R, Klingbeil A, Finney C (2017) Cycle to cycle variation study in a dual fuel operated engine. SAE Technical Paper, 2017-01-0772

Sone K, Patel N, Menon S (2000a) Implementations of large-eddy simulation into KIVA code—part 1: theory and formulation. Atlanta, GA

Sone K, Patel N, Menon S (2000b) Implementations of large-eddy simulation into KIVA code—part 2: practicums on implementation. Atlanta, GA

Sone K, Patel N, Menon S (2001) Large-eddy simulation of fuel-air mixing in an internal combustion engine. In: 39th AIAA Aerospace Sciences Meeting

Chapter 4
Numerical Investigations on Water-Ethanol-Diesel Emulsified Fuel

Rabinder Singh Bharj, Vishal Vasistha, Narinder Singh and Gurkamal Nain Singh

Abstract The depleting oil resources and harmful emissions from fossil fuel have raised keen attention whole world wide. Emulsified fuel technology might prolong availability of earthborn fossil fuel along with the reduction of the pollutants. It may also be seen as a useful technique to meet the latest stringent Bharat Stage VI norms in diesel engine. Emulsification requires mixing fossil fuel with water in the presence of a surfactant. Oxygenated fuels like alcohols may also be blended due to its renewability. Oxides of nitrogen tend to reduce owing to cooling effect of water content in the emulsified fuel. At the same time decrease in the amount of particulate matter in the tail pipe was observed because of reduced molecule size of emulsified fuel. The combustion and exhaust emissions characteristics have been elaborated numerically with the help of simulation software in this chapter. Acceptability of emulsified fuels has also been highlighted for its use in compression ignition engines.

Keywords Emulsification · Simulation · Ethanol

4.1 Introduction

Compression ignition engines have been playing an immense role in the transport and power generation. However the imminent energy crisis in future, increasing costs and harmful emissions associated with mineral diesel have forced researchers to find out and explore the possibility of alternate clean and non-polluting fuels for compression ignition engines (Gilbert and Perl 2008). Several techniques have been followed to get rid of emissions and to impede the depletion of pending hydrocarbons. Commonly considered alternative fuels include alcohol based biofuels and non-conventional fossil fuels derived from different sources. High viscosity and poor atomization of vegetable oils restrict their use in diesel engine. Natural gas, propane and hydrogen reduce emissions to some extent however they are products of fossil

R. S. Bharj (✉) · V. Vasistha · N. Singh · G. N. Singh
Department of Mechanical Engineering, Dr. B. R. Ambedkar, National Institute of Technology, Jalandhar 144011, India
e-mail: bharjrs@nitj.ac.in

A. P. Singh et al. (eds.), *Simulations and Optical Diagnostics for Internal Combustion Engines*, Energy, Environment, and Sustainability,
https://doi.org/10.1007/978-981-15-0335-1_4

fuel. Diesel engines play a supreme role in transportation, agriculture and industry (Dewulf and Van Langenhove 2006). About thirty years ago, the technology of application of emulsion fuels to compression ignition engine has attracted much attention. Emulsified fuel consists of continuous and dispersed phase where water is used as dispersed phase with/without surfactant. To alleviate the drawbacks of emulsified fuel, potential additives have been introduced in them in order to achieve reduction in emissions and improvement in combustion attributes at par with performance (Anton and Vandamme 2010; Becher 1965). However NO_x and PM from diesel engines cause a serious challenge to manufacturers and threat to environment. However, emulsification of diesel fuel is the best method which needs no engine modification. Emulsification is the process of adding water to the fuel in micro or macro scale (Bibette et al. 1999).

On the accounting of the nature of the continuous and dispersed phase, emulsions can be categorized as W/O (water in oil)—Water works as a dispersed phase and the oil behaves as a continuous phase. They can be also called as oil emulsions. Cold cream, butter and, cod liver oil are examples of this type of emulsion. O/W (oil in water)—Oil is considered as a dispersed phase and water is served as a continuous phase. Milk is an appropriate example of O/W emulsion. On the basis of droplets size, emulsions can be classified into two categories: Macro emulsions—generated by a process of shearing and have sizes of $0.1-10$ μm. They have a tendency of settled down with respect to time. They are kinetically stable and look milky and opaque. Micro emulsions—produced spontaneously and have sizes in the range of 10–200 nm. They are isotropic, thermodynamically stable and translucent in appearance (Bibette et al. 1999).

Emulsified fuels have certain advantages and disadvantages in terms of combustion and emission concerns. The addition of water in emulsified fuel lowers the combustion temperature due to its high latent heat of vaporization characteristic but at the same time it promotes the micro explosion of emulsion fuel droplets which in result, improves the fuel atomization. The better atomized fuel can be sprayed uniformly inside the combustion chamber that can improve combustion efficiency by complete combustion of emulsified fuel. The lower combustion temperature stops the formation of NO_x because only at higher temperatures (above 1200 K), Nitrogen is decomposed into atomic nitrogen which is very reactive and forms NO_x by reacting with oxygen of air. Owing to complete combustion of emulsified fuel, there is reduction in soot emissions.

Various numerical computational fluid dynamics (CFD) simulation studies are available on combustion of methane, natural gas, diesel-biodiesel blends, diesel-water mixtures and ethanol-diesel blends (Cook and Law 1978; Heywood 1988). But CFD studies on combustion of water-ethanol-diesel emulsions and comparison with diesel-water and diesel-ethanol blends have not been discussed. Combustion study of alternative fuel directly on internal combustion engine may become severe time consuming, complex and costlier if results are not predicted via simulation and numerical investigation.

Shirneshan and Jamalvand (2016) have compared combustion temperature, CO_2, NO_x, SO_2 and soot emissions in a furnace chamber from combustion of wood,

peat, methane and gasoil using CFD Ansys Fluent software. They reported lower combustion temperature, CO_2, NO_x and soot emissions for biomass fuel (wood and peat) than methane and gasoil but higher SO_2 emissions.

4.2 Mathematical Model

The different fundamental mathematical equations of species, energy, mass, momentum and turbulence have been used to describe the mathematical model. In this study, CFD simulations were executed using a standard k-e viscous turbulent flow model and the eddy dissipation (Shirneshan and Jamalvand 2016; Hussain et al. 2012; Palaniswamy et al. 2016). The heat transfer and radiation effects are neglected for this particular mathematical model to make the calculations easier. To calculate the fuel consumption rate, the eddy dissipation and reaction kinetics models were implemented in conjunction with each other without considering turbulent disturbances. The universal governing equations for the conservation of energy, mass, momentum and species transport can be defined as follows:

Continuity equation (mass conservation):

$$\frac{\partial \vartheta_r}{\partial r} + \frac{\vartheta_r}{r} + \frac{1}{r}\left(\frac{\partial \vartheta_\theta}{\partial \theta}\right) + \frac{\partial \vartheta_z}{\partial z} = 0 \tag{4.1}$$

Momentum equation in θ-axis:

$$\rho\left(\frac{\partial \vartheta_\theta}{\partial t} + \vartheta_r \frac{\partial \vartheta_\theta}{\partial r} + \frac{\vartheta_\theta \partial \vartheta_\theta}{r\partial\theta} + \frac{\vartheta_r \vartheta_\theta}{r} + \frac{\vartheta_z \partial \vartheta_\theta}{\partial z}\right) = -\frac{\partial p}{r\partial\theta} + \mu\left(\frac{\partial^2 \vartheta_\theta}{\partial r^2} + \frac{\partial \vartheta_\theta}{r\partial r} - \frac{\vartheta_\theta}{r^2} + \frac{\partial^2 \vartheta_\theta}{r^2\partial\theta^2} + \frac{2\partial \vartheta_r}{r^2\partial\theta} + \frac{\partial^2 \vartheta_\theta}{\partial z^2}\right) \tag{4.2}$$

Momentum equation in X-axis:

$$\rho\left(\frac{\partial \vartheta_x}{\partial t} + \vartheta_r \frac{\partial \vartheta_x}{\partial r} + \frac{\vartheta_\theta \partial \vartheta_x}{r\partial\theta} + \frac{\vartheta_x \partial \vartheta_x}{\partial x}\right) = -\frac{\partial p}{\partial x} + \mu\left(\frac{\partial^2 \vartheta_x}{\partial r^2} + \frac{\partial \vartheta_x}{r\partial r} + \frac{1}{r^2} + \frac{\partial^2 \vartheta_x}{r^2\partial\theta^2} + \frac{\partial^2 \vartheta_x}{\partial x^2}\right) \tag{4.3}$$

Energy equation:

$$\rho c_p\left(\frac{\partial T}{\partial t} + \vartheta_r \frac{\partial T}{\partial r} + \frac{\vartheta_\theta \partial T}{r\partial\theta} + \frac{\vartheta_z \partial T}{\partial z}\right) = k\left[\frac{\partial}{r\partial r}\left(\frac{r\partial T}{\partial r}\right) + \frac{\partial^2 T}{r^2\partial\theta^2} + \frac{\partial^2 T}{\partial z^2}\right] \tag{4.4}$$

WED combustion can be written as:

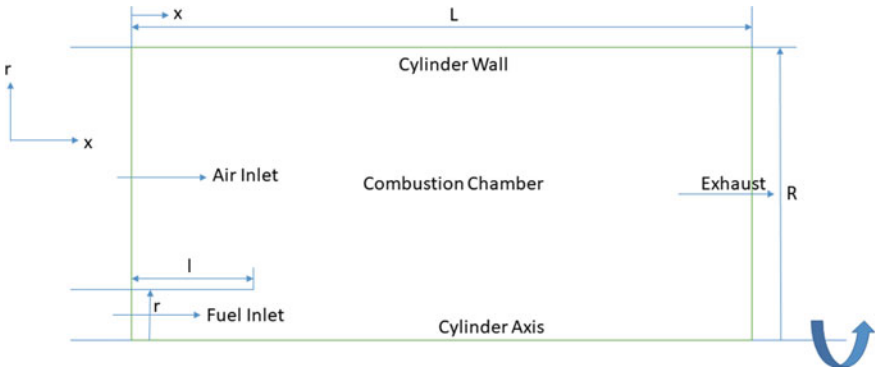

Fig. 4.1 Schematic—geometry of the combustion chamber

Table 4.1 Combustion chamber geometry dimensions

Cylinder length (L)	79.5 mm
Cylinder radius (R)	37.5 mm
Fuel nozzle radius (r)	0.10 mm
Fuel nozzle protrusion length inside cylinder (l)	2 mm

$$C_{10}H_{22} + uC_2H_5OH + vH_2O + w(O_2 + 3.76N_2) = n_{CO}CO + n_{CO_2}CO_2 + n_{H_2O}H_2O + n_{N_2}N_2 + n_{O_2}O_2 + n_{NO}NO + n_{NO_2}NO_2 + n_{N_2O}N_2O + n_{SO_2}SO_2 + n_{HC}HC + n_C C + n_{H_2}H_2 + n_H H + n_O O + n_{OH}OH + n_N N \quad (4.5)$$

where u, v and w are the amount of ethanol, water and air per kmol of emulsified fuel and n_i represents the number of by-product species moles of i in kmol.

This model was prepared and analyzed in fluent module of CFD Ansys software.

4.3 Geometry Measures

In the present study, the model geometry has been used for a diesel engine combustion chamber. The geometry details (length and diameter), inlet and outlet conditions and axis-symmetry have been represented in Fig. 4.1. Table 4.1 displays the combustion chamber geometry dimensions.

4.4 Solution Procedures

The boundary conditions of combustion chamber were defined for all zones such as axis, wall, and inlet mass flow rates for air and fuel and pressure outlet. The cylinder wall, air and fuel inlet temperatures were taken constant as ambient atmospheric

temperature 303 K. The model was made in 2D dimensions to make it less complex. Ansys software (Fluent module) was selected to make the geometry of the combustion chamber model.

Ansys Fluent software has been used for simulations, geometry creation and mesh formation to study the air-fuel flow behavior inside combustion chamber model (Govindan et al. 2014). The convergence criterion for kinetic energy, continuity, momentum and energy has been selected as 10^{-3}. In the current study, the non-premixed combustion has been used with inlet diffusion model to model combustion of air-fuel mixture. The inlet mass flow rate of air is 0.0551 kg/s while for fuel is 2.66 kg/s. The higher mass flow rate of fuel denoted the injection of fuel from fuel nozzle which is very small opening compared to air opening. A small opening increased the velocity of fuel flow and permitted the higher amount of fuel in given time. The flow of air and fuel is assumed only in axial direction. The turbulent intensity is used as 10% and hydraulic diameter 0.0347 m according to specifications of combustion chamber.

The air inlet species is used in terms of mass fractions means 23% oxygen and 77% nitrogen in the inlet air. The cylinder wall temperature is assumed constant of 303 K so heat generation rate has been neglected in this study. The cylinder wall is assumed as stationary wall similar to combustion chamber cylinder of real CI engine without considering any slip as shear condition. The cylinder wall roughness height is neglected with roughness constant of 0.5. The fuel inlet species included diesel ($C_{10}H_{22}$), mixture of water (H_2O) and diesel, mixture of ethanol (C_2H_5OH) and diesel, mixture of water, ethanol and diesel. The fuel species has been taken in mass fractions. All the fuel species, inlet fuels and combustion by products have been added or selected into fuel species library. The combustion by products are O_2, CO_2, H_2O and N_2. Fuel species can be searched via their chemical formula. Total nodes are 40,401 in the designed mesh. Mesh type is tetrahedral to make the calculations easier and flow of air-fuel mixture to be smooth. The advanced sizing function option is kept off as geometry model is considered 2-dimensional and simple. The relevance center is selected as fine. The smoothing has been put in high mode during meshing to make the mesh as smooth as possible (Burnete 2017). The radiation, acoustic and heat exchange effect is neglected in this study.

Elaborated model is standard k-epsilon viscous turbulent flow model and species transport model with eddy dissipation. The different mesh sizes were used for mesh independency test those were 200 × 200, 250 × 250, 300 × 300, 350 × 350, 400 × 400 and 450 × 450 out of which 250 × 250 was selected. So used cell size in the present model is 250 × 250. The species transport model is selected to predict emissions of NO_x, SO_x and soot (Burnete 2017; Sharath and Ajith 2016; Subramaniam et al. 2017; Varghese and Karunanidhi 2015). Fuel NO_x is not considered for calculations and results because fuel is considered free from nitrogen. Thermal and prompt NO_x are considered to show the NO_x emission results. Thermal NO_x is generated due to high combustion temperature while prompt NO_x is formed via high reaction rate between fuel and air. The patch function has been used to ignite the fuel-air mixture in the flow domain zone which is a necessary requirement to study the combustion phenomenon. Patch temperature is selected as

2500 K at nearby section of fuel inlet. In the patch zone, shapes of flow particles is considered quadrilateral and very small area (0.001×0.001 mm^2) is considered.

The absolute convergence criterion is selected in the residual monitors section. The pseudo transient explicit relaxation factors are considered for pressure, momentum, density, body forces, turbulent kinetic energy, turbulent dissipation rate, turbulent viscosity, $C_{10}H_{22}$, O_2, CO_2, H_2O, soot, NO and energy as 0.5, 0.5, 1, 1, 0.75, 0.75, 1, 0.75, 0.75, 0.75, 0.75, 0.75, 0.75 and 0.75 respectively. The hybrid initialization has been used as initialization method to initialize the solution. In solution methods, pressure-velocity relations are considered to be coupled. The least square cell based gradient is selected under spatial discretization. The second order pressure, momentum, turbulent kinetic energy, and turbulent dissipation rate have been considered. The pseudo transient is activated to make the calculations and results more smooth and accurate. The process parameters have been selected as default for two-step soot model. The standard k-epsilon model is selected with standard wall functions using default model constants.

4.5 Results and Discussion

4.5.1 Diesel Combustion

Figure 4.2, Fig. 4.3, Fig. 4.4 and Fig. 4.5 show the temperature, CO_2, NO_x and soot for diesel combustion, respectively. Figure 4.2 display the temperature of gas (gas produced by burning of diesel fuel mixed into air) in the chamber for diesel fuel combustion. As per the results shown, the maximum temperature has been occurred in the initial zone in radial direction. The combustion temperature has not shown significant change in the axial direction. The emission of CO_2 from diesel combustion is shown in Fig. 4.3. According to figure, the maximum emission of CO_2 was occurred in the initial zone along the radial direction of the combustion chamber.

Fig. 4.2 Temperature distribution contour for diesel

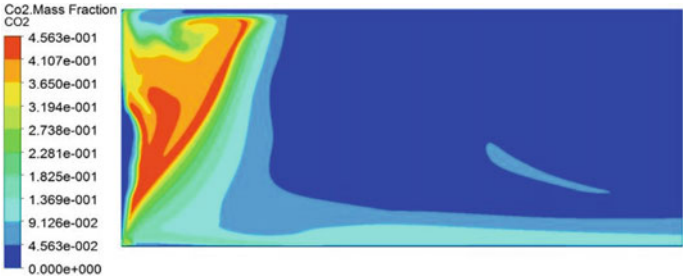

Fig. 4.3 CO_2 contour for diesel

Fig. 4.4 NO_x contour for diesel

Fig. 4.5 Soot contour for diesel

In the middle and outer zone, CO_2 emissions happens almost zero or non-significant along both the directions, radial and axial (Burnete 2017).

Figures 4.4 and 4.5 represent the emissions of NOx and soot generated from the combustion of diesel where it can be observed that maximum production rate of these emissions occurs only in small inlet area of the combustion chamber while the other areas of combustion chamber are not affected by these emissions. Since soot and NO_x generation is dependent on the combustion temperature inside the cylinder, it can be clearly noticed that the maximum soot and NO_x is occurred at the maximum combustion temperature area.

4.5.2 *Water-Diesel Emulsion Combustion*

In water-diesel emulsified fuel, water is mixed with the diesel in the proportion of 10% with remaining diesel. The water-diesel emulsified fuel containing 10% water is designated as W10D90. Figure 4.6, Fig. 4.7, Fig. 4.8 and Fig. 4.9 show the temperature, CO_2, NO_x and soot for W10D90 emulsion respectively. Similar to diesel combustion, water-diesel emulsified fuel reacts instantly as the combustion starts and this can be reported that the mass fraction of water-diesel emulsified fuel was propagated only at inlet of combustion chamber.

According to Fig. 4.6, the highest combustion temperature takes place at inlet section of the combustion area and a relatively the lowest range of temperatures across the cylinder can be reported. The CO_2 mass fraction distribution is represented in Fig. 4.7. CO_2 has the highest concentration at starting of the combustion area of the chamber while it's showing moderate level along the axial direction but no effect along radial direction throughout the combustion cylinder. Figure 4.8 and Fig. 4.9 show the mass fraction of NO_x and soot, respectively. On the basis of results obtained, the maximal soot generation occurs at intake of the combustion chamber, but it has nil effect (zero soot) in all other parts of combustion cylinder. In the starting phase of combustion, more soot is formed because it takes a little time to achieve required

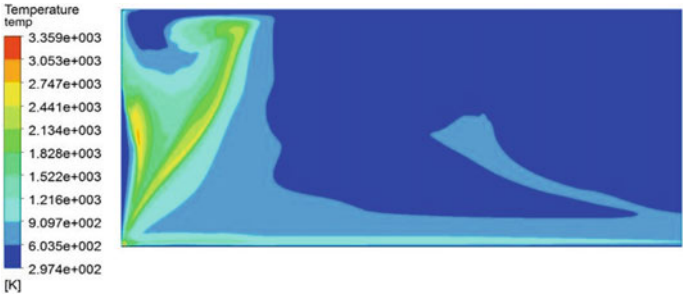

Fig. 4.6 Temperature distribution contour for W10D90 emulsion

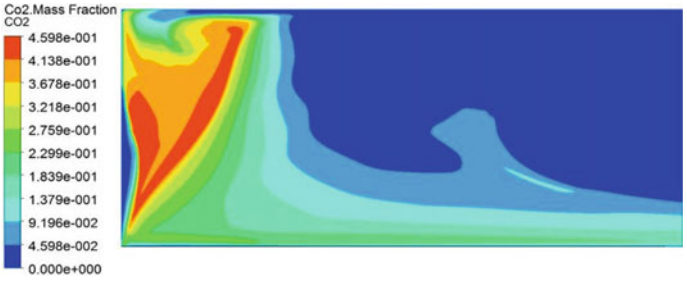

Fig. 4.7 CO_2 contour for W10D90 emulsion

Fig. 4.8 NO_x contour for W10D90 emulsion

Fig. 4.9 Soot contour for W10D90 emulsion

pressure or temperature for complete combustion of fuel. The same pattern was followed by the NO_x formation.

4.5.3 Ethanol-Diesel Emulsion Combustion

In ethanol-diesel emulsified fuel, ethanol is mixed with the diesel in the proportion of 10% with remaining diesel. The ethanol-diesel emulsified fuel containing 10% ethanol is designated as E10D90. Figure 4.10, Fig. 4.11, Fig. 4.12 and Fig. 4.13 show the mass fraction of E10D90, temperature, CO_2, NO_x and soot, respectively.

According to Fig. 4.10, the highest combustion temperature occur form the starting to middle of the combustion chamber and a moderate level of temperature is reported after the middle section. The CO_2 mass fraction distribution is represented in Fig. 4.11. CO_2 has almost similar pattern like temperature distribution contour while its maximum range covers more area of combustion chamber than highest temperature area. The reason behind this could be more complete combustion. Figure 4.12 and Fig. 4.13 show the mass fraction of NO_x and soot, respectively. According to results, the maximal soot generation area is shifted from inlet to outlet means soot formation does not take place at inlet which indicated smooth combustion, but it has nil effect (zero soot) in all other parts of combustion cylinder. Only a little NO_x of

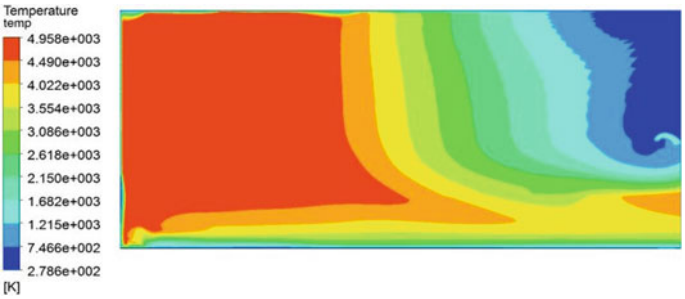

Fig. 4.10 Temperature distribution contour for E10D90 emulsion

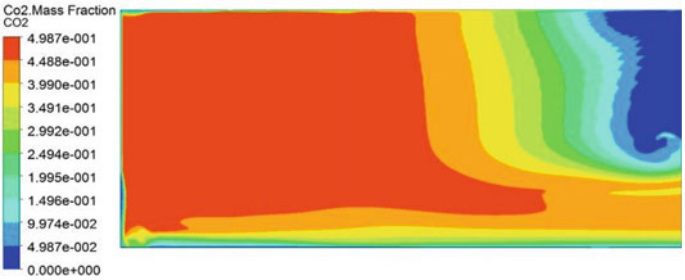

Fig. 4.11 CO_2 contour for E10D90 emulsion

Fig. 4.12 NO_x contour for E10D90 emulsion

Fig. 4.13 Soot contour for E10D90 emulsion

minimal value was observed at the boundary of combustion chamber (Sharath and Ajith 2016; Varghese and Karunanidhi 2015).

4.5.4 Water-Ethanol-Diesel Emulsion Combustion

In water-ethanol-diesel emulsified fuel, water and ethanol is mixed with the diesel in the proportion of 10% each with remaining 80% diesel. The water-ethanol-diesel emulsified fuel containing 10% ethanol and 10% water is designated as W10E10D80. Figure 4.14, Fig. 4.15, Fig. 4.16 and Fig. 4.17 show the mass fraction of W10E10D80, temperature, CO_2, NO_x and soot, respectively.

According to Fig. 4.14, the temperature distribution contour shows the highest combustion temperature at first half area from starting and then in a decreasing pattern afterwards in axial direction, exactly similar to Fig. 4.10. The CO_2 mass fraction distribution is depicted in Fig. 4.15. CO_2 mass fraction contour for W10E10D80 looks like CO_2 mass fraction contour of E10D90 as shown in Fig. 4.11 where most of the area of combustion chamber shows highest temperature range. It could be owing to complete combustion. Figure 4.16 and Fig. 4.17 show the mass fraction of NO_x and soot, respectively. According to results, the soot generation area for

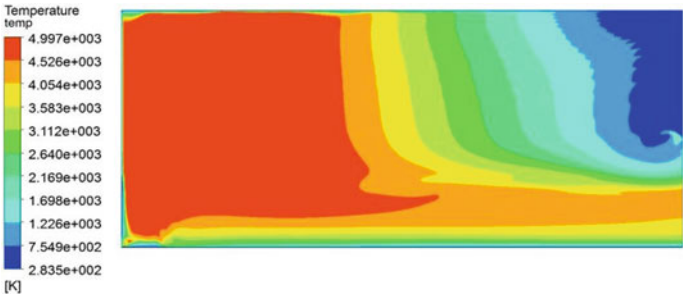

Fig. 4.14 Temperature distribution contour for W10E10D80 emulsion

Fig. 4.15 CO_2 contour for W10E10D80 emulsion

Fig. 4.16 NO_x contour for W10E10D80 emulsion

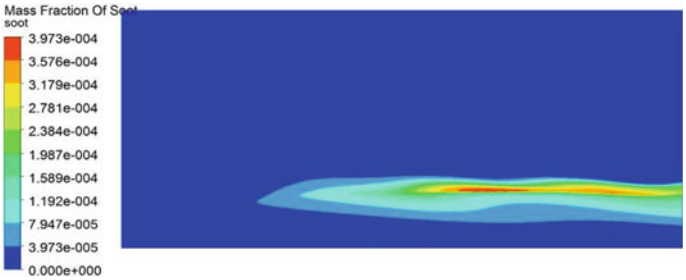

Fig. 4.17 Soot contour for W10E10D80 emulsion

W10E10D80 is increased compared to E10D90, W10D90 and diesel. It has shown effect only in the axial direction of chamber. NO_x is almost zero or minimal value compared to all other blends.

4.6 Validation with Literatures

Sharath and Ajith (2016) achieved the similar pattern of temperature distribution for diesel and E10 blend. They showed more area of maximum temperature with 10% ethanol blending into diesel. They have reported a small NO_x area for diesel and E10 blends similar to the present work.

Varghese and Karunanidhi (2015) have shown similar soot pattern for ethanol-diesel blend, maximum at the piston head and then decreasing up to the cylinder head.

Fernandez (2015) has presented similar results of mass fraction of NO_x for water-diesel fuel blends and concluded that increasing water concentration reduced the formation of NO_x.

4.7 Conclusions

This chapter presented a numerical investigation on combustion of water-ethanol-diesel emulsified fuel into diesel engine using CFD software Ansys (Fluent Module). The different fuel combinations; diesel, diesel-water, diesel-ethanol, and water-ethanol-diesel emulsions were selected and effects on combustion temperature, CO_2, NO_x, and soot were analyzed. Diesel emulsified fuel seemed to be better alternative fuel owing to its superior combustion and lowering emissions characteristics. Induction of water into diesel reduced the combustion temperature because of higher vaporization latent heat (cooling effect) which further resulted in lower NO_x. Soot is increased for water-ethanol-diesel emulsified fuel compared to water-diesel, ethanol-diesel emulsions. Blending of ethanol in ethanol-diesel and water-ethanol-diesel emulsions increased temperature distribution inside combustion chamber improved mass fraction of CO_2 which indicated better combustion of above said fuels. It could be possible to use diesel emulsified fuel with little modification to the diesel engine. The micro explosion combustion phenomenon improved the combustion of presented emulsified fuel.

References

Anton N, Vandamme TF (2010) Nano-emulsions and micro-emulsions: clarifications of the critical differences. Springer Science Business Media, LLC

Becher P (1965) Emulsions: theory and practice. Reinhold, New York

Bibette J, Leal-Calderon F, Poulin P (1999) Emulsions: basic principles. Rep Prog Phys 62(6)

Burnete NV (2017) Separate direct injection of diesel and ethanol: a numerical analysis. Therm Sci 21(1B):451–463

Cook DH, Law CK (1978) Combust Sci Technol 18:217

Dewulf J, Van Langenhove H (2006) Renewable-based technology: sustainability assessment. Wiley

Fernandez JMI (2015) Study of combustion using computational fluid dynamics software (ANSYS). Master's thesis, University of Barcelona

Gilbert R, Perl A (2008) Transport revolutions: moving people and freight without oil. Earthscan

Govindan R, Jakhar OP, Mathur YB (2014) Computational analysis of Thumba biodiesel-diesel blends combustion in CI engine using Ansys-Fluent. Int J Comput Math Sci 3(8):29–39

Heywood JB (1988) Internal combustion engine fundamentals. McGraw-Hill, New York

Hussain SM, Kumar SP, Reddy VK (2012) CFD analysis of combustion and emissions to study the effect of compression ratio and biogas substitution in a diesel engine with experimental verification. Int J Eng Sci Technol 4(2):473–492

Palaniswamy D, Ramesh G, Sivasankaran S, Sooryaprakash K (2016) CFD analysis for homogenous effect of biogas and air in the intake manifold of dual fuel CI engine. Int J Adv Eng Technol 7(2):265–268

Sharath P, Ajith K (2016) Experimental and CFD analysis of combustion in diesel engine for various ethanol-diesel blends. Int J Sci Res 5(5):1800–1805

Shirneshan A, Jamalvand H (2016) Numerical investigation of combustion of biomass, methane, and gasoil fuels and emissions from a furnace chamber. Energy Policy Res 3(1):19–26
Subramaniam VS, Vinayak SG, Prashanth K (2017) Performance optimization of a single cylinder 4-stroke diesel engine using biodiesel fuel. Int J Mech Prod Eng 5(4):5–8
Varghese M, Karunanidhi G (2015) CFD analysis and experimental validation of ethanol diesel blend in CI engine. Int J Latest Res Eng Technol 1(1):10–14

Part III
Optical Diagnostics in IC Engines

Chapter 5
Optical Diagnostics of Spray Development in Diesel Engines

Ashutosh Jena

Abstract In order to comply with the current and future emission norms applicable to diesel engines, understanding the fuel-air mixing phenomena in depth is quite crucial. Fuel spray inside the cylinder of an engine in operation interacts with in-cylinder gases as well as with solid boundaries. Fuel spray impinging on the cylinder wall and piston top, may subsequently enhance soot formation and hence, study and analysis of fuel spary characteristics can help to minimize these effects. However, study of the physics of spray evolvement and dynamics demands advanced diagnostics and numerical techniques. Many attempts have been made in developing computational models for analyzing the fuel-air and fuel-wall interactions. Despite those efforts it remains an exciting area of research to accurately model the spray behavior under dynamic conditions inside the engine cylinder. These models need continuous inputs from experimental studies for validation and for further development purposes. For experimental investigations point of view, several optical methods have been adopted viz. Phase Doppler Interferometry (PDI), Shadowgraphy, Schlieren photography etc. However, deployment of these techniques for acquiring precise and reliable data requires certain expertises. The aim of this chapter is to confine various optical diagnostics techniques applicable to diesel engines. A critical review of these methods has been presented for further advancement in the field.

Keywords Spray wall impingement · Optical diagnosis · Diesel engines

5.1 Introduction

5.1.1 Spray Wall Impingement: Causes and Consequences

In Direct Injection diesel engines and Gasoline Direct Injection (GDI) engines, fuel spray may penetrate longer than the dimension of the combustion chamber. This

A. Jena (✉)
Department of Mechanical Engineering, Indian Institute of Technology Kanpur, Kanpur 208016, UP, India
e-mail: asutosh@iitk.ac.in

A. P. Singh et al. (eds.), *Simulations and Optical Diagnostics for Internal Combustion Engines*, Energy, Environment, and Sustainability,
https://doi.org/10.1007/978-981-15-0335-1_5

leads the fuel droplets to interact with the wall, and a wall film may be formed (Mathews et al. 2013). The phenomenon of spray touching the cylinder wall or combustion chamber wall is termed as spray wall impingement.The probability of spray wall impingement is higher for small bore engines during cold starting conditions and for engines with early injection strategies (Werlberger and Cartellieri 1987); Tang et al. 2017. Figure 5.1 shows the typical diesel spray impinging on piston bowl and cylinder liner.

In order to resolve the soot-NO_x tradeoff, many new and innovative developments in engine combustion strategies have been proposed and put into practice. Engine downsizing has been given priority to improve fuel economy. On the other hand, injection pressure is on the rise through CRDI technology to promote better fuel

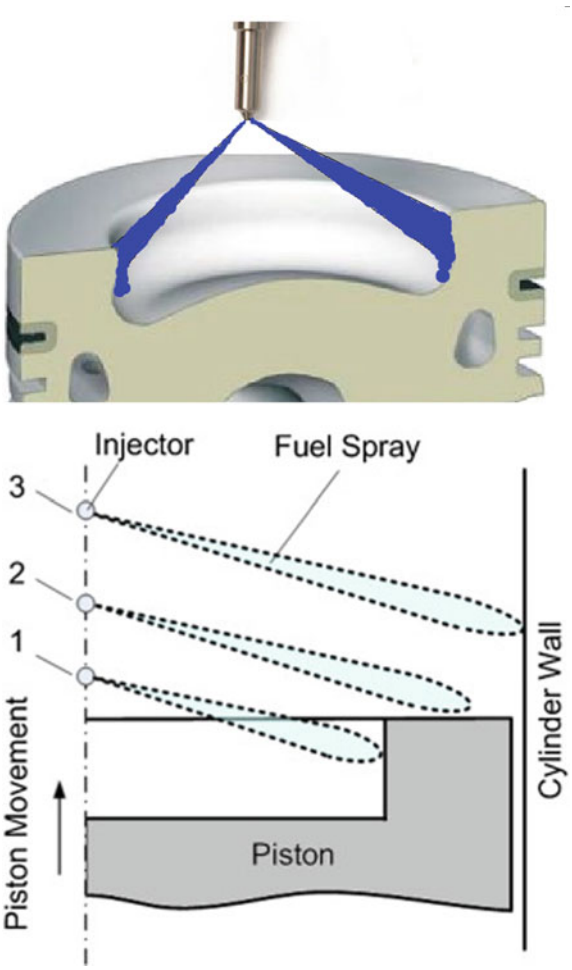

Fig. 5.1 Spray impingement on piston bowl and cylinder wall (Tang et al. 2017)

atomization. Combined effect of both these strategies tends to increase the probability of spray impingement on piston bowl. In a recent study (Wang et al. 2011), use of ultra-high injection pressure of 300 MPa with microhole nozzle (0.08 mm) demonstrated a deeper penetration of the spray tip into the combustion chamber, and significant spray impingement on piston bowl. This condition is thus almost inevitable in downsized diesel engines operating with high injection pressures. Borman and Nishiwaki (1987) studied the effect of wall heat transfer of impinging flames and reported that at least 30% of the total heat loss was due to the flames touching the piston cavity. Due to the wall-impingement of flame, heat transfer to the piston increased, which led to a decrease in thermal efficiency as a consequence of higher heat loss.

Advanced combustion technologies such as homogeneous charge compression ignition (HCCI) and premixed charge compression ignition (PCCI) require advanced injection timing in order to provide adequate time for homogeneous air-fuel mixture preparation (Yao et al. 2009; Berggren and Magnusson 2012; Musculus et al. 2013; Mwangi et al. 2015). However, this exposes cylinder liner to the spray. Relatively low gas density increases spray tip penetration, which may dilute the lube oil leading to more harmful pollutant formations (Kook et al. 2007); Kitasei et al. 2008. It has been reported by previous studies that HCCI and PCCI diesel engines generally suffer from increased soot, CO (carbon monoxide) and HC (Hydrocarbon) emissions as a consequence of wall impingement. Fuel deposited on piston bowl due to early injection resulted in increased particulate matter (PM) emission (Benajes et al. 2012).

These increased emissions as a result of spray wall impingement can be attributed to two aspects:development of rich fuel/air mixture in the vicinity of the film (Peng et al. 2011; Yu et al. 2015) and a phenomenon called pool fire also occurs in the piston cavity (Fang and Chia-fon 2011). Early injection also causes liner oil film dilution, which results in oil loss (Jia et al. 2009). In recent years, substantial research efforts have been made to resolve the issue of wall impingement so that the stringent emission requirements can be met.The phenomenon can be broadly understood by two processes: splash process, and wall film formation.

The physics behind the occurrence and growth of wall film need to be understood in order to design an efficient combustion chamber and injection equipment. However, this is a complex phenomenon since it involves a number of geometric and physical parameters. Injection pressure is one of the key parameters that influences the phenomenon has been studied extensively. Increasing injection pressure increases the area of impingement film due to an increase in impact velocity (Abo-Serie et al. 2003; Park and Lee 2004). This, in turns, increases the number density of small-sized droplets (Meingast et al. 2000). Liquid film growth can be mitigated by utilizing and optimizing multiple short injections (Stanton et al. 1998; Nhumaio and Watkins 2005).

The distance of impingement cavity from the injector tip also plays a major role because the impact momentum of droplets varies with it (Su 1999). Sufficient time for air entertainment into the spray promotes vaporization, which reduces the adhered fuel mass (Meingast et al. 2000). The velocity and angle of spray impingement also

affects the dynamics of film formation. By analyzing mean velocity field of the post-impingement spray using Particle image velocimetry (PIV) technique, Zama et al. (2014) concluded that the impinging droplet momentum played a key role in wall film formation and adhered mass decreased with increase in inclination angle. Very few studies have investigated the effect of the presence of oil film on the impingement wall. Seel et al. (2015) performed experiments on an impingement disc with lube oil film and found a significant rise in the count of small-sized fuel droplets. Other study showed a strong dependence of impingement film stability with initial oil film thickness (Seel et al. 2018).

From the above discussion, it is clear that spray-wall interaction is a complicated phenomenon and plays a vital role in the combustion process and thus in thermal efficiency and emissions of modern IC engines. Because of such complicated physics, developing an accurate physical model would rely on fundamental experiments. Optical techniques being the most promising method have provided a deep insight into the spray-wall interaction process in this context.

5.2 Heat Transfer Evaluation Due to Wall Impingement

Study of heat loss through cylinder walls and piston cavity has great importance since it directly affects thermal efficiency of the IC engines. By improving combustion efficiency and decreasing heat loss, higher thermal efficiency can be achieved. Spray wall impingement affects both the quality of combustion and heat loss through the cylinder wall. Hence, predicting the mechanism of heat transfer accurately under these conditions holds the key to efficient design of combustion chamber and injection strategies.

Over the years, many attempts have been made to develop empirical correlations for estimating the heat transfer coefficient. However, when applied to the engine in-cylinder conditions, these correlations may differ by up to 200% (Woschni 1967), which limits their application for practical design purposes. Hohenberg (1979) has developed a correlation to determine instantaneous heat flux after conducting extensive studies on DI diesel engine, which has been applied successfully in combustion analysis.

$$h_C = \frac{130 \times P_{cy}^{10.8} \times (u_p + 1.4)^{0.8}}{V_{inst}^{0.06} \times T_{cyl}^{0.4}} \tag{5.1}$$

h_c Heat transfer coefficient
u_p Piston velocity
V_{inst} Instantaneous cylinder volume
T_{cyl} Temperature of the in-cylinder gases

The instantaneous heat transfer coefficient then can be used to accurately determine the instantaneous heat flux by the expression given below (Babu and Murthy 1976).

$$\frac{dQ}{d\theta} = Ahc(Tcyl - Twall)\left(\frac{1}{6N}\right)$$

A Instantaneous surface area
T_{wall} Wall temperature

Woschni (1967) has developed an accurate correlation for predicting heat transfer coefficient in the impingement location inside the combustion chamber. This heat interaction is involved in NOx formation mechanism and hence, it is very helpful and widely accepted for combustion chamber design. The Woschni correlation is given below,

$$h_C = C^* L^{-0.2} P_{cyl}{}^{0.8} u_{wall}{}^{0.8} T_m{}^{-0.35} \tag{5.2}$$

where

h_c Coefficient of heat transfer
C* Constant
L Characteristic length/impinged film diameter/mean diameter of ring
P_{cyl} Ambient pressure, bar
u_{wall} Impinging spray velocity, m/s
Tm Mean temperature of outer and inner boundaries of the ring section

The foot of the impinging spray is subdivided into several annular rings, as shown in Fig. 5.2. For every annular segment, mean temperature and heat flux are calculated. Integration is performed over the entire domain to obtain the total heat flux.

$$h_{f,\,ring} = hc\,(T_m - T_p) \tag{5.3}$$

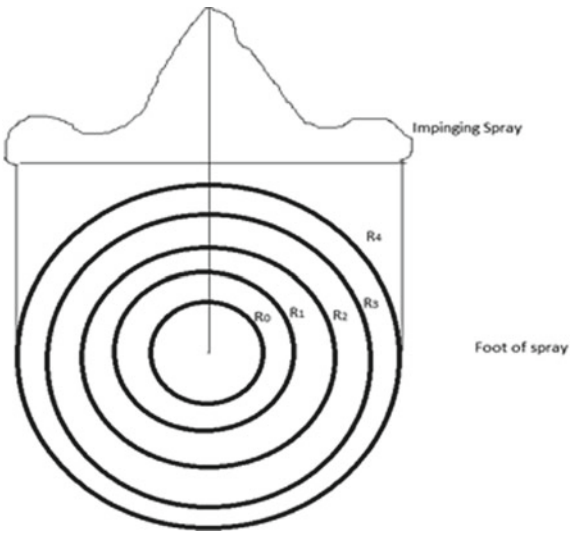

Fig. 5.2 Annular sections of wall film approximated as a circle

$$h_{ring} = \sum h_{f,\ ring} A_{ring} \tag{5.4}$$

where,

$h_{f,\ ring}$ Average heat flux for an annular section
T_p Piston temperature, K
$h_{t,\ ring}$ Average heat transfer for annular section
A_{ring} Area of an annular division

These empirical correlations help to develop simulation models and to predict heat losses in transient condition.

Experimental determination of heat flux in IC engine environment is a complicated process. Study of heat flux on wall-impinging flames has been done mostly in a Constant Volume Combustion Chamber (CVCC). Mahmud et al. (2018) used Alumel/Chromel Thin Film Thermocouples Heat Flux (TFTHF, Medtherm 10702B) sensors to measure the instantaneous heat flux of impinging spray. Each of such sensors was made up of two thermocouples in pair. One was placed at the surface concerned and other was at a depth of 3.3 mm from the surface. One dimensional transient heat transfer equation was used to calculate the temperature distribution. Finite difference approach was used to solve the equation, and transient data from TFTHF was used as a boundary condition. The temperature distribution so obtained was then used for calculating the heat flux. However, Infrared Thermography can be used to obtain the temperature distribution directly over the desired zone (Schulz et al. 2011). A simpler alternative can be a series of K-type thermocouples embedded beneath the impinging plate. However, this approach has been adopted in a spray cooling study, which can be explored further (Nayak et al. 2016). Serras-Pereira et al. (2013) used a Vetell made Fast-response heat flux sensor to obtain heat flux data. The heat flux sensor location varied in angular position on liner at a certain depth from the injector tip in an Optical DI engine, where the probability of spray impingement was maximum. The tests were conducted for both static (non-motoring quiescent ambient conditions) and motoring modes.

5.3 Optical Diagnosis Technique

Over the last few decades, notable developments in spray measurement have been reported. Accurately quantifying the spray behavior helps in developing improved spray model for simulation. With the advancement in computing, imaging, and laser technology, optical diagnostics techniques have emerged as an excellent tool to provide reliable results regarding spray physics. The two common optical methods for study of fuel spray impingement that has been commonly adopted by the researchers are: Schlieren photography and Phase Doppler interferometry (PDI).

5.3.1 Schlieren Photography

5.3.1.1 Basic Principle

Schlieren imaging has emerged as a rather simple and effective optical technique over the years. Especially for diesel injection, to visualize vapor phase of the spray, this is a very effective tool. Many investigations have been aimed to study transient behavior of vapor phase and impinging jets in both inert and reactive environment. Schlieren imaging technique is useful to study the macroscopic parameters such as spray penetration length, cone angle, impingement area, and growth of spray (Payri et al. 2016; Ismael et al. 2014; Tschöke and Marohn 2017). However, researchers have also successfully used this technique to study more complicated parameters like ignition delay and liftoff length (Payri et al. 2015; Payri et al. 2016; Tschöke and Marohn 2017).

Schlieren photography method uses a collimated light beam for visualization of the test section. The light beam suffers deflection from its path while passing through a medium having gradients in refractive index. This gradient arises due to variation in density through the medium. Figure 5.3 shows the schematic of basic components commonly usedin this method.

Schlieren edge (e.g., a knife-edge) is placed at the point of formation of the image. This edge blocks some amount of light coming from the source. The amount of light blocked by the edge depends upon its relative position to the axis of lens/mirror. The schlieren image is captured on a screen, which is placed after the edge. The intensity of this image varies with location (in the vertical axis) of edge. When the knife edge moves closer to the optical axis progressively, more amount of light is covered, and the undisturbed image gets darker. The sensitivity of a schlieren setup is a strong function of the position of edge.

When a light beam passes through a varying density medium, it may bend towards the edge or away from it. Nature of deflection depends on the nature of density gradient. When light is deflected towards the edge, the image gets darker. When it deviates away, the image becomes brighter relative to the case when edge is absent. Two optical components provide flexibility to have the measurement regime anywhere along

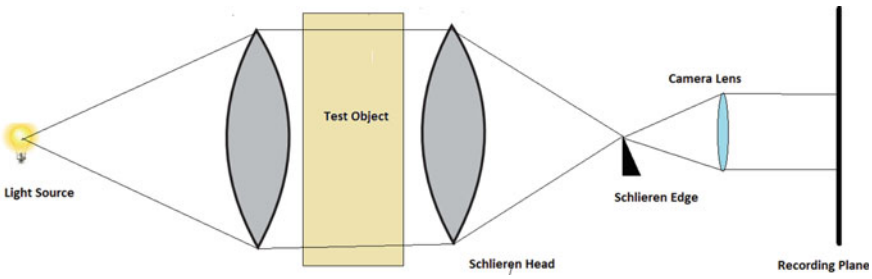

Fig. 5.3 Schematic of a typical Schlieren setup

the axis. Though lenses can be used, high-quality mirrors are preferred because of their availability.

Light source plays a key role in determining the sensitivity of entire setup. Sensitivity is inversely proportional to the wavelength of the light. The point source of light should be at the focal point of mirror/lens. The incident angle of light beam should be minimized to avoid beam straightening (Payri et al. 2016; Pastor et al. 2012). Spark flashlight, and Xe Arc lamp, have been used as light source for visualization of fuel sprays by the researchers (Cardenas et al. 2008; Du et al. 2018). Payri et al. (2015) have used a 150 W halogen lamp for spray visualization. Mercury and Sodium discharge lamps are other options suitable for schlieren visualization.

Schlieren edge can be of two types:knife edge; suitable for a rectangular light source, and circular opening; suitablefor circular source. Knife edge has limitations to capture gradients in one direction. On the other hand, circular opening can visualize gradients in all directions. Furthermore, circular opening is suggested to define and measure the spray boundary accurately (Pastor et al. 2012). Diameter of circular opening can be varied to obtain a satisfactory result. For high-quality visualization, edge should be located precisely at the focal point of optical component, which makes the screen homogenously darker from all sides when edge moves closer to the path of beam. By successive adjustments, an accurate location can be obtained.

There are a few key points that need to be considered: (i) parallel beam from the source must pass through investigation volume, (ii) proper alignment of camera lenses, camera, and circular edge. To ensure the beams are parallel, a simple screen can be moved along the beam path. Diameter of the bright disc on screen will not change for parallel beam. If the beam is not parallel, distance between light source and mirror needs to be adjusted. To have good collection angle, lens is placed as close as possible to the injector axis. Focus of camera should be perfect at the spray plane at desired shutter speed of camera. To ensure alignment of camera with beam, reflection of camera diaphragm and diaphragm of the source should perfectly overlap each other.

5.3.1.2 Effect of the Clustered Orifice on Wall Interaction

Cardenas et al. (2008) have studied the spray-wall interaction using clustered orifice and schlieren imaging technique. Ambient pressure and temperature condition were set at 50 bar and 800 K, respectively. Three different walls were used in the investigation viz. flat wall, straight divided wall, and a slant divided wall as shown in Fig. 5.4. Details of the nozzle investigated are given in Table 5.1. All nozzles had identical pressure difference of 100 bar and two nozzles 0.6 mm apart, form one cluster.

For similar wall orientations, images from cluster nozzles were captured. These images were then further processed to obtain spray widths for each case. It was observed that after impingement, spray width of the clustered nozzle decreased. This suggests a decrease in momentum of the wall jet. Due to loss in momentum of fuel droplets more accumulation takes place near the wall and richer mixer is formed leading to soot formation in engines.

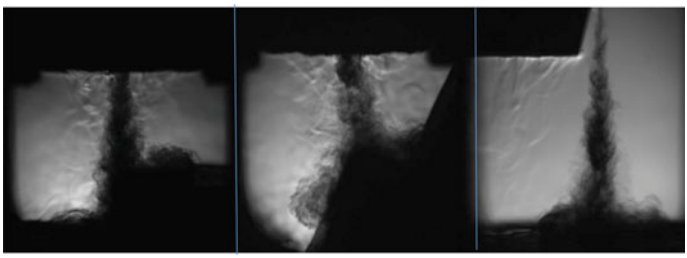

Fig. 5.4 Schlieren image of impinging spray from a conventional nozzle on (from left) straight devided wall, slant devided wall and flat wall (Cardenas et al. 2008)

Table 5.1 Injector specification

Number of orifices	Angle between cluster sprays	Orifice diameter (μm)
3	–	131
3 × 2	10°	93
3 × 2	20°	93

5.3.1.3 Pressure Dependence Study of Impinging Spray

High-pressure injection helps to achieve better atomization of fuel spray, but at the same time increased momentum makes the spray more prone to wall impingent. Hence, injection pressure is a key parameter to monitor for better understanding the formation of wall film. Du et al. (2018) have studied the effect of injection pressure on spray morphology after impingement in a CVCC. Schlieren technique was used to study the vapor phase structure of the spray impingement. Macroscopic features of the spray viz. film radius, height, area were calculated for both liquid and vapor phase. Injected mass was kept constant and the pressure was varied between 40 to 160 bar in steps of 20 bar throughout the study, Optical setup included in this study a Phantom V7.3 camera with a maximum acquisition rate of 20 k fps and a Xe-arc lamp.

The authors reported that the impingement radius first increased and then decreased with pressure. Increase in radius can be attributed to increased momentum of droplets, which is transferred to the film. After a certain point, increased pressure causes smaller droplet formation, which in turn increases evaporation rate, and the radius starts to diminish. By optimisation of injection pressure minimum film thickness and film area can be achieved.

5.3.2 *Phase Doppler Interferometry (PDI)*

5.3.2.1 Principle

Phase Doppler Interferometry (PDI) has evolved as a pioneering technology for quantitative spray measurement. PDI works on the principle of light scattered from two intersecting, coherent laser beams, which is similar to Laser-Doppler velocimetry (LDV). Sinusoidal doppler burst signals are generated by the sensor. Frequency of these signals is proportional to droplet velocity, and phase corresponds to the droplet diameter. PDI is capable of measuring droplet size distribution, velocity, and volume flux at a high rate of 10000 samples per second (Bachalo 2000; Tropea 2011). In this method, when a droplet passes through intersection of the laser beam (also called probe volume), reflection and refraction of beams occur. Disturbance created by the droplet at interference fringes of the intersecting coherent beams is received at receiver. Light intensity pattern at receiver is transferred to multiplier tubes, which in turns generates Doppler burst signals. Frequency of signal can be related to the velocity as (Patel et al. 2016),

$$V = f_d \delta \tag{5.5}$$

f_d Doppler frequency
δ Fringed spacing

The droplet diameter is determined by the following relationship

$$d = \frac{F \delta r}{s \Delta} \tag{5.6}$$

F Volume flux,
δr Fringe width,
s Slope factor,
Δ Spatial wavelength

A spatial wavelength is determined using phase shift of the signal between detectors in the time domain along with calibrated spacing of detectors.

Advanced Signal Analyser (ASA) further improves the signal. ASA amplifies Doppler burst signal generated by the receiver. It also performs necessary signal filtration before passing them to computer via a high-speed interface card.

A typical PDI experimental setup consists of two transmitters and a receiver. Both transmitters are placed at an angle of 60° to each other. Transmitter-1 generates two laser beams of green (wavelength 532 nm) and blue color (wavelength 491 nm). Yellow beam (wavelength 561 nm) emerges from transmitter-2. Beam splitter splits each beam into two parts. Laser beam alignment is done in such a way that all six beams intersect at a single point. Perfect alignment is ensured when interference

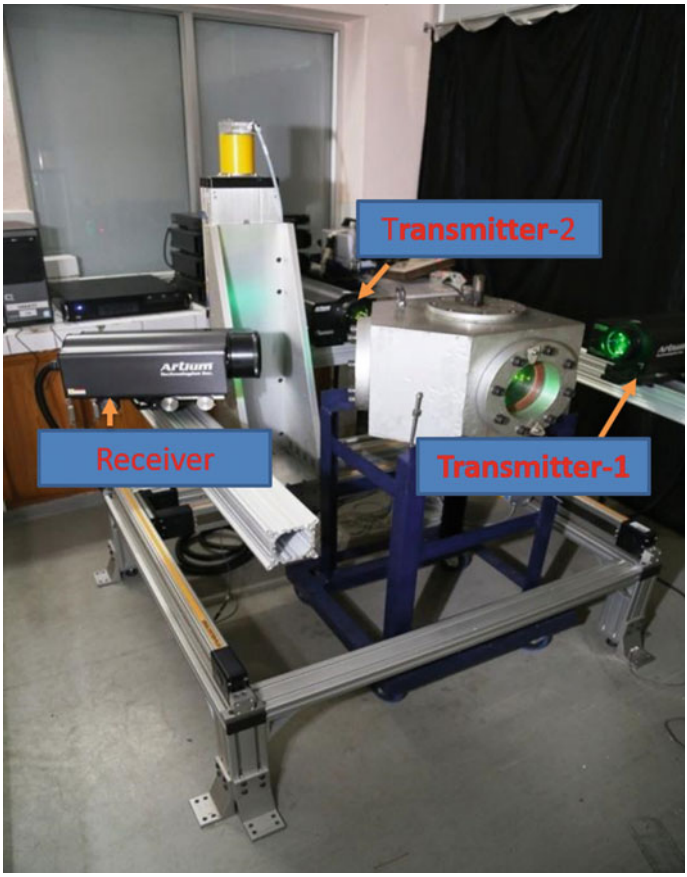

Fig. 5.5 A typical PDI setup

fringes can be clearly observed. A dedicated PDI software is used to produce real-time droplet size distribution and droplet velocity distribution of the spray under study.

5.3.2.2 Post Impingement Study Near Wall Region

PDI can be effectively used to study microscopic behavior of near wall impingement region. With the knowledge of droplet velocity and diameter, Weber number can be calculated, which gives valuable insight of the spray. Pan et al. (2019) have investigated the glide, spread, and splash phenomenon of impinging droplet using PDI along with other techniques such as PIV and Mie scattering. In this study, Weber number was calculated using the data acquired through PDI and Bai, and Gosman impingement map was used to study splash, stick, and glide behavior. Kay et al.

(2012) have studied pre and post impingement behavior using PDI technique. hollow cone spray was investigated. Figure 5.6 shows the raw data acquired in this study. A delay in data aquisation can be observed after Start of Injection (SOI). This was consistent with the injection rate shape used. The initial cluster of data corresponds to pre-spray. After that the hollow cone develops and then collapse towards the end of injection. In between the pre-spray and collapse no data has been recorded as the probe volume falls in the hollow region of the spray cone. This type of distribution is typical to hollow cone spray. Both, axial and radial velocity approaches to zero as the cone collapse and end of injection is approached.

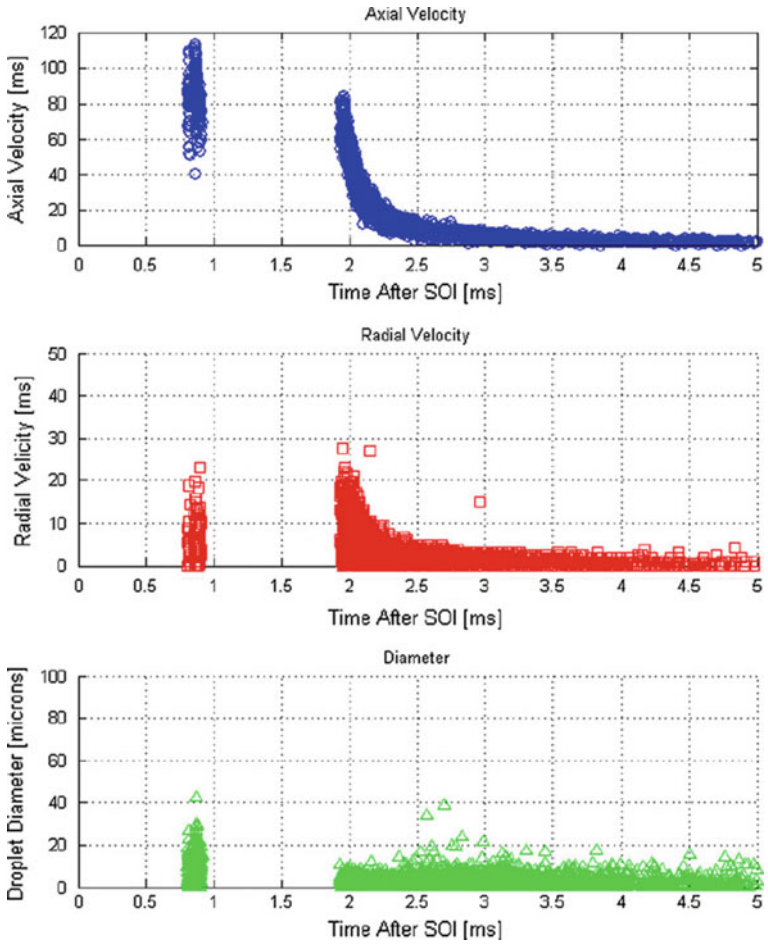

Fig. 5.6 Raw data recorded 10 mm downstream of the injector axis Kay et al. (2012)

5.4 Modeling of Spray Wall Impingement

For better design and optimization of low-emission modern diesel engines, the complicated process of spray-wall interaction needs to be understood in depth. Despite significant advancements in experimental diagnostics, in-cylinder investigation on engines in operation is still a difficult task. Fortunately, advanced computer modeling, can potentially predict in-cylinder dynamics. However, it requires the development of reliable impingement model. Many efforts have been made to develop reliable models over the years. Naber and Reitz's model is based on three breakup regimes, namely stick, reflect, and slide. Droplets with very low incident Weber number (We_{in}) will stick to the wall and continues to evaporate post impingement. Droplet with We_{in} in intermediate range will bounce off the wall. These droplets would retain their tangential components of velocity, but the normal components change its direction. For We_{in} greater than 80, droplets slide on the wall forming wall jet. Bai and Gosman model distinguishes between the dry and wet wall. The authors have provided a map of impingement regimes based on wall temperature. W_{in} was used as a standard to predict the outcome of droplet-wall interaction. For dry case stick, spread and splash regimes are modeled. For a wet wall, rebound is also included in addition to other modes mentioned. In Mundo, Tropea and Summerfield model only splash and deposition are considered. The two phenomena are different from a splashing parameter, which is a function of droplets Weber number and Reynolds number. O'Rourke and Amsden model calculates a splashing Mach number, which is a function of W_e, film thickness, and boundary layer thickness. For dry wall, film thickness becomes zero, and the model is similar to splash model. There are many modified and improved models which have been proposed. O'rourke model has better accuracy in predicting the wall droplets accuracy over the other models discussed. Hence this model is suggested for the modeling and simulation of droplets interaction in in-cylinder condition of ICE.

5.5 Summary and Future Scope

Spray-wall interaction study has been the prime area of researchers in the field of combustion for the last two decades. However, the recent developments in high-speed data acquisition, computing, and imaging have provided a new dimension to this study. With the introduction of laser technology like PDI, both qualitative and quantitative analysis is possible with better accuracy. On the other hand, the age-old technologies like shadowgraphy and Schlieren imaging are much simpler and less expensive. But at the same time, the experimental setup requires experience and expertise.

In preceding sections, we focussed mainly on the two optical techniques which can be used to study the spray-wall interaction. In order to study the effects of fuel spray on combustion and emissions, none of the technique discussed above can

solely characterize the spray behavior completely. Schlieren technology is a simple and useful tool to study the morphology of spray, especially in vapor phase. While PDI is capable of measuring both velocity and droplet diameter but it's a single point measurement system. PDI technique directly provides spray droplet and velocity distribution and probably the simplest technique to handle once alignment is done properly. Hence, use of the combination of these methods can capture complete physics of the problem.

The literature is enriched with a lot of information regarding the impingement of spray. However,these informations and understandings are yet to be utilised for practical purpose. With the help of these fundamental studies, optimised injection strategies can be developed. Previous research investigations are mostly done inside the Constant Volume Combustion Chamber (CVCC) in a quiescent environment. Efforts have been made to replicate engine like environment, but the effect of turbulent environment is hardly studied. The optical engine can be a breakthrough technology to solve this problem. Optical access into the cylinder of anengine in operation provides the scope of using non-intrusive techniques like PDI to study the spray/flame interaction of the wall in transient condition. For an optical diesel engine, inert gases like nitrogen or exhaust gases from external combustor can be used to study the spray interaction and film formation in in-cylinder environment. It would help developing much clearer insight of the phenomenon. Appropriate numerical model can be helpful in this regard but its development remains a challenge. Fundamental study of the film dynamics is another area that needs to be explored for complete understanding. Effect of geometry of the impingement surface on film stability should be studied. The geometrical parameters like impingement angle, spray radius can be optimised to minimise the film formation. This will help to develop an efficient piston bowl geometry for lower emissions. Further optimization of the geometry can be done by the experimental diagnosis techniques. With the development of new low-temperature combustion strategies like HCCI, PCCI, the spray-cylinder liner interaction has become an important issue. This significantly changes physics of the problem due to the presence of lube oil film on liner. Very few studies have been found in the literature dealing with this issue. Future studies can therefore focus on this area as well.

References

Abo-Serie E, Gavaises M, Arcoumanis C (2003) Spray/wall interaction in direct-injection spark ignition engines equipped with multi-hole injectors. In: Proceedings 9th international conference on liquid atomisation and spray systems (ICLASS). Sorrento, p 28

Babu MG, Murthy BS (1976) Simulation and evaluation of exhaust and intake system of a four-stroke spark ignition engine. SAE Technical Paper

Bachalo WD (2000) Spray diagnostics for the twenty-first century. At Sprays 10(3–5):439–474

Benajes J, García-Oliver JM, Novella R, Kolodziej C (2012) Increased particle emissions from early fuel injection timing Diesel low temperature combustion. Fuel 1(94):184–190

Berggren C, Magnusson T (2012) Reducing automotive emissions—The potentials of combustion engine technologies and the power of policy. Energy Policy 1(41):636–643
Borman G, Nishiwaki K (1987) Internal-combustion engine heat transfer. Prog Energy Combust Sci 13(1):1–46
Cardenas M, Pawlowski A, Günther M, Kneer R (2008) Spray-wall interaction of clustered sprays under conditions relevant for diesel engines. ILASSEuropeilasseurope.org
Du W, Zhang Q, Bao W, Lou J (2018) Effects of injection pressure on spray structure after wall impingement. Appl Therm Eng 25(129):1212–1218
Fang T, Chia-fon FL (2011) Low sooting combustion of narrow-angle wall-guided sprays in an HSDI diesel engine with retarded injection timings. Fuel 90(4):1449–1456
Hohenberg GF (1979) Advanced approaches for heat transfer calculations. SAE Technical paper
Ismael MA, Heikal MR, Baharom MB (2014) Spray-wall impingement of Diesel-CNG dual fuel jet using Schlieren imaging technique. In: MATEC web of conferences 2014, vol 13. EDP Sciences, p 02037
Jia M, Xie M, Stobart R (2009) Evaluation of spray/wall interaction models under the conditions related to diesel HCCI engines. SAE Int J Fuels Lubr 1(1):993–1008
Kay PJ, Bowen PJ, Gold MR, Sapsford SM (2012) Transient fuel spray impingement at atmospheric and elevated ambient conditions. Exp Fluids 53(4):873–890
Kitasei T, Yamada J, Shoji T, Shiino S, Mori K (2008) Influence of the different fuel spray wall impingement angles on smoke emission in a DI-diesel engine. SAE Technical Paper
Kook S, Park S, Bae C (2007) Influence of early fuel injection timings on premixing and combustion in a diesel engine. Energy Fuels 22(1):331–337
Mahmud R, Kurisu T, Nishida K, Ogata Y, Kanzaki J, Tadokoro T (2018) Experimental study on flat-wall impinging spray flame and its heat flux on wall under diesel engine–like condition: first report—effect of impingement distance. Proc Inst Mech Eng Part D: J Autom Eng 33(8):2187–2202
Mathews WS, Lee CF, Peters JE (2013) Experimental investigations of spray/wall impingement. At Sprays 13(2 and 3)
Meingast U, Staudt M, Reichelt L, Renz U, Sommerhoff FA (2000) Analysis of spray/wall interaction under diesel engine conditions. SAE Trans 1:299–312
Musculus MP, Miles PC, Pickett LM (2013) Conceptual models for partially premixed low-temperature diesel combustion. Prog Energy Combust Sci 39(2–3):246–283
Mwangi JK, Lee WJ, Chang YC, Chen CY, Wang LC (2015) An overview: Energy saving and pollution reduction by using green fuel blends in diesel engines. Appl Energy 1(159):214–236
Nayak SK, Mishra PC, Parashar SK (2016) Influence of spray characteristics on heat flux in dual phase spray impingement cooling of hot surface. Alex Eng J 55(3):1995–2004
Nhumaio GC, Watkins AP (2005) Simulation of electrosprays in model direct-injection spark-ignition engine in-cylinder flows. Int J Engine Res 6(6):527–546
Pan H, Xiao D, Hung D, Xu M, Li X (2019) Experimental investigations of wall jet droplet impact on spray impingement fuel film formation. Fuel 1(241):33–41
Park SW, Lee CS (2004) Macroscopic and microscopic characteristics of a fuel spray impinged on the wall. Exp Fluids 37(5):745–762
Pastor JV, Payri R, Garcia-Oliver JM, Nerva JG (2012) Schlieren measurements of the ECN-spray a penetration under inert and reacting conditions. SAE Technical Paper
Patel C, Sharma N, Tiwari N, Agarwal AK (2016) Effects of spray droplet size and velocity distributions on emissions from a single cylinder biofuel engine. SAE Technical Paper
Payri R, Gimeno J, Bracho G, Vaquerizo D (2016a) Study of liquid and vapor phase behavior on Diesel sprays for heavy duty engine nozzles. Appl Therm Eng 25(107):365–378
Payri R, Salvador FJ, Manin J, Viera A (2016b) Diesel ignition delay and lift-off length through different methodologies using a multi-hole injector. Appl Energy 15(162):541–550
Payri R, Viera JP, Pei Y, Som S (2015) Experimental and numerical study of lift-off length and ignition delay of a two-component diesel surrogate. Fuel 15(158):957–967

Peng Z, Liu B, Wang W, Lu L (2011) CFD investigation into diesel PCCI combustion with optimized fuel injection. Energies 4(3):517–531
Schulz F, Schmidt J, Kufferath A, Samenfink W (2011) Gasoline wall films and spray/wall interaction analyzed by infrared thermography. SAE Int J Engines 7(3):1165–1177
Seel K, Reddemann MA, Kneer R (2018) Optical investigation of the interaction of an automotive spray and thin films by utilization of a high-pressure spin coater. Exp Fluids 59(3):50
Seel K, Reddemann MA, Baltaci T, Kneer R (2015) Impact of lubricating oil films on spray-wall interaction. SAE Technical Paper
Serras-Pereira J, Aleiferis PG, Walmsley HL, Davies TJ, Cracknell RF (2013) Heat flux characteristics of spray wall impingement with ethanol, butanol, iso-octane, gasoline and E10 fuels. Int J Heat Fluid Flow 1(44):662–683
Stanton DW, Lippert AM, Reitz RD, Rutland CJ (1998) Influence of spray-wall interaction and fuel films on cold starting in direct injection diesel engines. SAE Trans 1:1540–1563
Su K (1999) Numerical studies of sprays impacting normally on an infinite plate. At Sprays 9(4)
Tang Q, Liu H, Li M, Yao M (2017) Optical study of spray-wall impingement impact on early-injection gasoline partially premixed combustion at low engine load. Appl Energy 1(185):708–719
Tropea C (2011) Optical particle characterization in flows. Ann Rev Fluid Mech 21(43):399–426
Tschöke H, Marohn R (eds) (2017) 10. Tagung Diesel-und Benzindirekteinspritzung 2016: InklusiveGaseinblasung. Springer, Berlin
Wang X, Huang Z, Zhang W, Kuti OA, Nishida K (2011) Effects of ultra-high injection pressure and micro-hole nozzle on flame structure and soot formation of impinging diesel spray. Appl Energy 88(5):1620–1628
Werlberger P, Cartellieri WP (1987) Fuel injection and combustion phenomena in a high speed DI diesel engine observed by means of endoscopic high speed photography. SAE Technical Paper
Woschni G (1967) A universally applicable equation for the instantaneous heat transfer coefficient in the internal combustion engine. SAE Technical paper
Yao M, Zheng Z, Liu H (2009) Progress and recent trends in homogeneous charge compression ignition (HCCI) engines. Prog Energy Combust Sci 35(5):398–437
Yu H, Guo Y, Li D, Liang X, Shu GQ, Wang Y, Wang X, Dong L (2015) Numerical investigation of the effect of spray cone angle on mixture formation and CO/Soot emissions in an early injection HCCI diesel engine. SAE Technical Paper
Zama Y, Sugawara K, Akop MZ, Furuhata T, Arai M (2014) Experimental study on velocity distribution of postimpingement diesel spray on a wall. Part 1: effect of impingement angle on flow pattern. At Sprays 24(8)

Chapter 6
Investigation of Influence of Injection Pressure on Gasoline Fuel Spray Characteristics Using Numerical Simulation

Sandip Wadekar

Abstract Maximum fuel injection pressure in gasoline direct injection engine is expected to increase because of its potential to reduce emissions while maintaining a high efficiency in spark ignition engine. Present gasoline injectors in the market operates in the range of 20–30 MPa. Because of many positive effects of high injection pressure for the emission reduction and fuel efficiency, an interest has been developed to investigate the spray behavior at around 40 MPa, 60 MPa and even more higher injection pressure. A fundamental investigation of spray characteristics at high-pressure injection will help to develop the understanding of spray behavior at such elevated pressure. In the present study, a gasoline fuel spray was studied through the numerical model at an injection pressure ranging from 40 to 150 MPa. A numerical simulation was performed in an optical accessible constant volume chamber. The chamber was effectively non-reacting and non-vaporizing condition since the focus was on the spray droplets. In the numerical model, gas flow was calculated by large-eddy simulation (LES) method and the liquid phase was accounted by a standard Lagrangian spray model. The fuel spray atomization was modelled using the Kelvin Helmholtz—Rayleigh Taylor (KH-RT) model, and droplet size distribution followed the Rosin-Rammler distribution function. Simulation results were validated by comparing the liquid penetration length of spray with the experimental data at different fuel injection pressures. Then, the mean droplet sizes such as arithmetic mean diameter and Sauter mean diameter of the spray droplets were compared with the measure droplet sizes as a function of pressure. The spray droplet size distribution was also shown along with measured droplet sizes. The result shows that the liquid length penetration of the spray was significantly increases together with the higher probability of smaller droplet by increasing the fuel injection pressure. Moreover, the mean droplet sizes were also reducing by increasing the fuel injection pressure, such as the droplet SMD was reduced from 13.5 to 7.5 μm by injecting the fuel at pressure 150 MPa instead of 40 MPa.

S. Wadekar (✉)
Chalmers University of Technology, Gothenburg, Sweden
e-mail: sandip.wadekar@chalmers.se

A. P. Singh et al. (eds.), *Simulations and Optical Diagnostics for Internal Combustion Engines*, Energy, Environment, and Sustainability,
https://doi.org/10.1007/978-981-15-0335-1_6

Keywords Gasoline high pressure injection · Large-eddy simulation · Spray modelling

6.1 Introduction

Emission regulation agencies have strongly influenced the engine development over the last decades, encouraging to develop cleaner combustion engine technology. In the recent year, strict emission norms for CO2 and particulate number (PN) discharge from the vehicles have been initiated, and more tougher emission control is expected in near future. To fulfil these emission regulations, vehicle manufacturers are exploring several strategies including electrified automotive powertrain. But currently, the capacity and working lifespan of electric battery is very limited. The intermediate solution could be a hybrid vehicle, where electric battery and internal combustion engine can be utilized together. That means, researcher still need to focus on spark ignition (SI) engine development.

In SI engine, the research is mainly focused on the Gasoline Direct Injection (GDI) engine because of its capability to improve the fuel consumption and exhaust emission. In GDI engine, gasoline fuel spray emerged from the injector plays a crucial role in fuel-air mixing formation, combustion process and subsequently on the exhaust emissions. Therefore, present injector system needs to improve to produce better spray characteristics. The spray characteristics such as penetration length, droplet sizes, and droplet distribution helps to enhance a combustion system efficiency. Therefore, it is important to investigate the spray characteristics qualitatively and quantitatively using measurement and simulation tool to develop an efficient combustion system.

An effective way to improve the spray characteristics is to increase the fuel injection pressure. For this reason, fuel injection pressure of injector system has been increased since the introduction of GDI technique. In the beginning, fuel injector operated at injection of 5–10 MPa only. The fuel spray at such pressures are very sensitive to operating and thermodynamics conditions. Then, after the introduction of turbo-charger, fuel injection pressure was further increased to get an extended injector flow range (Piock et al. 2002). The second drive to increase injection pressure was the requirement of better atomization and improved mixture formation (Waltner et al. 2006). In this way, maximum fuel injection pressure over the last decade has been increased up to 25 MPa. And, it is expected that the gasoline injection pressure will increase up to 40 MPa by 2020 and, 60 MPa by 2025.

Relatively few investigations (Mitroglou et al. 2007; Matousek et al. 2013; Buri et al. 2010) have been performed by experiments or simulation technique concerning the influence of high-pressure fuel injection. Tian et al. (2016) studied the influence of high injection pressure on the spray characteristics under vaporizing and non-vaporizing conditions. They concluded that the spray penetration length was proportional to time, and significantly increased by increasing injection pressure for both vaporizing and non-vaporizing conditions. Kim et al. (2013) compared fuel

spray cone angle and penetration length for gasoline and diesel fuel at injection pressures between 40 and 100 MPa. The result shown that the diesel fuel has a longer liquid penetration length and a shorter spray cone angle compared to gasoline fuel. Similar study of comparing diesel and gasoline fuel spray at injection pressure 60–150 MPa was performed by Payri et al. (2012). Moreover, a gasoline spray at pressure 30–150 MPa under different chamber pressure was studied using high-speed image technique by Medina et al. (2018). The result revealed that the spray characteristics (penetration length, spray cone angle and other) have a strong impact of chamber pressure compared to the injection pressure.

As a summary of literature study, some research gap has been identified. Previous studies have mainly been focused on macroscopic spray characteristics for example spray cone-angle, spray area, and spray tip penetration but rather limited investigations on details of the atomization characteristics were exercised. The efforts to analyze the spray characteristics at high injection pressure have been highly important but a detailed investigation is still needed. Moreover, diagnosis methods are confined by an optical accessible limit.

Due to the limitations of measurement techniques, use of computational fluid dynamics (CFD) approach is becoming more reliable and important tool for the in-depth study of fuel spray and its subsequent processes. In CFD method three techniques are widely used, that has their own strengths and weaknesses. First, the Reynolds averaged Navier-Stokes (RANS) method is widely used to simulate the fuel spray (Chrigui et al. 2004; Paredi et al. 2018; Wang et al. 2011). In this method, averaged (Reynolds) equations of Navier-stokes are solved, and offers a time average solution with economical computational cost. But, the averaging nature of the method restrict its use for global predictions only. Second, direct numerical simulation (DNS) method resolves all the scale involved in the flow but it is computationally very expensive and limits its use to the academic test cases only. Third, large-eddy simulation method resolves the large flow structure and model the sub-grid scale structure. The LES method extensively used for unsteady, multiphase phenomenon because this method can capture an intrinsic time and space dependent phenomenon with a reasonable computational cost (Apte et al. 2003; Allocca et al. 2018; Senecal et al. 2013; Pera et al. 2006). The capability of LES method for the engine application is highlighted in the review provided by Rutland (2011). In the present work, fuel spray was modelled using a Eulerian-Lagrangian approach. The fuel was represented as a discrete set of computational parcels and gas phase was accounted using the LES method. The atomization of spray parcels depend on the exchange of mass, momentum and energy with the gas phase, which was accounted using KH-RT model. Addition models were also provided for droplet breakup, droplet dispersion, transfer of momentum and kinetic energy.

The aim of present work is to study the gasoline fuel spray characteristics using numerical models at different injection pressures (40–150 MPa). Another objective is to evaluate the ability of models to capture the spray, and therefore, calculation results are compared with the measuremental data. The spray characteristics compared with the measurement are the spray liquid penetration length, droplet mean sizes and

distribution. The result suggested that the higher fuel injection pressure increases the spray penetration length and substantially reduces the droplet size.

6.2 Experimental Set-Up

The measurements were performed in a constant volume spray chamber with optical access. In the spray investigation, special designed 6-hole diesel-type nozzle was used, which had a relatively large L/D (nozzle thickness to smaller hole diameter) ratio to withstand the high injection pressure. The L/D ratio in the gasoline and diesel type injector is usually around 2–3 and 8–9, respectively. The current investigated nozzle is divergent towards exit side with exit hole diameter 380 μm, and L/D ratio is 5.45. A piezo-electric system was used for needle movement. This actuation system controls the needle movement using the pressure difference between the fuel injection and return flow pressure. The injection rate of the fuel was measured using an injection rate meter. The operating conditions for the measurements are summarized in Table 6.1.

After the injection rate measurement, a high-speed video (HSV) camera was utilized to capture the shadowgraph images of the liquid spray in an optical accessible chamber. The black illumination was used because it clear distinct between the liquid spray region and surrounding air. A schematic diagram of the experimental setup is shown in Fig. 6.1. The optical access into the spray chamber is provided through the quartz glass window of diameter 90 mm. The spray chamber contain air at atmospheric condition. For the shadowgraphy, a LED light was passed towards the spray, and high-speed camera captured the scattered light. The spray images were taken for 20 continues shots. The average image of 20 shots was used to postprocess and analyze the spray characteristics such as spray penetration length and spray jet-angle for all investigated injection pressures. First, a mask was applied to trim the spray jet and injector location was determined. Then, the distance between the nozzle and spray-tip was measured, keeping in mind the camera view angle, as a spray penetration length. Similar postprocessing technique was applied for spray jet angle calculation, which as used as boundary condition for the cfd simulations.

Table 6.1 Operating conditions of the measurements

Fuel	n-heptane
Chamber pressure (MPa)	0.1
Chamber temperature (K)	293
Nozzle outlet diameter (μm)	380
Injection mass (mg)	54
Injection duration (ms)	3
Fuel injection pressure (MPa)	40, 60, 80, 100, 120, 150

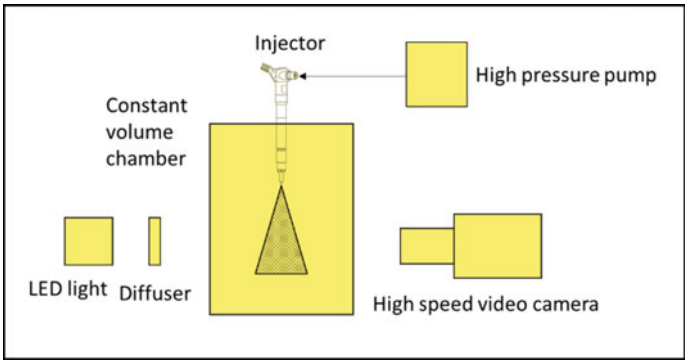

Fig. 6.1 Schematic diagram of the spray measurements using high-speed shadowgraph imaging

After spray imaging, a 2D Phase Doppler Interferometry was employed to measure the spray droplet sizes. In this technique, two intersecting laser beams built a measurement volume. The measurement location was set at 80 mm downstream of the injector tip and 5 mm outside the spray core. This location was chosen considering the high density at the center of the spray. The droplet was investigated for the injection event only. The pulse time, signal delay for needle opening and closing time was ignored.

6.3 Numerical Modeling

6.3.1 Fluid Motion

Spray phenomenon can be model using a multi-phase numerical model which can correctly describe a liquid phase, gas phase and an interactions between these two phases. In the present work a well-known Euler-Lagrangian approach was used to describe the spray occurrence. In this approach, gas phase was described by Euler method and liquid spray was modelled by lagrangian particle tracking (LPT) method. Both phases were coupled using the addition source terms in the Euler (gas phase) conservation equation. The Eulerian gas phase can be described using the equation of mass (6.1), momentum (6.2), and energy (6.3), as:

$$\frac{\partial \bar{\rho}}{\partial t} + \frac{\partial \left(\bar{\rho}\tilde{u}_j\right)}{\partial x_j} = s_{ev}, \tag{6.1}$$

$$\frac{\partial \bar{\rho}\tilde{u}_j}{\partial t} + \frac{\partial \left(\tilde{u}_i\tilde{u}_j\right)}{\partial x_j} = \frac{\partial \bar{\tau}_{ij}}{\partial x_j} + \frac{\partial \tau_{ij}^{sgs}}{\partial x_j} - \frac{\partial \bar{p}}{\partial x_i} + s_{i,m}, \tag{6.2}$$

$$\frac{\partial(\bar{\rho}\tilde{e})}{\partial t}+\frac{\partial\left(\bar{\rho}\tilde{e}\tilde{u}_j\right)}{\partial x_j}+\frac{\partial(\bar{\rho}K)}{\partial t}+\frac{\partial\left(\bar{\rho}K\tilde{u}_j\right)}{\partial x_j}=\frac{\partial}{\partial x_j}\left(\alpha_{eff}\frac{\partial T}{\partial x_j}\right)+\frac{\partial\left(\bar{p}\tilde{u}_j\right)}{\partial x_j}+s_e. \tag{6.3}$$

Here, the overline and tilde represents a Reynolds filtered and a Favre filtered quantity respectively, with relation $\tilde{q}=\overline{\rho q}/\bar{\rho}$. In the governing equations, $\bar{\rho}$ is the density, p is the pressure, $\tilde{u}_j$ is the flow velocity, $\bar{e}$ is the internal energy, K is the kinetic energy, τ_{ij} is the viscous shear stress and α_{eff} is the effective thermal diffusivity. In the mass conservation equation, the source term s_{ev} can be neglected as there is no evaporation was considered in the present work. Moreover, the momentum transfer and heat transfer between the liquid and gas phase was accounted using momentum and energy source term, respectively. The unclosed Reynold stress tenser τ^{sgs} was modelled using the standard Smagorinsky model (Smagorinsky 1963), as:

$$\tau_{ij}^{sgs}=-2\bar{\rho}\upsilon_T\left(\tilde{S}_{ij}-\frac{1}{3}\delta_{ij}\tilde{S}_{kk}\right), \tag{6.4}$$

$$\upsilon_T=C_s^2\Delta^2\sqrt{2\tilde{S}_{ij}\tilde{S}_{ij}}, \tag{6.5}$$

$$\tilde{S}_{ij}=\frac{1}{2}\left(\frac{\partial\tilde{u}_i}{\partial\tilde{x}_j}+\frac{\partial\tilde{u}_i}{\partial\tilde{x}_j}\right). \tag{6.6}$$

Here, $\boldsymbol{\delta_{ij}}$ is the Kronecker delta, $\boldsymbol{\upsilon_T}$ is the turbulent kinematic viscosity and $\boldsymbol{C_s}$ is the Smagorinsky constant. The grid filter width Δ was calculated using cubic root of the cell volume. The dynamic viscosity was calculated using the Sutherland law.

6.3.2 Droplet Motion

The liquid spray was defined using the Largangian particles as fuel droplets. In order to mimic the real spray large number of droplets needs to be considered, but solving the equation of motion for each fuel droplet was not affordable computationally. Therefore, the droplets having same properties were combined as 'parcel', which allowed to simulate the spray with reasonable computational cost. In the simulation, fuel droplet exchanged the momentum with the gas phase when the fuel was injected into quiescent gas environment at high velocities. The momentum exchange was estimated using a drag force (F_d) acting on a liquid parcel, as:

$$F_d=\frac{1}{6}\rho_p\pi d^3\frac{du_p}{dt}=\frac{1}{2}\left(u_g-u_p\right)\left|u_g-u_p\right|\rho_g C_d\frac{\pi d^2}{4}, \tag{6.7}$$

where d, ρ_g, ρ_p, u_g, and u_p is the droplet diameter, density of gas, density of fuel particle, velocity of gas and particle velocity, respectively. The coefficient of drag

force (C_d) acting on a droplet defined as:

$$C_d = \frac{24}{Re_p}\left(1 + \frac{1}{6}Re_p^{2/3}\right) \text{ for } Re_p < 1000, \tag{6.8}$$

$$C_d = 0.424 \; for \; Re_p \geq 1000. \tag{6.9}$$

The particle Reynolds number was calculated using the viscosity of the gas (υ_g), as:

$$Re_p = \frac{|u_g - u_p|d}{\upsilon_g}. \tag{6.10}$$

6.3.3 Droplet Break-up Model

The fuel droplets were injected using the Blob-injection model (Reitz 1987). During the injection, the liquid droplets (blobs) were continuously introduced with a diameter equal to the injector orifice diameter. The number of droplets injected per time-step was determined from the mass flow rate profile taken from the injector rate meter. It was assumed that no cavitation was generated when the liquid fuel flow through the injector orifice. The initial big spherical droplets were then broke down into the smaller droplets with a process called secondary break-up.

In the present work, secondary break-up of droplets was accounted using a Kevin-Helmholtz Rayleigh-Taylor (KHRT) model described by Reitz (1999). The KH-RT model was chosen as it is suitable for high Weber number sprays. This model combines the Kelvin-Helmholtz (KH) and Rayleigh-Taylor (RT) instability to calculate the diameter of new child droplet from the parent droplet. In KH instability, the break-up was estimated by the wavelength of instability generated by the aero-dynamics forces. Whereas, in RT break-up, wavelength of instability due to liquid-gas interaction through the density difference between liquid fuel and gas was used to calculate the break-up. In the simulation, the droplet break-up was finally considered using a mechanism (either KH or RT) which predicts the shortest break-up time. The KH instability was dominated around the nozzle exit and RT instability was dominant in downstream part of spray. Further detail of the model can be found in Reitz (1999).

6.4 Computational Set-Up

Computational mesh: A spray simulation needs a high-quality mesh to obtain an accurate numerical solution. The quality of spray in the numerical solution is highly

depend on the mesh resolution. Moreover, numerical instability and mesh causing errors can also be reduced by employing a good quality mesh. A study of impact of gird resolution on the spray formation provided by Banerjee and Rutland (2012) used to identify the correct mesh resolution for this work. The computational mesh was created using the OpenFoam's mesh utility called '*blockMesh*'. The dimension of spray chamber is 180 mm diameter and 120 mm height. The mesh contains almost equidistance hexahedral cells with the resolution of 0.5 mm. However, because of circular shape of the spray chamber the grids were stretched towards the chamber surface and subsequently mesh resolution increased maximum up to 1 mm. The whole mesh contains more than 24 million cells which restrict to further refinement of the mesh gird. The 3D view and top view of the spray chamber is shown in Fig. 6.2. Moreover, the fuel was injected from the top of spray chamber consisting 6 symmetrical spray jet. The total mass of liquid fuel (54 mg) was injected through 4e7 parcels, which was identical for all the investigated injection pressures.

Numerical set-up: The numerical simulation was performed in an open accessible library known as OpenFoam-2.2.x (The open source CFD 2014). All the simulation cases were non-reactive and non-evaporative. The spray chamber was filled with the air at atmospheric condition (T = 293 K and p = 0.1 MPa). The liquid fuel (n-heptane) was injected into the spray chamber at different injection pressure. Total mass injected and mass flow rate profile was provided as an input to the simulation, which was measured using flow rate meter. Moreover, the number of parcels per second of injection was 4e7 and constant coefficient of discharge 0.9 was provided. The spray-jet angle was defined as constant 8.8° throughout the injection event. The numerical equation was solved using an implicit backward (second-order accurate) scheme for time integration and central differencing scheme (second order accurate) for the treatment of convective scalar fluxes. For all scalar quantities zero-gradient boundary condition was applied at walls.

Furthermore, in the simulation all 6 spray-jet were considered to mimic the multi-hole injection event. The primary break-up of spray was accounted by Blob model with the Rosin-Rammler distribution function (Rosin and Rammler 1933) for the initial droplet sizes. The initial diameter of blobs was provided corresponding to the

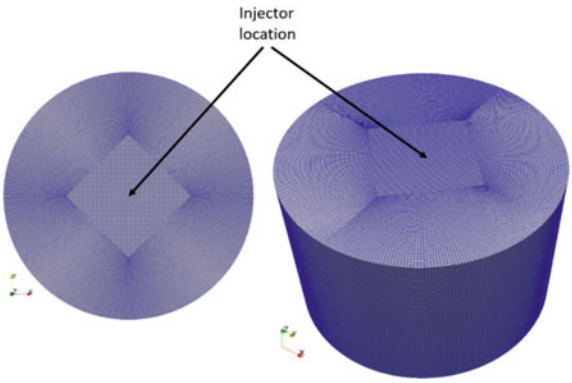

Fig. 6.2 (Left) top view, (right) 3d view of spray chamber with pointing the injector location

Table 6.2 Sub-models and their model constant used in the simulation (Wadekar et al. 2019)

Type	Model	Constants
Injector	Multi hole injector	6 holes, Do = 380 μm
Droplet distribution	Rosin-Rammler	n = 3
Primary break-up	Uniform droplet size	380 μm
Secondary break-up	KH-RT	B1 = 0.61, B2 = 40, C1 = 1, C2 = 0.1
Dispersion model	Stochastic dispersion	

nozzle exit hole diameter (380 μm). These primary blobs were undergone through the secondary breakup modelled using Kelvin-Helmholtz Rayleigh-Taylor (KHRT) model. Also, the turbulent fluctuations in droplet trajectories were modelled by stochastic dispersion model. The different numerical models and their model constant are illustrated in the Table 6.2.

6.5 Result and Discussion

Figure 6.3 presents the spray penetration length as a function of time together with the measured spray penetration length at different fuel injection pressures. In this work, the spray penetration length was defined as the distance between the farthest point of spray-tip and the nozzle position along the spray direction. The measured data presented here were the average of 20 injection shots. The measured data was determined using a post-processing technique based on pixel-based threshold filter. The variation between shot-to-shot is also provided using shaded color band together with average data. The spray model was tuned in such a way to ensure the correct calculation of the measured penetration length. The model was tuned only for a single case i.e. 100 MPa, else cases followed the same tuned values. For all injection pressure cases, different mass flow profile was provided which was obtained from the measurement.

The simulation result of spray penetration length is in fair agreement with the measured penetration length for all injection pressure cases. The better agreement of penetration length indicate that it correctly mimics the momentum exchange between liquid fuel and surrounding gas during the injection process. It also exhibits that the aerodynamic force induced during fuel injection is correctly predicted by the model. The spray penetration results suggested that by increasing the injection pressure penetration length increases and injection time significantly reduces.

Figure 6.4 illustrates the computed and measured Sauter mean diameter (SMD or D32) as function of time at different fuel injection pressures. Generally, the D32 diameter is highly affected by the presence of larger droplet. The large droplets usually come from the movement of needle inside the injector. Therefore, the measurement data of droplet diameters presented here are extracted during the full-lift needle

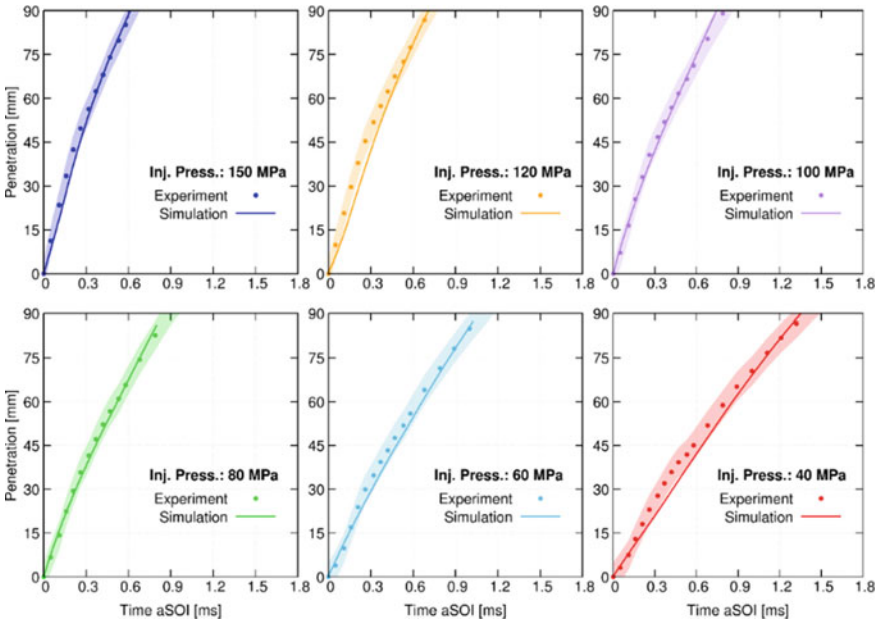

Fig. 6.3 The comparison between measured (dot) and calculated (solid line) spray penetration length at different injection pressures. The filled area shows the standard deviation of measurement data

state. That mean, the influence of larger droplets is eliminated from the measurement data, and hence, SMD diameter seem to be constant over the time. Moreover, as the simulation utilized the lagrangian model, no needle movement was considered. The results indicated that the higher fuel injection pressure significantly reduced the SMD diameter. Which mean the higher fuel injection pressure help in reducing the droplet diameter and subsequently provide the large surface of the fuel droplet to assist a faster evaporation under engine conditions.

The calculated result shown the fair agreement with the measured SMD data at all injection pressure. However, the injection pressure case of 40 and 150 MPa shows slight discrepancies. The potential cause could be the influence of large droplets that might have come during the full-needle opening position. Usually, the bigger droplets stayed in the spray axis because of their momentum, whereas smaller droplets generated after the breakup were more distributed around the peripheral area of the spray. Moreover, the SMD valve during the initial time in the calculation shown the higher values of SMD diameter. It might be the influence of poor primary atomization model, in which the initial droplet was considered to be equal to the nozzle orifice diameter.

Figure 6.5 presents the comparison of calculated mean droplet diameter against the measured mean droplet diameter at different fuel injection pressure. The mean droplet shown are arithmetic mean diameter (D10) and Sauter mean diameter (D32),

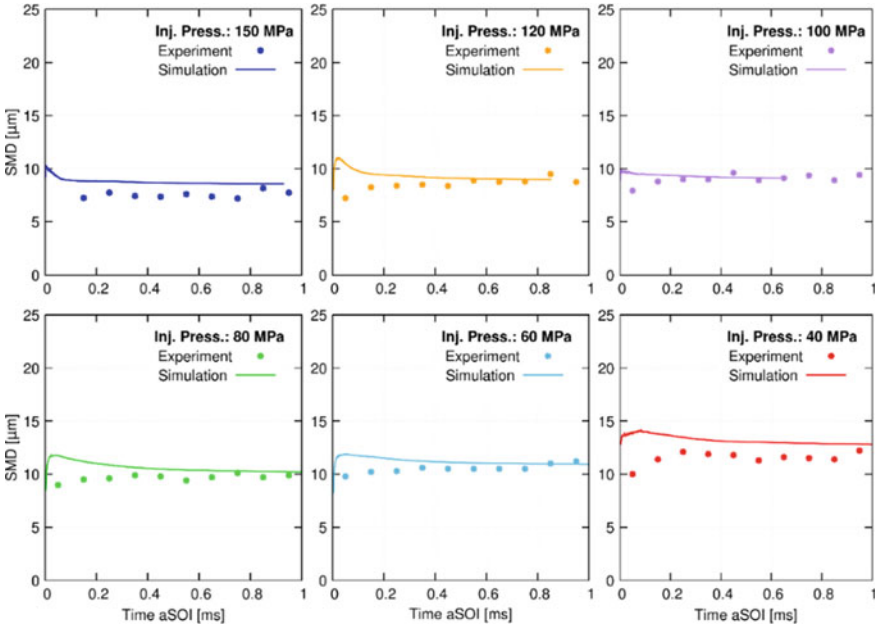

Fig. 6.4 The comparison between experimental and simulated Sauter mean diameter (SMD or D32) as a function of time at different fuel injection pressures

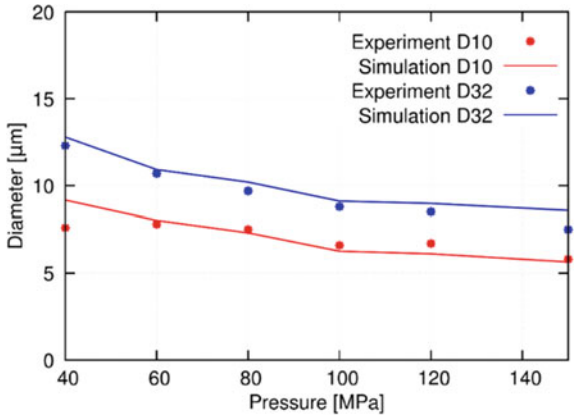

Fig. 6.5 Illustration of arithmetic mean diameter (D10) and Sauter mean diameter (D32) as a function of injection pressure for the simulation (line) and measurement data (dot) (Wadekar et al. 2019)

which are probed at around 80 mm downstream from the nozzle location. The result of droplet mean diameter shown the good agreement with the measured mean diameters at all injection pressure cases. The result clearly evident that droplet diameter reduced by increasing the injection pressure. The D10 diameter shown slight variation by increasing the injection pressure, in comparison with the D32 diameter. Possibly the droplet diameters have achieved the adequately small diameter and do not exhibit the further breakup. However, the D32 valve was significantly reduce by exerting the high injection pressure. Which mean the influence of larger droplets that came from needle opening and closing event, was significantly reduce and helped in faster evaporation.

In addition to droplet mean diameter, the droplet size distribution also play significant role in the droplet atomization process and subsequently fuel-air mixture formation. Figure 6.6 illustrate the comparison between calculated local droplet size distribution against the measured data. The droplet size distribution data also collected at 80 mm downstream of injector nozzle. Moreover, the droplet size distribution data was collected during the full needle opening condition just to avoid the influence of larger droplet from the opening/closing needle position. In the simulation, the same location with the diameter of around 2 mm diameter was considered to collect the droplet distribution. The simulation result shown overall good agreement with the measured droplet distribution valves at all injection pressure.

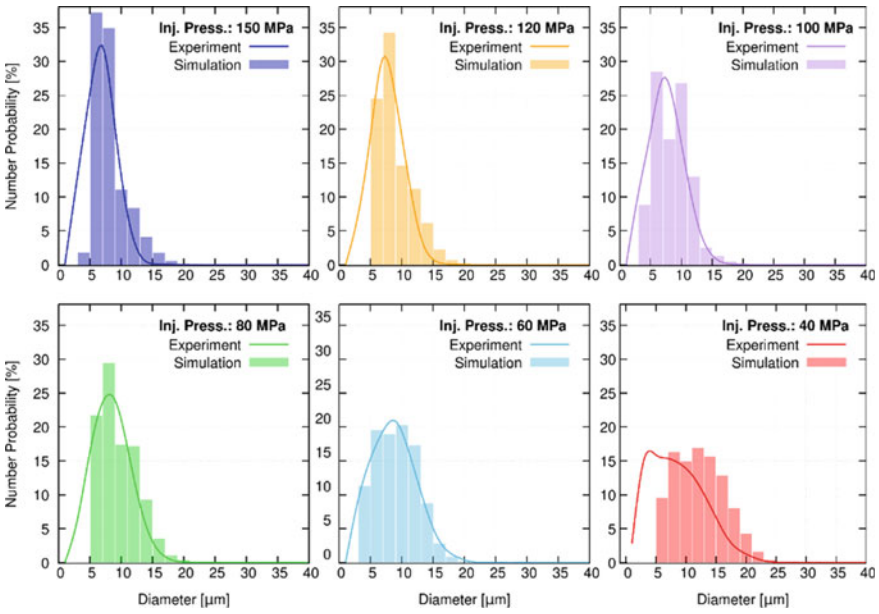

Fig. 6.6 The local droplet size distribution is demonstrated at different injection pressure for simulation and experimental data

The droplet size distribution at high pressures (120 and 150 MPa) demonstrate the higher probability of smaller droplets. At these pressures, 5 to 10 μm diameter shown more than 30% probability, while the probability of large droplets (i.e. above 15 μm) were negligible (< 5%). Also, the droplet distribution curve at this injection pressure looked quite narrow with the highest probability of smaller droplet amongst all the injection pressure studied here. Moreover, at injection pressure 80 and 100 MPa, the droplet size distribution still shown the higher probability of smaller droplets, but the big droplets were also indicated. Then, at 40 and 60 MPa injection pressure, the chance of finding the smaller droplets was significantly reduced and pointing out the sufficiently number of large droplet diameter valves. The size distribution curve looked more wider compared to the distribution at highest pressure.

Note that, the droplet size distribution above 100 MPa looks almost similar. The potential reason was the injection pressure at around 100 MPa was the threshold or saturation pressure. The injection above this threshold pressure was not anymore efficient to reduce the droplet size and effectively distributed within the spray jet.

6.6 Conclusion

The purpose of the present work was to study the gasoline fuel spray at very high injection pressures i.e. 40–150 MPa. Mainly the fuel spray characteristics were analyzed such as spray penetration length, droplet mean diameters and droplet size distribution. Another objective was to check the accuracy of numerical model to capture the spray related phenomenon correctly. The following conclusion were down based on the simulation results:

- The numerical model correctly captured the spray penetration length for all injection pressures. It suggested that the higher injection result in significant enhance in penetration length.
- The numerical model appropriately calculated the Sauter mean diameter (D32) of the fuel droplet when compared to the experimental results. At higher injection pressure the SMD values are significantly reduces compared to D10 diameter. It suggested that the influence of large droplet (comes from the needle movement) was substantially reduced by injecting the fuel at higher injection pressure.
- The Arithmetic mean diameter decreased from 9.2 to 6 μm, when injection pressure increased from 40 to 150 MPa. It concluded that the high injection help in faster droplet break-up and subsequently promote the faster evaporation of liquid fuel.
- The local droplet size distribution of spray jet was considerably good predicted by the model and substantiate that the droplet size was reduced using higher pressure injection. At 150 MPa injection pressure, the probability of finding the smaller droplets (5–10 μm) was highest amongst the investigated pressures.

References

Allocca L, Bartolucci L, Cordiner S, Lazzaro M et al (2018) ECN spray G injector: assessment of numerical modeling accuracy. SAE technical paper 2018-01-0306. https://doi.org/10.4271/2018-01-0306

Apte SV, Gorokhovski M, Moin C (2003) LES of atomizing spray with stochastic modeling of secondary breakup. Int J Multiph Flow 29(9). https://doi.org/10.1016/s0301-9322(03)00111-3

Banerjee S, Rutland C (2012) On LES grid criteria for spray induced turbulence. SAE technical paper 2012-01-0141. https://doi.org/10.4271/2012-01-0141

Buri S, Kubach H, Spicher U (2010) Effects of increased injection pressures of up to 1000 Bar-opportunities in stratified operation in a direct-injection spark-ignition engine. Int J Engine Res. https://doi.org/10.1243/14680874JER608

Chrigui M, Sadiki A, Ahmadi G (2004) Study of interaction in spray between evaporating droplets and turbulence using second order turbulence RANS modelling and a lagrangian approach. Prog Comput Fluid Dyn. https://doi.org/10.1504/PCFD.2004.004084

Kim K, Kim D, Jung Y, Bae C (2013) Spray and combustion characteristics of gasoline and diesel in a direct injection compression ignition engine. Fuel. https://doi.org/10.1016/j.fuel.2013.02.060

Matousek T, Dageforde H, Bertsch M (2013) Influence of injection pressures up to 300 Bar on particle emissions in a GDI engine. In: 17th ETH conference on combustion generated nanoparticles

Medina M, Fatouraie M, Wooldridge M (2018) High-speed imaging studies of gasoline fuel sprays at fuel injection pressures from 300 to 1500 Bar. SAE technical paper 2018-01-0294. https://doi.org/10.4271/2018-01-0294

Mitroglou N, Nouri J, Yan Y, Gavaises M et al (2007) Spray structure generated by multi-hole injectors for gasoline direct-injection engines. SAE technical paper 2007-01-1417. https://doi.org/10.4271/2007-01-1417

Paredi D, Lucchini T, D'Errico G, Onorati A (2018) Combined experimental and numerical investigation of the ECN spray G under different engine-like conditions. SAE technical paper 2018-01-0281. https://doi.org/10.4271/2018-01-0281

Payri R, García A, Domenech V, Durrett R et al (2012) An experimental study of gasoline effects on injection rate, momentum flux and spray characteristics using a common rail diesel injection system. Fuel. https://doi.org/10.1016/j.fuel.2011.11.065

Pera C, Réveillon J, Vervisch L, Domingo P (2006) Modeling subgrid scale mixture fraction variance in LES of evaporating spray. Combust Flame. https://doi.org/10.1016/j.combustflame.2006.07.003

Piock WF, Pinter A, Fraidl GK (2002) Gasoline direct injection and engine boosting. SAE TOPTEC, San Francisco

Reitz R (1987) Modeling atomization processes in high-pressure vaporizing sprays. Atomization spray technology

Rolf R (1999) Modeling spray atomization with the Kelvin-Helmholtz/Rayleigh-Taylor hybrid model. AtIzation Spray Technol. https://doi.org/10.1615/AtomizSpr.v9.i6.40

Rosin P, Rammler E (1933) The laws governing the fineness of powdered coal. J Inst Fuel

Rutland CJ (2011) Large-eddy simulations for internal combustion engines-a review. Int J Engine Res. https://doi.org/10.1177/1468087411407248

Senecal P, Pomraning E, Richards K, Som S (2013) An investigation of grid convergence for spray simulations using an LES turbulence model. SAE technical paper 2013-01-1083. https://doi.org/10.4271/2013-01-1083

Smagorinsky J (1963) General circulation experiments with the primitive equations: I. the basic experiment. Mon Wea Rev. https://doi.org/10.1175/1520-0493(1963)091%3c0099:gcewtp%3e2.3.co;2

The open source CFD toolbox (2014) http://www.openfoam.com

Tian J, Zhao M, Long W, Nishida K et al (2016) Experimental study on spray characteristics under ultra-high injection pressure for DISI Engines. Fuel. https://doi.org/10.1016/j.fuel.2016.08.086

Wadekar S, Yamaguchi A, Oevermann M (2019) Large-eddy simulation on the effects of fuel injection pressure on the gasoline spray characteristics. SAE technical paper 2019-01-0060. https://doi.org/10.4271/2019-01-0060

Waltner A, Lueckert P, Schaupp U, Rau E, Kemmler R, Weller R (2006) Future technology of the spark-ignition engine: spray-guided direct injection with piezo injector. In: 27th vienna motor symposium

Wang Y, Lee W, Reitz R, Diwakar R (2011) Numerical simulation of diesel sprays using an eulerian-lagrangian spray and atomization (ELSA) model coupled with nozzle flow. SAE technical paper 2011-01-0386. https://doi.org/10.4271/2011-01-0386

Chapter 7
Cavitation in Injectors: A Brief Review of the Diagnostics of Liquid-Vapour Flow Within Injector Nozzles

Aditya Saurabh

Abstract Practical injectors typically involve high speed flows and large static pressure variation along the liquid stream before it exits the injector. As a result, the phenomenon of cavitation and the formation of a liquid-vapor mixture within the nozzle is always a possibility. The effects of cavitation may be beneficial (improved atomization) or undesirable (damage to injector walls due to violent cavitation bubble collapse); but regardless of the nature of effects, in both cases it is important to characterize cavitation within injector nozzles and understand its dynamics. Previous work on the *diagnostics of cavitation within injectors* is reviewed here.

7.1 Cavitation

Vapour bubbles form in a liquid when it is subjected to a decreasing pressure when the same falls below a critical value; the critical value depends on several factors including the saturated vapour pressure, presence of impurities, dissolved gases, and the finish of the surfaces in contact with the liquid flow. This is cavitation (Brennen, 1995). The propensity of a liquid flow to cavitate is given by the cavitation number, $\left[(p_\infty - p_v)/\left(0.5\rho_l U_\infty^2\right)\right]$, with p_v denoting the vapor pressure at a reference temperature; p_∞, U_∞ the freestream pressure and velocity and ρ_l the liquid density. The presence of surface defects, impurities in the fluid, which act as nucleation cites for cavitation bubble formation; and the presence of dissolved gases in the fluid promote early cavitation. Depending on these factors, cavitation will occur at a certain value of the cavitation number and a reducing cavitation number within the flow will lead to an increasing size and number of cavitation bubbles.

Conditions for hydrodynamic cavitation are generally created at corners and area changes. It is sometimes also referred to as flash boiling (often in the context of gasoline injectors).

A. Saurabh (✉)
Department of Mechanical Engineering, Indian Institute of Technology Kanpur, Kanpur 208016, India
e-mail: asaurabh@iitk.ac.in

A. P. Singh et al. (eds.), *Simulations and Optical Diagnostics for Internal Combustion Engines*, Energy, Environment, and Sustainability,
https://doi.org/10.1007/978-981-15-0335-1_7

Cavitation bubbles themselves are highly dynamic and would go through stages of growth, oscillation, coalescence, formation of clusters/clouds, and collapse depending on various physical factors. Among these, the latter—bubble collapse—is a highly violent process responsible for the destructive capabilities of a cavitating fluid, and must therefore be avoided; specially in an injector for obvious reasons.

The advantages of cavitation are in creating a two-phase flow within the injector. As a result atomization is enhanced—likely at the cost of increased pressure drop. Cavitation induced in an injector nozzle prior to the exit, would also lead to increased turbulence levels within the liquid jet emanating from the injector, which would in turn result in enhanced jet breakup, atomization, and therefore vaporization of liquid fuels. For this reason, cavitation within injectors is an important phenomenon being actively investigated by the industry and academia. However, cavitation in injectors involves small time and length scales; and in a turbulent fluid flow its occurrence leads to complex multi-phase structures and interactions and is difficult to study experimentally (in particular, in-situ measurements) and numerically. In this report, a short account of recent experimental diagnostics is provided.

The effects of cavitation on spray formation and atomization has been reported in several previous studies. For instance, Baldwin et al. (2016) and Rachakonda et al. (2018) numerically investigated (including comparison with corresponding experimental results by the research group in case of Baldwin et al. (2016) and Zhang et al. (2014) for Rachakonda et al. (2018)) the spray characteristics from a gasoline direct injection VCO (valve covered orifice) nozzle under conditions where the internal flow would cavitate. Figure 7.1 from Baldwin et al. (2016) presents a visual comparison (experimental results) of spray formation from cavitating and non-cavitating nozzles. In comparison to the non-cavitating case, the spray corresponding

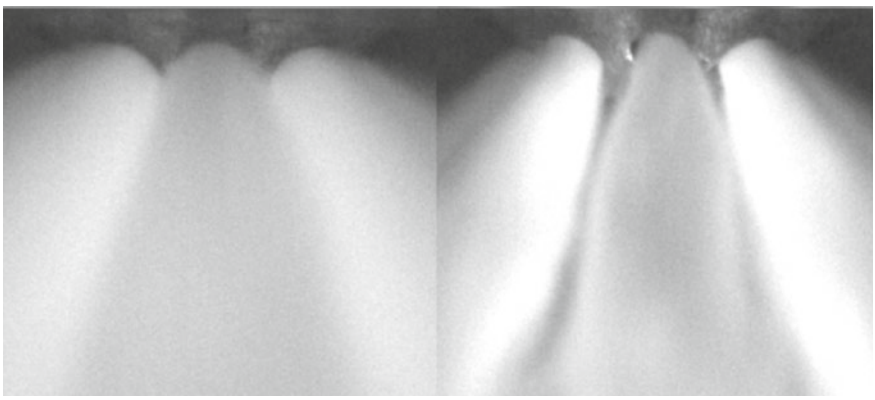

Fig. 7.1 Spray formation for a cavitating (left) and non-cavitating (right) multiport nozzle (Baldwin et al. 2016). For cavitating nozzles, the atomization is enhanced, spray angle is increased, and the penetration depth is correspondingly reduced. Standard approaches to correlations (Lefebvre and McDonell 2017) with respect to Weber or Reynolds numbers fail for spray characteristics of spray nozzles (Xu et al. 2013)

to the cavitating case is wider by a factor of about 1.5. Atomization is improved and these effects combined, the penetration length of the jet is reduced. Because of the phenomenon of vaporization within the nozzle, unlike non-cavitating nozzle sprays, properties of cavitating sprays may not be well-correlated with the Weber number; rather, the parameters governing cavitation (saturated pressure, cf. Xu et al. (2013)) and nozzle geometry become critical for the spray characteristics. For multi-nozzle configurations, it is quite common to obtain string cavitation/flash-boiling associated with transient vortical structures formed between pairs of nozzles (Andriotis et al., 2008; Gavaises et al., 2009; Baldwin et al., 2016). These are often observed during transient operation of multi-hole injectors when the unsteady flow field with intense vorticity connecting pairs of holes is formed at conditions conducive for cavitation (i.e. conditions at which even a single nozzle configuration would feature cavitation pockets).

In experiments, the effect of cavitation on spray formation can be diagnosed using the same techniques as for any spray: once the cavitating flow leaves the injector it is a two-phase flow just as any other spray. The reader is referred to other reviews (Chigier, 1983; Fansler and Parrish, 2014) on this aspect for further details. The diagnostics covered in this review concern the investigation of the cavitating flow as it evolves within the nozzle.

7.2 Diagnostics of Cavitating Flow Inside Injectors

To understand, control, and predict cavitation inside injectors, it becomes essential to perform diagnostics of the nozzle/injector flow and previous research falls into the following categories:

1. Optical diagnostics in the visible spectrum but with the injector geometry modified (often simplified) to use transparent materials (plastic or glass) at least along the desired path of light.
2. Diagnostics with high energy radiation (X-ray, neutron imaging) and with the injector material transparent to the radiation.
3. Diagnostics with magnetic resonance imaging of the cavitating nozzle flow.

Characterization of the two-phase flow within the nozzle due to cavitation often involves the determination of the spatial distribution of the vapour fraction. The vapour fraction is also the basis for comparison between experiments and numerical simulations of cavitating flow within injectors.

7.2.1 Diagnostics with Visible Light

Cavitation bubbles and clouds strongly scatter light and may be identified as dark regions within the nozzle in the backlighting or shadowgraphy configuration or as

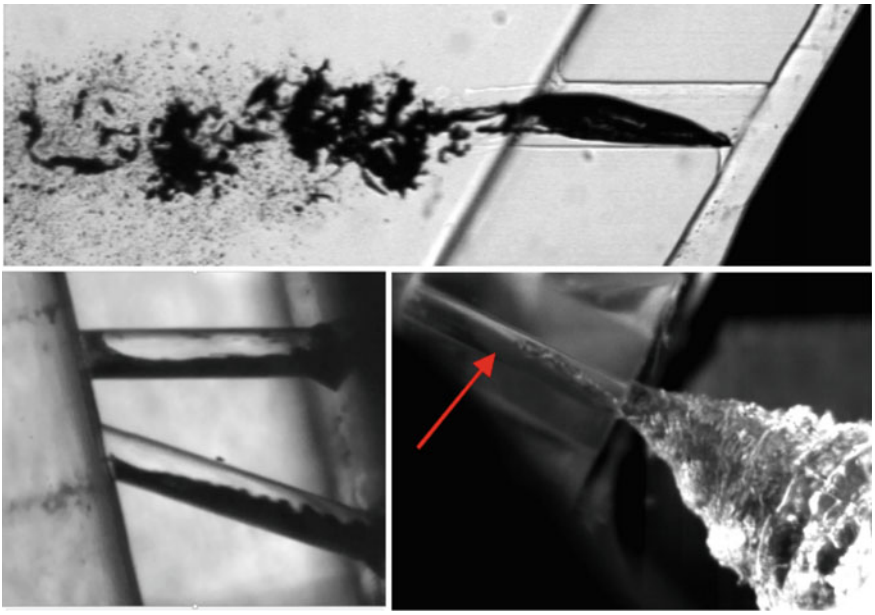

Fig. 7.2 Top: Cavitation in a glass model diesel injector illuminated by and LED light source (Miranda et al. 2003); left: cavitation inside nozzles obtained with backlit imaging using a plasma light source (Falgout and Linne 2016) and right: cavitating nozzle and spray illuminated by a pulsed laser (Mitroglou et al. 2011)

bright features in the forward scattering mode. Figure 7.2 shows some examples of the direct optical imaging of cavitation within injectors with the two methods. The high speed flow necessitates small exposure times (of the order of 100 nanoseconds) which is only possible with the use of short duration pulses from high power light sources. Mitroglou et al. (2011) for instance employed a ∼20W pulsed laser source for illumination.

The main drawback of optical methods with visible light is that the injector must be optically transparent. The material must be able to handle the high injection pressures (Falgout and Linne 2016). Finally, in order to obtain sharp images, differences in the optical path of light from different sections of the region of interest (including the small diameter of the order of 0.1 mm, cylindrical nozzle) due to curvature and changes in the refractive indices of the material, the liquid being tested, and the surrounding air or fluid (submerging the setup in a liquid in order to reduced differences in refractive indices helps (Miranda et al. 2003)) must be minimized. Miranda et al. (2003) and subsequent investigations on the setup, for instance, employed a glass prism and added α-methylnapthalene to the fuel in order to have a plane surface (removing the effect of curvature on optical path) and matching refractive indices between glass and the liquid being tested.

Because of the scattering of light from gas-liquid interfaces and additionally from the walls of the injector, optical methods are limited to visualization and identification of qualitative features of the cavitating flow. Measurements in this class of diagnostics deliver line-of-sight images and tomographic reconstruction is difficult because measurements from different angles not only sees different views of the cavitation geometry but also contains differences due to different optical path lengths if the rig is not axisymmetric. Light sheet methods are rare because of difficulties at the walls, and scattering problems. Often the injector test assembly is scaled up for the convenience of diagnostics (Park et al. 2008; Sou et al. 2012; Gavaises et al. 2009). In order to reduce curvature effects, a two-dimensional nozzle has often been investigated to study cavitation (Park et al. 2008).

Previous attempts to obtain quantitative characterization, specifically vapour fraction determination with diagnostics in the visible spectrum include Winklhofer et al. (2001), who used interferograms to obtain optical path lengths in experiments with a 2-D cavitating nozzle and used this information to infer the density of the two-phase mixture. Cavitation was observed at a pressure difference of 70 bar and was identified to coincide with choking of the fuel flow rate.

7.2.2 X-Ray and High-Energy Radiation Diagnostics

Quantitative diagnostics, in particular void or vapour fraction in a cavitating injector flow, is of particular importance for the validation of numerical simulations. For this purpose X-ray techniques which are employed for line-of-sight projected vapour fraction determination in sprays have been extended for the same study in cavitating nozzle flows in the forms of X-ray radiography (Mitroglou et al. 2016; Vabre et al. 2009), X-ray averaged tomography (Mitroglou et al. 2016; Bauer et al. 2012) (see Fig. 7.4 top panel), X-ray fluorescence measurements (with dissolved Krypton) (Duke et al. 2015), fluorescence spectroscopy (Duke et al. 2018) and phase contrast imaging (with Cerium as the contrast agent) (Duke et al. 2018).

X-ray diagnostics can be conducted at conditions that one cannot realise in optically-accessible setups. Depending on the material of the nozzle, specifically the absorption of X-rays by the material, the signal-to-noise ratio will be affected, with previously tested materials such as Beryllium or Aluminium giving high SNR. But the working pressures are reduced for such soft metals in comparison to steel used commonly in injectors. Duke et al. (2018) reported that Beryllium and Aluminium allow for maximum operating pressures in the range of 100 bar and 500 bar respectively with good SNR levels.

Small laboratory-scale X-ray sources are limited in their resolution (increased spatial resolution can be obtained at the cost of time resolution and vice versa) (Mitroglou et al. 2016) but large synchrotron X-ray facilities (Kastengren et al. 2012; Vabre et al. 2009) provide focused X-rays that allow higher spatial (of the order of μm) and temporal (of the order of μs) are possible (Duke et al. 2014, 2015, 2018).

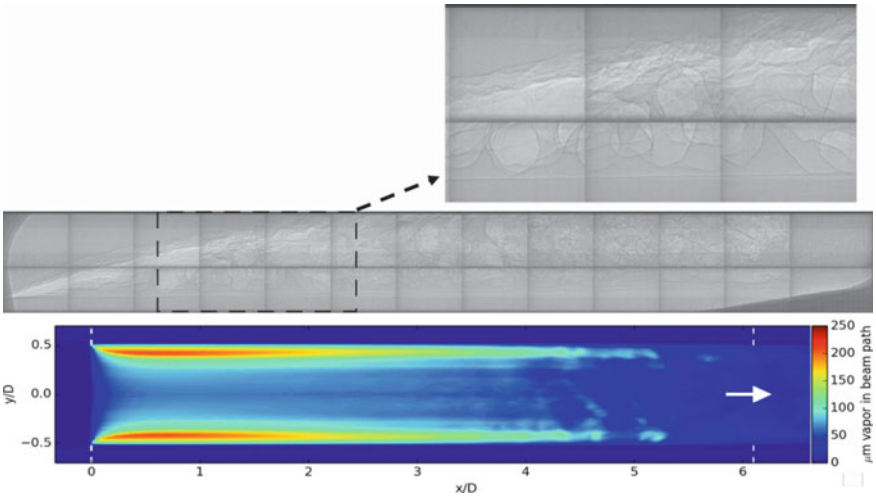

Fig. 7.3 Top: X-ray imaging of the liquid-vapour interface in a cavitating nozzle (Vabre et al. 2009); bottom: line-of-sight project void fraction from X-ray radiography of a cavitating nozzle. (Duke et al. 2015)

X-ray based techniques suffer similar limitations in the diagnostics of cavitating flows as they have for the diagnostics of sprays. It is only possible to obtain a line-of-sight imaging of the liquid-vapour interface; and details of cavitation bubbles and clouds are averaged out (cf. Fig. 7.3 top panel). For this reason their best application is the measurement of projected vapour fraction (Fig. 7.3 bottom panel) for use in numerical model validation studies—and in this respect the methods are the state-of-the-art.

As a means of improving X-ray radiography and phase contrast imaging, the use of Beryllium alloy for the injector to reduce the absorption of X-ray in the injector geometry has also been reported recently (Duke et al. 2017).

Similar studies with neutron beams instead of X-rays are ongoing presently (Toops et al. 2016) and we may expect to see new—possibly more detailed—results on cavitating flows in the coming years. Neutrons may be well suited for such study due to their sensitivity to hydrogen atoms in the fuel/water and low interactions with the metal part of the injector.

7.2.3 Magnetic Resonance Imaging

Magnetic resonance imaging of a cavitating nozzle has been reported recently by Adair et al. (2018) (see Fig. 7.4). However, in addition to the limitation of the choice of injector material due to the technique; the technique is also slow and only steady

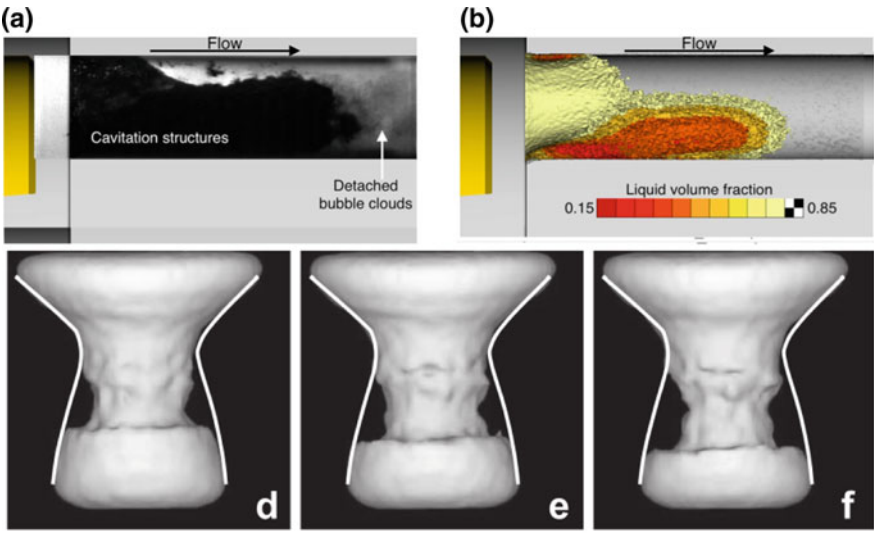

Fig. 7.4 Top: Comparison of shadowgraphy image of a cavitating nozzle and its X-ray CT reconstruction (Mitroglou et al. 2016); bottom: MRI images of a cavitating nozzle under different pressure differentials beyond the threshold for cavitation (Adair et al. 2018)

or periodic flows may be diagnosed. Given these conditions are met, the technique allows accurate three-dimensional reconstruction of a cavitating flow.

As mentioned previously, similar reconstruction may also be achieved using X-ray radiography.

7.3 Conclusions

Accessing the two phase flow field within injectors is difficult and requires special considerations concerning the test setup and diagnostic methodology. Research reported till date involves diagnostics with visible light, high energy radiation, and even magnetic resonance imaging. Cavitation within injectors be an important aspect for research and development in the near future and future developments in diagnostics are also expected.

Acknowledgements I benefitted greatly from the 2018 CECOST workshop on optical and laser diagnostics (Laser techniques for combustion diagnostics). This review was initiated as a project within the workshop and I am particularly thankful to Edouard Berrocal (Combustion Physics, Lund University) for his comments and suggestions on the work.

References

Adair A, Mastikhin IV, Newling B (2018) Motion-sensitized SPRITE measurements of hydrodynamic cavitation in fast pipe flow. Mag Resonance Imaging 49:71–77. https://doi.org/10.1016/j.mri.2017.12.025

Andriotis A, Gavaises M, Arcoumanis C (2008) Vortex flow and cavitation in diesel injector nozzles. J Fluid Mech 610:195–215. https://doi.org/10.1017/s0022112008002668

Baldwin E, Grover R, Parrish S, Duke D, Matusik K, Powell C, Kastengren A, Schmidt D (2016) String flash-boiling in gasoline direct injection simulations with transient needle motion. Int J Multiph Flow 87:90–101. https://doi.org/10.1016/j.ijmultiphaseflow.2016.09.004

Bauer D, Chaves H, Arcoumanis C (2012) Measurements of void fraction distribution in cavitating pipe flow using x-ray CT. Meas Sci Technol 23(5):055–302. https://doi.org/10.1088/0957-0233/23/5/055302

Brennen C (1995) Cavitation and bubble dynamics. Oxford University Press, Oxford

Chigier N (1983) Group combustion models and laser diagnostic methods in sprays: a review. Combust Flame 51:127–139. https://doi.org/10.1016/0010-2180(83)90093-7

Duke D, Swantek A, Tilocco Z, Kastengren A, Fezzaa K, Neroorkar K, Moulai M, Powell C, Schmidt D (2014) X-ray imaging of cavitation in diesel injectors. SAE Int J Engines 7(2):1003–1016. https://doi.org/10.4271/2014-01-1404

Duke DJ, Swantek AB, Kastengren AL, Powell CF (2015) X-ray diagnostics for cavitating nozzle flow. J Phys: Conf Ser 656:012110. https://doi.org/10.1088/1742-6596/656/1/012110

Duke DJ, Matusik KE, Kastengren AL, Swantek AB, Sovis N, Payri R, Viera JP, Powell CF (2017) X-ray radiography of cavitation in a beryllium alloy nozzle. Int J Eng Res 18(1–2):39–50. https://doi.org/10.1177/1468087416685965

Duke DJ, Kastengren AL, Matusik KE, Powell CF (2018) Hard x-ray fluorescence spectroscopy of high pressure cavitating fluids in aluminum nozzles. Int J Multiph Flow 108:69–79. https://doi.org/10.1016/j.ijmultiphaseflow.2018.05.026

Falgout Z, Linne M (2016) Novel design for transparent high-pressure fuel injector nozzles. Rev Sci Instrum 87(8):085108. https://doi.org/10.1063/1.4960402

Fansler TD, Parrish SE (2014) Spray measurement technology: a review. Meas Sci Technol 26(1):012002. https://doi.org/10.1088/0957-0233/26/1/012002

Gavaises M, Andriotis A, Papoulias D, Mitroglou N, Theodorakakos A (2009) Characterization of string cavitation in large-scale diesel nozzles with tapered holes. Phys Fluids 21(5):052107. https://doi.org/10.1063/1.3140940

Kastengren A, Powell CF, Arms D, Dufresne EM, Gibson H, Wang J (2012) The 7bm beamline at the APS: a facility for time-resolved fluid dynamics measurements. J Synchrotron Radiat 19(4):654–657. https://doi.org/10.1107/s0909049512016883

Lefebvre AH, McDonell VG (2017) Atomization and sprays. Taylor and Francis Inc

Miranda R, Chaves H, Martin U, Obermeier F (2003) Cavitation in a transparent real size VCO injection nozzle. In: ICLASS

Mitroglou M, Gavaises M, Nouri JM, Arcoumanis C (2011) Cavitation inside enlarged and real-size fully transparent injector nozzles and its effect on near nozzle spray formation. In: DIPSI workshop on droplet impact phenomena and spray investigation

Mitroglou N, Lorenzi M, Santini M, Gavaises M (2016) Application of X-ray micro-computed tomography on high-speed cavitating diesel fuel flows. Exp Fluids 57(11):1–14. https://doi.org/10.1007/s00348-016-2256-z

Park SH, Suh HK, Lee CS (2008) Effect of cavitating flow on the flow and fuel atomization characteristics of biodiesel and diesel fuels. Energy Fuels 22(1):605–613. https://doi.org/10.1021/ef7003305

Rachakonda SK, Wang Y, Grover RO, Moulai M, Baldwin E, Zhang G, Parrish S, Diwakar R, Kuo TW, Schmidt DP (2018) A computational approach to predict external spray characteristics for flashing and cavitating nozzles. Int J Multiph Flow 106:21–33. https://doi.org/10.1016/j.ijmultiphaseflow.2018.04.012

Sou A, Pratama RH, Tomisaka T (2012) Cavitation in a nozzle of fuel injector. In: Proceedings of the 8th symposium on cavitation

Toops T, Finney C, Nafziger E, Splitter D, Pawlowski A, Bilheux H, Santodonato L, Tremsin A (2016) Neutron imaging of intra-nozzle fluid dynamics in fuel injectors. In: 2016 SAE world congress

Vabre A, Gmar M, Lazaro D, Legoupil S, Coutier O, Dazin A, Lee W, Fezzaa K (2009) Synchrotron ultra-fast x-ray imaging of a cavitating flow in a venturi profile. Nuclear Instrum Methods Phys Res Sect A: Accel Spectrom Detect Assoc Equip 607(1):215–217. https://doi.org/10.1016/j.nima.2009.03.192

Winklhofer E, Kull E, Kelz E, Morozov A (2001) Comprehensive hydraulic and flow field documentation in model throttle experiments under cavitation conditions. In: ILASS-Europe

Xu M, Zhang Y, Zeng W, Zhang G, Zhang M (2013) Flash boiling: easy and better way to generate ideal sprays than the high injection pressure. SAE Int J Fuels Lubr 6(1):137–148. https://doi.org/10.4271/2013-01-1614

Zhang G, Xu M, Li T, Grover RO, Kuo T, He Y (2014) A study of near-field spray structure under superheated conditions of a gasoline fuel spray. In: ILASS Americas 26th annual conference on liquid atomization and spray system

Chapter 8
Multiphase Phenomena in Diesel Fuel Injection Systems

Ioannis K. Karathanassis, Foivos (Phoevos) Koukouvinis and Manolis Gavaises

Abstract Fuel Injection Equipment (FIE) are an integral component of modern Internal Combustion Engines (ICE), since they play a crucial role in the fuel atomization process and in the formation of a fuel/air combustible mixture, consequently affecting efficiency and pollutant formation. Advancements and improvements of FIE systems are determined by the complexity of the physical mechanisms taking place; the spatial scales are in the order of millimetres, flow may become locally highly supersonic, leading to very small temporal scales of microseconds or less. The operation of these devices is highly unsteady, involving moving geometries such as needle valves. Additionally, extreme pressure changes imply that many assumptions of traditional fluid mechanics, such as incompressibility, are no longer valid. Furthermore, the description of the fuel properties becomes an issue, since fuel databases are scarce or limited to pure components, whereas actual fuels are commonly hydrocarbon mixtures. Last but not least, complicated phenomena such as phase change or transition from subcritical to transcritical/supercritical state of matter further pose complications in the understanding of the operation of these devices.

8.1 Introduction

The link between nozzle flow and spray formation has long been an open issue in the IC engines community. Phase-change dominates injection of liquid fuels into combustion engines. Depending on the nozzle design and/or operating conditions, cavitation or flash boiling (for gasoline injectors) are the first phase-change processes

I. K. Karathanassis (✉) · F. Koukouvinis · M. Gavaises
School of Mathematics, Computer Science & Engineering, Northampton Square, City, University of London, London EC1V0HB, UK
e-mail: ioannis.karathanassis@city.ac.uk

F. Koukouvinis
e-mail: foivos.koukouvinis.1@city.ac.uk

M. Gavaises
e-mail: m.gavaises@city.ac.uk

A. P. Singh et al. (eds.), *Simulations and Optical Diagnostics for Internal Combustion Engines*, Energy, Environment, and Sustainability,
https://doi.org/10.1007/978-981-15-0335-1_8

taking place even before reaching the combustion chamber and affect atomisation. It is widely accepted that nozzle flow plays a major role in fuel atomisation and emissions in Diesels. Today's commercial FIE reach 2750 bar while injection pressures as high as 4,500 bar are being investigated. The present work aims to discuss in detail the importance of phase change phenomena and flow mechanisms in the operation of FIE equipment, or simplified models resembling such equipment, discussing internal flow effects. Also, a brief discussion on fuel properties, subcritical/transcritical fluid state and how it affects atomization will be discussed. The discussions will be based on prior experimental investigations or numerical studies of the authors' group.

8.2 Flow Topology

Real-size exact replicas of Diesel nozzles made from transparent (e.g. acrylic) materials have been successfully manufactured, able to withstand pressures of the order of 1000 bar (Mitra et al. 2019). Parallel to those activities, several studies have focused on illustrating the in-nozzle, two-phase flow topology in transparent, enlarged replicas at lower injection pressures (see selectively Reid et al. 2010; Reid 2014; Gavaises et al. 2009). Flow similarity to the actual injector flow is ensured based on non-dimensional numbers, i.e. with the use of the Reynolds and cavitation numbers defined as follows:

$$Re = \frac{u \cdot D}{\nu} \tag{8.1}$$

$$CN = \frac{p_{inj} - p_o}{p_o - p_{sat}} \tag{8.2}$$

where u, D and ν in the Reynolds-number definition are the flow average velocity, the orifice internal diameter and the diesel kinematic viscosity, respectively. Referring to the cavitation number definition, p_{inj}, p_o and p_{sat} are the injection, back (outlet) and saturation pressure, respectively. An additional definition of the cavitation number has also been used in the literature (Schmidt et al. 2014):

$$\sigma = \frac{p_{inj} - p_{sat}}{\frac{1}{2}\rho u^2} \tag{8.3}$$

where ρ, u are the fuel density and the flow velocity, respectively. Nevertheless, Eq. (8.2) will be used throughout this chapter where increasing values of CN correspond to more extensive cavitation formation.

8.2.1 Optical Methods

Optical methods, i.e. back-light diffuse illumination or Mie scattering (Pickett et al. 2009; Bardi et al. 2013; Westlye et al. 2017) have been extensively employed for the

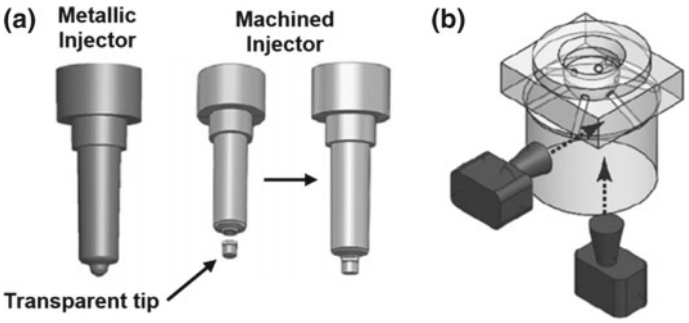

Fig. 8.1 **a** Nominal fabrication steps of injector/transparent tip assembly **b** 3-D view of the transparent-tip schematic indicating visualisation angles. The tip realises a six-hole Diesel injector, with all holes at angles of 65° with reference to the injector main axis (Mitroglou et al. 2014)

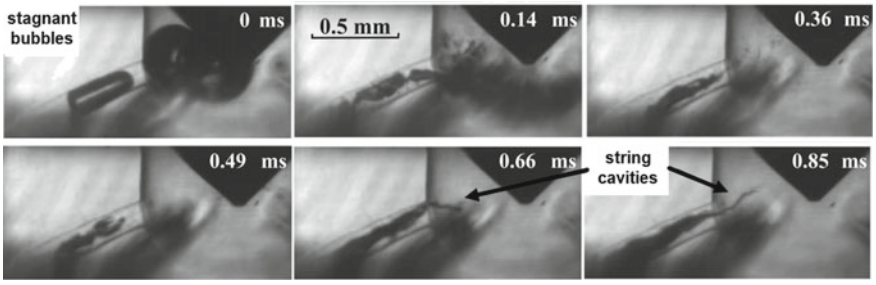

Fig. 8.2 Sequence of representative time instances of an injection event having a duration of 3.5 ms at 300 bars injection pressure. The injection hole diameter is 0.160 mm (Mitroglou et al. 2014)

visualization of cavitating structures emerging in injector flows. Such methods benefit from a relatively simple and straightforward optical set-up, mainly comprising an illumination source, a set of diffusers/lenses and a high-speed camera recording either the shadows or the Mie signal produced by the vapour formed within the injector orifice. The schematic shown in Fig. 8.1 illustrates the assembly of a real-size injector with a transparent tip. The metallic body of the actual injector is machined-off below the sac region and an acrylic part realising the sac and injector holes is clamped into position (Fig. 8.1a), allowing the internal flow to be realised from different angles (Fig. 8.1b). Due to the limited durability of acrylic, experiments reported in this chapter have been performed for injection pressures up to 500 bars (Mitroglou et al. 2014).

A representative injection event employing the transparent tip depicted in Fig. 8.1 is presented in Fig. 8.2, illustrating the formation of cavitation in the sac region and injector holes. The sequence at 0 ms reveals that bubbles, consisting of congested gas and/or fuel vapour, occupy a large portion of the sac and injector-hole regions prior to injection. Latter time instances clearly demonstrate the presence of fuel vapour clouds within the injector hole during the needle-opening phase. As can be seen,

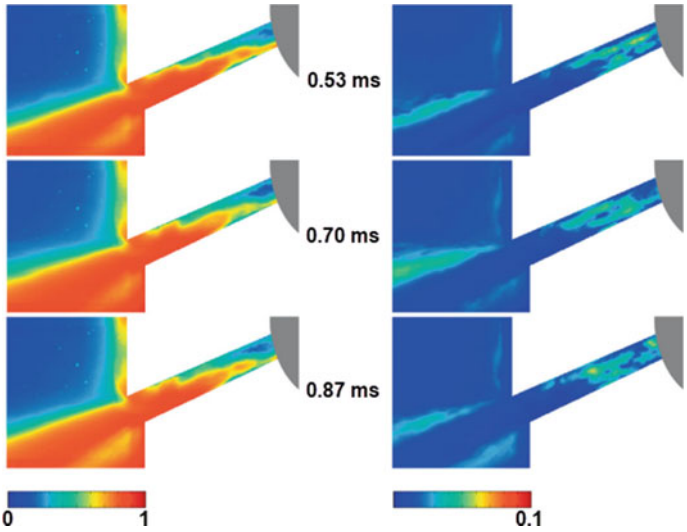

Fig. 8.3 Spatial distribution of average and standard deviation demonstrating the presence of an interphase, i.e. cavitation bubbles and two-phase spray mixture inside and downstream of the nozzle exit, respectively during selected time-steps of one injection event corresponding to the raw images depicted in Fig. 8.2 (Mitroglou et al. 2014)

cavitation is always evident during the first half of injection duration with the cavity forming in the sac region, in the vicinity of the needle tip and propagating into the orifice core. These distinct cavitation structures of elongated shape, which are not attached to the injector walls, are characteristically termed as string cavities.

Suitable post-processing and averaging of a large number of time-resolved data can provide useful information on the extent and dynamical behaviour of fuel vapour within the injector during the entire injection event. Figure 8.3 presents mean vapour (or two-phase mixture) presence probability images corresponding to the high-speed images presented in Fig. 8.2, as produced by a series of different injection events. Also depicted in Fig. 8.3 are the respective standard deviation images, which are suitable for highlighting the transient flow features. The mean images corresponding to the needle-opening phase of the injector operation illustrate that the vapour-presence probability is close to 1 in the lower part of the injection hole, hence denoting the presence cavitation during the needle-valve opening. As also revealed by the standard deviation images, transient features within the injector-nozzle are associated with unstable spray behaviour. The time instances depicted in Fig. 8.3 clearly demonstrate that the upper part of the injected spray plume exhibits a flapping behaviour and the spray cone angle fluctuates.

Apart from real-size optical injector tips, fully transparent enlarged injector replicas have been used in experimental investigations allowing cavitating structures to be visualised at larger length-scales, hence enhancing the visualisation resolution (Arcoumanis et al. 2001). A representative example of an enlarged replica of a 5-hole asymmetrical injector is depicted in Fig. 8.4, with a nominal injection-hole diameter

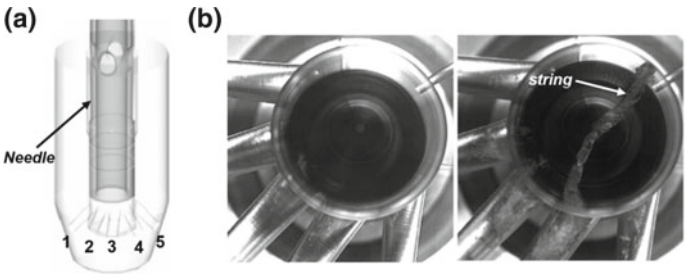

Fig. 8.4 **a** Schematic and bottom-view photograph of the enlarged injector replica, depicting the needle, sac-region an injector holes. **b** Bottom view of the two-phase flow emerging inside the replica. The presence of a string cavity can be clearly discerned in the sac region, also extending into one of the injection holes (CN = 4.0, Re = 68000) (Andriotis et al. 2008; Andriotis and Gavaises 2009)

of 1.5 mm (Andriotis et al. 2008; Andriotis and Gavaises 2009). The schematic of the arrangement, shown in Fig. 8.4a, incorporates a hollow slide-type needle that covers the injection holes directly, and minimises the sac volume when fully closed. The injector replica discharges the working medium directly into ambient air under atmospheric pressure and at room temperature and enables the concurrent visualization of the atomization process and the transient cavitating strings arising in the injector-holes and sac regions, as shown in Fig. 8.4b.

Even more simplified, enlarged single-orifice layouts have been designed and examined with reference to injector flows, in order to shed light to the physical flow processes influencing the onset, development and collapse of cavitation. An injector-mimicking orifice that excludes flow perturbations due to the presence of multiple nozzle holes and transient needle motion is depicted in Fig. 8.5 (Mitroglou et al. 2017). The optical part comprises an off-set injection hole preceded by an axisymmetric cylindrical flow-path replicating the sac region (Fig. 8.5a). An asymmetric metallic needle, also depicted in Fig. 8.5a, is placed at a fixed, yet adjustable position in the sac region and along with the offset injector nozzle give rise to a flow pattern which leads to the formation of cavitation mainly on one side of the nozzle. Hence, fundamental flow processes associated with cavitation dynamics can be visualised from different angles and in a fully controllable manner by adjusting the position of the metallic needle, as well as the upstream and downstream pressures. A metallic manifold is assembled upstream the examined nozzle configuration, so as to ensure a parallel and unperturbed flow entering the injector-replicating layout. The diesel fuel exiting the nozzle is subsequently discharged into a chamber filled with liquid as well, shown on the lower part of Fig. 8.5c. Hence, the overall configuration can be characterised as a submerged orifice.

The cavitating flow arising inside the single orifice injector depicted in Fig. 8.5 is elucidated by the sequence of high-speed images presented in Fig. 8.6. For flow conditions characterised by Re = 53760 and CN = 1.3, a cloud cavity is established in the entrance region of the orifice with an unstable trailing edge from which coherent vortical structures are shed, as highlighted by the red circle in time instances after

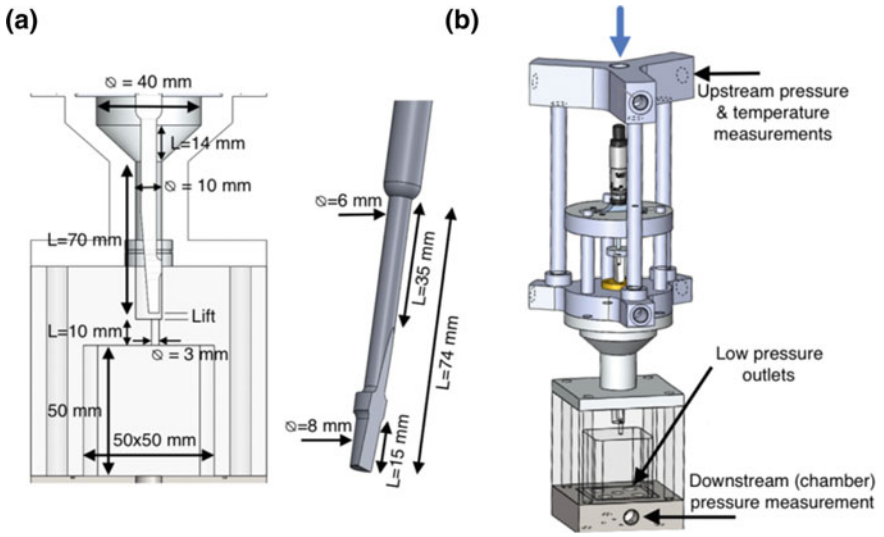

Fig. 8.5 **a** Cross-sectional view of the optical part realizing the single orifice of the injector replica. The metallic needle is also discernible in the middle of the part, while a detailed view of the needle geometry is shown on the right part of the figure. **b** Schematic of the part/manifold assembly (Mitroglou et al. 2017)

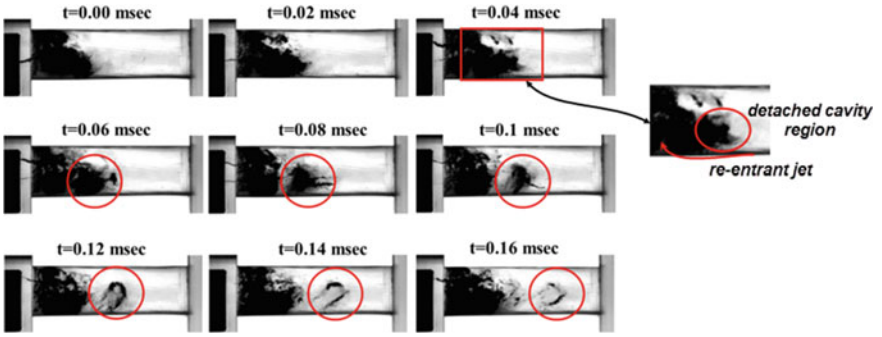

Fig. 8.6 Sequence of side-view high-speed images produced by diffuse back-illumination for the single-orifice replica (needle lift fixed at 0.5 mm, CN = 1.3 and Re = 53760) (Mitroglou et al. 2017). Flow is from left to right

0.06 ms. The underlying cause for the formation of cloud cavitation in the vicinity of the nozzle wall is the flow separation downstream the geometrical constriction between the needle and needle seat. Hence, the low pressure prevailing in the core of the recirculation pattern leads to the formation of an adverse pressure gradient in the lower part of the nozzle entrance region. This pressure gradient urges liquid to flow opposite to the main flow, as denoted in the detailed view of the 0.04 ms time instance (Fig. 8.6). This is a well-known flow mechanism, commonly termed

as re-entrant jet in the literature (Gopalan and Katz 2000; Stutz and Legoupil 2003), which has been demonstrated to be responsible for a cavity shedding sequence, made evident in the specific case as well, by the time instances between 0.04 and 0.16 ms. A coherent vaporous structure can be seen to completely detach from the main cloud at t = 0.06 ms and being convected towards the nozzle outlet by the main flow in the subsequent time instances. As shown by the time instance at t = 0.12 ms, the vortical cavitating structure obtains a hairpin shape and eventually collapses once it encounters a flow region of elevated pressure. The vortex ligaments are separated almost entirely at t = 0.16 ms due to viscous decay, while it is worth pointing out that the cavitating vortex collapses in the near-wall region, highlighting a typical mechanism of erosion formation in fuel injectors, as will be discussed in more detail in a subsequent paragraph.

Apart from physical inspection of the in-nozzle cavitation development and collapse, statistical treatment of a large number of high-speed images can provide information on the extent of vapour formation and highlight transient features of cavitation owed solely to the flow conditions. Figure 8.7a presents characteristic time instances of the cavitating flow arising in a similar single-orifice layout as the one depicted in Fig. 8.5, with the exception that the needle tip and sac wall have a hemispherical rather than a flat outline. A cloud cavity, once again sets in at the lower part of the nozzle wall with the distinct feature of exhibiting an oscillating behaviour with a frequency of approximately 296 Hz. Although the cavity-trailing region is unstable, the shedding sequence is associated with a full collapse of a part of the main cloud and hence cannot be attributed to the re-entrant jet mechanism. A mechanism based on the formation of a shock-wave within the separated cloud cavity causing its partial collapse, as described in (Ganesh et al. 2016), seems suitable to describe the cavitation dynamics in the specific case. The mean vapour presence probability and standard deviation images depicted in Fig. 8.7a–b clearly highlight the transient behaviour of the cavity development. As can be seen by comparison of the mean images, increase of CN leads to a more extensive cavity attached to the lower part of the orifice wall. Furthermore, it can be deduced through the standard deviation images that increase of CN enhances the oscillatory motion of the cavity, as the extent of the region exhibiting high values increases as well. An additional observation, is that the mean and standard deviation images also highlight the presence of vortical (or string) cavities emanating from the needle tip. Their highly transient nature is once again verified by the low mean and high standard deviation values.

The experimental investigations incorporating the simplified single-orifice injectors discussed above demonstrate that fundamental cavitation processes can be elucidated in such configurations, which omit additional perturbations probable to set in due to geometry complexity. The cavitation regimes identified in enlarged replicas also arise during the operating cycle of actual fuel injectors and therefore identification of the underlying flow processes, e.g. pressure gradients in the orifice, presence and topology of vortical motion, shockwave dynamics, can be directly connected to spray atomisation, injector fuel delivery effectiveness and durability.

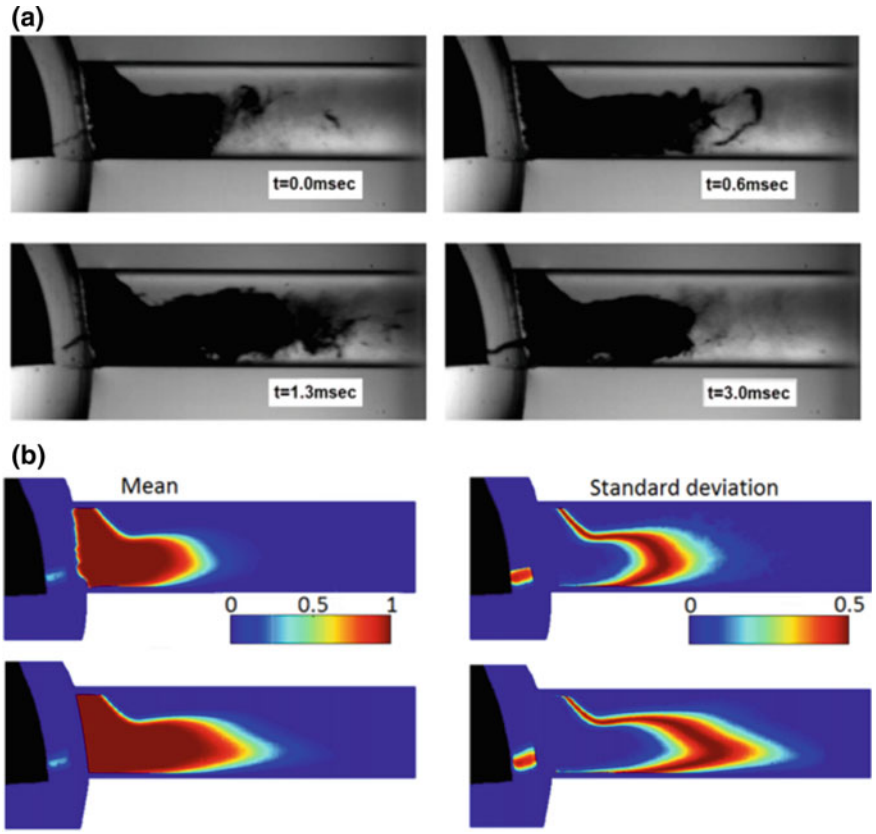

Fig. 8.7 **a** Time instances of the cavitating flow arising in a single-orifice replica with curved needle tip and sac wall. **b** Mean and standard deviation images of the in-nozzle vapour extent (CN = 1.6 (top) − 1.8 (bottom), Re = 30000 and needle lift of 0.5 mm)

8.2.2 X-Ray Phase Contrast Imaging (XPCI)

8.2.2.1 Vapour Extent and Flow Dynamics

Optical imaging, although offers useful information on in-nozzle cavitation characteristics, is limited as a flow visualisation technique by the excessive light scattering in the presence of very low amounts of vapour. In fact, it has been demonstrated that vapour volume fractions of order of 0.15 can completely block a visible light source (Ganesh et al. 2016). XPCI is also based on the interaction of irradiation with matter in the same manner as optical visualisation. A refraction index n can be defined for x-ray beams in the form $n = \delta + \beta i$, with the real part δ and the imaginary part β corresponding to the phase shift intensity and decrease (absorption) of the x-ray

wave, respectively (Russo 2014). XPCI takes advantage of the δ value of the refractive index corresponding to beam scattering, which is orders of magnitude weaker compared to visible light for hydrocarbon fuel (Im et al. 2013). Contrast fluctuations in a phase-contrast image are therefore designated by much stronger index gradients compared to optical methods and the scattered beam collected by the sensor bears information for all interactions occurring along its path (Linne 2012). In other words, features of the cavitating flow, especially in the core of a nozzle, where light visualisation is not possible due to high optical thickness, can be elucidated through XPCI.

An XPCI investigation of the two-phase flow arising in the single-hole injector orifice shown in Fig. 8.7 has been conducted employing a high-flux, 12 keV parallel x-ray beam, as described in detail in (Karathanassis 2018). As depicted in Fig. 8.8, the white x-ray beam, after irradiating the injector orifice, is converted to visible light by a scintillator crystal and subsequently captured by a high-speed camera. A sample raw image of the irradiated geometry is shown on the left part of Fig. 8.8 illustrating the beam circular cross-section. Therefore, the orifice is irradiated in a successive manner along its length, which is divided into five characteristic locations. A spatial overlap has been maintained in all locations, so as to ensure a high signal to noise ratio.

An indicative post-processed x-ray image is depicted in Fig. 8.9a illustrating the prevailing cavitation regime within the orifice for a needle lift of 0.5 mm. Since the cavitation number value characterising the flow conditions is rather high (CN = 7.7),

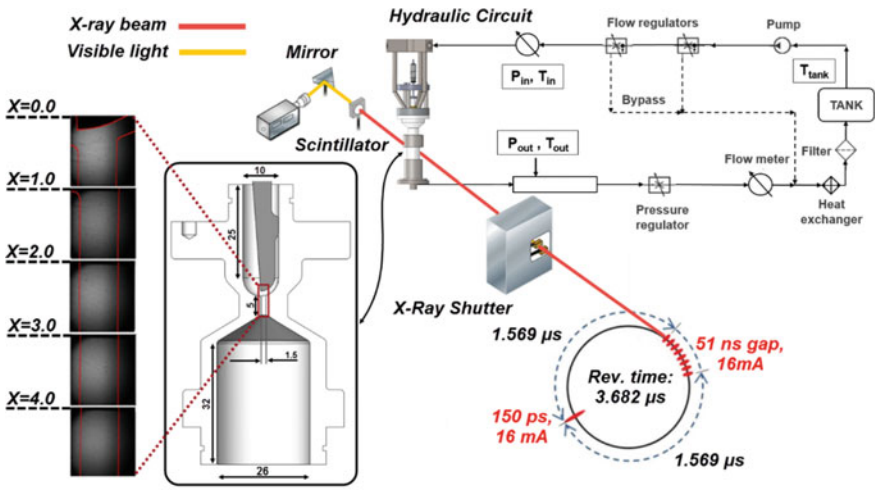

Fig. 8.8 XPCI test rig employing synchrotron radiation. The synchrotron beam-pulsation mode comprises a single pulse of 150 ps in duration, followed by eight short pulses separated by time intervals of 51 ns. Six of the eight pulses of the bunch was utilised allowing a shutter exposure time of 347 ns. The spatial resolution in the irradiated characteristic locations (X = 0 − 5 mm) of the orifice is 5 μm/pixel. The axisymmetric orifice shown was fabricated by a carbon-fibre composite, which causes lower x-ray absorption compared to metals (Karathanassis 2018)

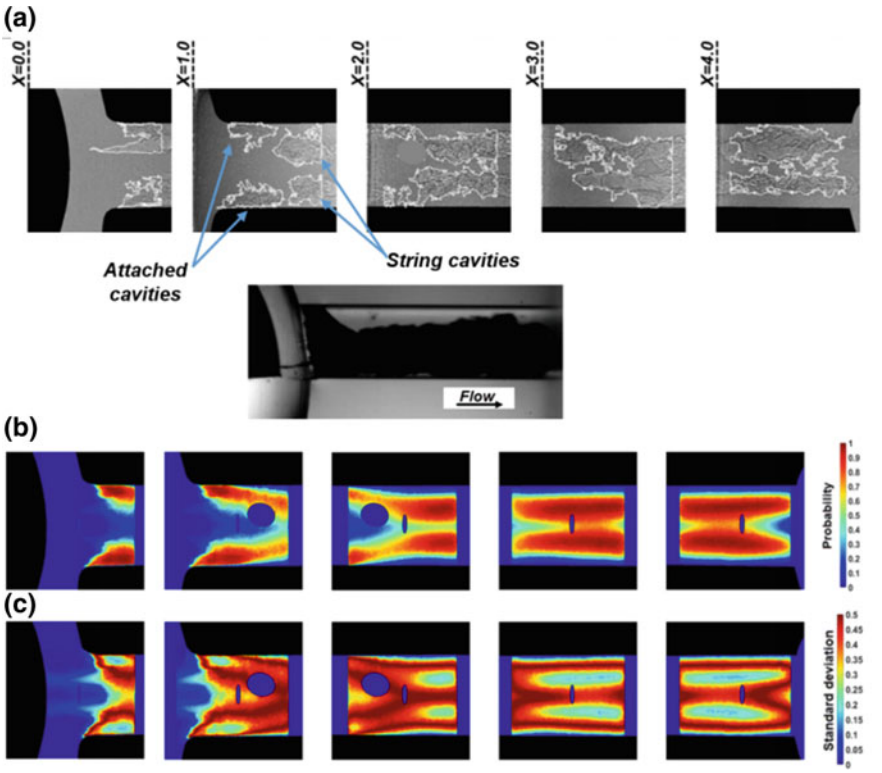

Fig. 8.9 **a** Indicative post-processed time instance of the cavitation development (visualised at 67,200 fps) along the orifice length for Re = 35500, CN = 7.7 and needle lift of 0.5 mm (top view) (Karathanassis et al. 2018). The cavity interphase is denoted by the white line. Vertical lines at the edges of each panel signify the extent of the region where high signal-to-noise ratio could be obtained. Artefacts due to scintillator crystal imperfections have been omitted in grey colour. The inset of the figure shows a representative image obtained by backlight illumination for similar flow conditions. **b** Mean vapour-presence probability and **c** standard deviation images produced by 16,000 radiographies for each characteristic location

the entire orifice length is occupied by a pair of well-established strings with highly unstable interfaces. Attached cavities can also be discerned in the locations closer to the orifice entrance (X = 0.0 − 1.0 mm), while it should be noted that the two cavitation regimes can be clearly differentiated in the phase contrast image. A side-view raw image obtained by backlight illumination is also presented as an inset in Fig. 8.9a. Juxtaposition of the two images highlights that interfacial perturbations in the cavity outline, not discernible in the visible-light image, are clearly captured in the x-ray image. Besides, the large extent of cavitation within the orifice blocks light completely and, thus no specific structures can be differentiated in the optical image.

Phase contrast images can be further utilised to extract temporal information regarding the in-nozzle cavitation development. For instance, Fig. 8.9b depicts the mean and standard-deviation images of the vapour extent within the orifice, verifying that, for the specific flow conditions, stable string cavities establish in the largest part of the orifice. It is evident by the close-to-unity probability values obtained that vapour occupies almost the entire orifice cross-section for $X \geq 2.0$, whereas the low standard deviation values in the core of the vaporous structures denote that the strings, although present substantial interfacial fluctuations, their coherence is never disrupted during the manifestation of the phenomenon.

The faithful capture of interfacial fluctuations offered by XPCI can be further exploited to obtain information on the underlying secondary flow motion responsible for the cavities onset. It is well established in the literature that string cavities emanate due to pressures lower than the liquid saturation pressure prevailing in the core of coherent vortices. Hence, the well established strings shown in Fig. 8.9 can be correlated to the presence of longitudinal vortices within the orifice. In fact, inspection of the radiographies has verified that for CN > 3.0 the cavity interface oscillates laterally with a frequency that is representative of the intensity of the underlying recirculating motion. Figure 8.10 depicts the Fast Fourier Transform of the cavity radius waveform at a characteristic location depicted in the inset of the figure. By comparing Figures Fig. 8.10a and b, it can be observed that by increase of the Reynolds and cavitation number, the prevailing oscillation frequency f shifts from 340 to 544 Hz. Also taking advantage of theoretical models correlating the vortical motion intensity Γ with f (Arndt 2002), for instance $\Gamma \sim f \cdot 4\pi^2 \cdot r_c^2$ (r_c being the cavity radius) (Franc and Michel 2005), quantitative information regarding the increase in intensity of the longitudinal vortices can be derive. For instance, since

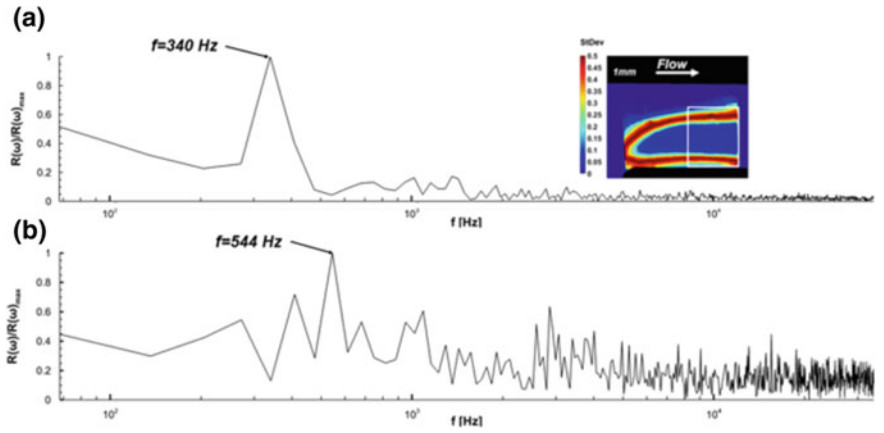

Fig. 8.10 Frequency spectrum of the string cavity radius normalised by the maximum radius recorded: **a** Re = 18000, CN = 3.2 and **b** Re = 35500, CN = 4.0 (needle lift of 0.5 mm in both cases). Radius values have been averaged along the white-square area of the inset (Karathanassis 2018)

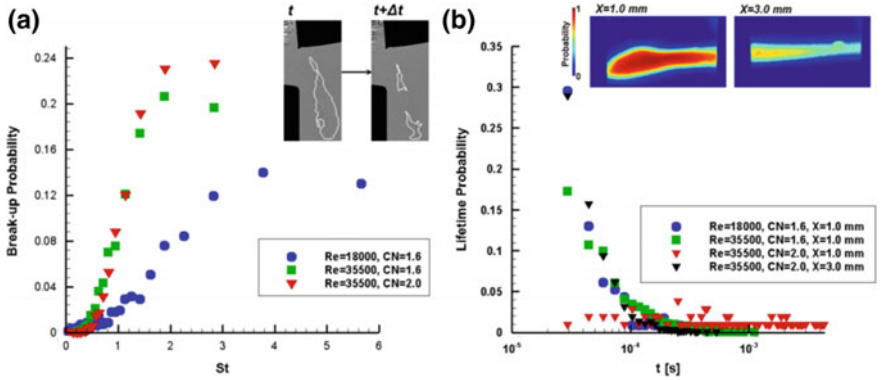

Fig. 8.11 **a** String break-up probability with Strouhal number $St = f \cdot L/U$, f being the break-up frequency, L(=5 mm) the nozzle length and U the nominal flow velocity. **b** String lifetime probability; the inset depicts an indicative structure under consideration (Karathanassis 2018)

the cavity has been measured equal to 0.306–0.388 mm for the cases corresponding to Fig. 8.10a and b, respectively, the recirculation intensity is calculated to be approximately 2.5 higher in the second case.

XPCI, owing to its high temporal and spatial resolution, can also be utilised to obtain quantitative information regarding the dynamics of highly-transient vaporous structure arising for moderately cavitating flows. For instance, referring to the flow layout depicted in Fig. 8.8, Fig. 8.11a shows the probability of a string cavity to break up into to two (or more). As Re and CN increase, the cavities become more coherent, since the break-up prevailing frequency decreases. Besides, Fig. 8.11b demonstrates that string cavities (an indicative example is shown in the inset of the figure) are expected to live longer prior to their collapse for increased Re and CN. Transient cavitation structures have considerable after-effects regarding injector shot-to-shot fuel delivery variability and induced erosion; hence, identification of their dynamics in a consistent manner is highly valuable for industrial-scale applications, as well.

8.2.2.2 Fuel Effects

Fuel additives exhibiting a viscoelastic behaviour added to base Diesel blends in ppm concentrations have been demonstrated to reduce injector deposits but also to have an effect on the topology of the two-phase flow arising in the injector nozzle (Naseri et al. 2018). XPCI data, although produced through a line of sight method, in essence contain information regarding the 3-dimensional extent of vapour within the orifice and, hence, constitute an ideal method for pinpointing differences between different diesel blends. Figure 8.12a presents mean vapour-probability images of the flow arising within the single orifice injector (refer to Fig. 8.8) for a base and an additised compound, where viscoelastic polymers have been added in a concentration of 500 ppm w/w. The bulk thermophysical properties of the two compounds

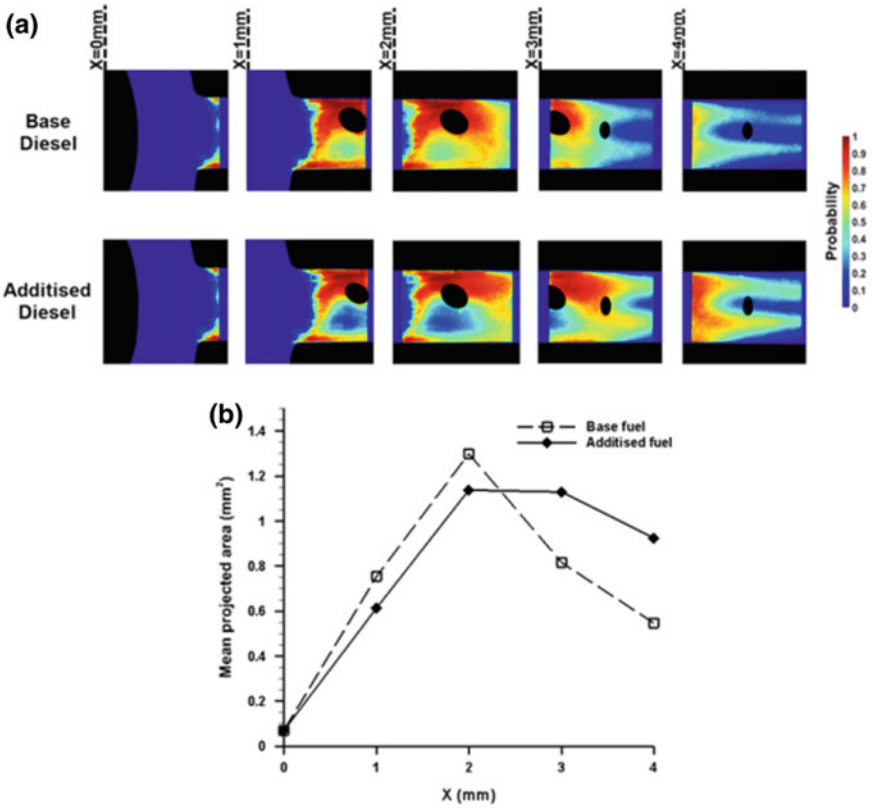

Fig. 8.12 **a** Top-view contour plots of the in-nozzle mean vapour-presence probability for different diesel-fuel compounds. **b** Mean surface of the cavity projection along the orifice length (Needle lift of 1.0 mm, Re = 35500, CN = 6.0) (Karathanassis et al. 2018)

are considered to be the same. The contours plots depict a considerably different cavitation topology compared to Fig. 8.9, as cloud cavitation is now prevalent in the major part of the orifice. This different flow behaviour is attributed to the different value of the needle lift, 1.0 mm instead of 0.5 mm, which modifies the recirculation pattern that arises downstream the geometrical constriction. Comparison of the upper and lower panels of Fig. 8.12a makes clear that the presence of additives reduces the extent of cloud cavitation ($X \leq 2.0$ mm), while on the contrary enhances string cavitation setting in towards the nozzle outlet ($X \geq 2.0$ mm). The differences in the vapour extent present in the nozzle for the two diesel compounds are quantified by the vapour mean projected area along the orifice length, shown in Fig. 8.12b. The extent of the cloud cavity in the additised diesel case is reduced by approximately 18.5%, whereas the volume occupied by string cavities is increased by about 69% compared to the base diesel fuel. A mechanism for this distinct flow behaviour of viscoelastic diesel fuel, as proposed in (Karathanassis et al. 2018; Naseri 2018), lies

in the interaction of viscoelastic micelles (Dreiss 2007) with coherent vortical motion in the macroscale, as well as with turbulence generating vortices in the microscale (Tsukahara et al. 2013).

Additional information on the effects of viscoelastic additives on string-cavitation dynamics can be obtained with an analysis similar to that presented in Fig. 8.11.

Figure 8.13a comparatively presents the lifetime probability for the two blends of the string cavities arising within the orifice for a needle lift of 0.5; refer to Fig. 8.9 depicting the prevailing cavitation topology for the specific flow conditions. The string lifetime for the additised fuel obtains relatively even probabilities for values up to 0.2 ms, whereas the two prevailing frequencies for the base blend are below 0.05 ms. Besides, similar to Fig. 8.10, Fig. 8.13b illustrates the string radius fluctuation in the frequency domain. It is clear that the string fluctuation is more violent regarding the base fuel with at least three prevailing frequencies. On the contrary, only one clear prevailing frequency of 409 Hz is evident for the additised fuel. Once again, the single peak observed and, in fact, at a lower frequency value compared to the base sample, is indicative of a less-perturbed flow. In other words, viscoelastic additives reduce the level of turbulence in the orifice, i.e. the magnitude of the small-scale vortices that would interact and lead to the eventual decay of

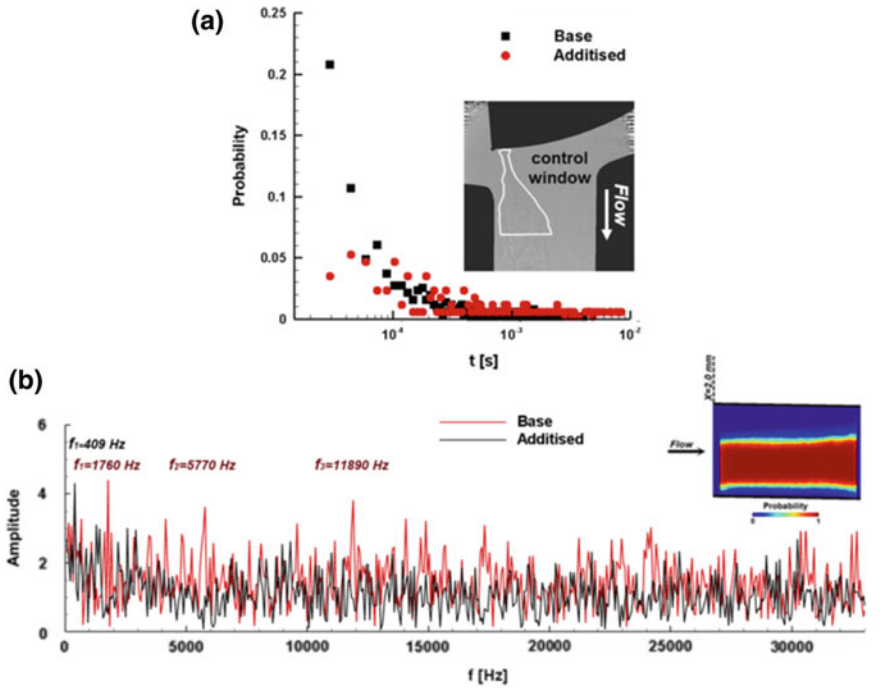

Fig. 8.13 String Cavitation dynamics for needle lift of 0.5 mm Re = 35500, CN = 7.7: **a** string-life probability for the two diesel blends. The control window is located in the vicinity of the needle tip, as denoted by the white line. **b** Fast Fourier Transform of the string radius fluctuation with time. The radius has been averaged in the control window shown as an inset (Naseri 2018)

the string coherence, thus increasing the string lifetime and reducing its interfacial fluctuations. The turbulence-reducing effect of viscoelastic additives has been well documented with reference to single-phase flow (Dimitropoulos et al. 1998; Pereira et al. 2017). Control of cavitation dynamics and, in a second step spray atomisation process in a consistent manner, with the addition of viscoelastic polymers in Diesel fuel is expected to have a tremendous positive impact on the fuel efficiency of diesel engines.

8.2.2.3 Velocimetry Employing XPCI

A technique bearing resemblance to Particle Tracking Velocimetry (PTV) (Kitagawa et al. 2005; Sathe et al. 2010) can be employed in combination with XPCI to provide an estimate of the planar velocity field in the vapour region. The high temporal resolution offered by synchrotron x-ray imaging allows the tracking of distinct flow features, such as vaporous structures or interfacial perturbations, refer indicatively to Fig. 8.14a. Besides, the small exposure time (of the order of nanoseconds) due to the x-ray beam pulsation mode facilitates the accurate capture of the flow fine features without unwanted blurriness. The method enables instantaneous measurements of the local velocity field to be made in regions of the orifice, where the cavitation topology exhibits extensive transient features. As made evident by Fig. 8.14b, point velocity measurements, in both low- and high-CN cases, were made possible in the regions of the flow field exhibiting high vapour presence standard deviation. It has to be emphasised that PTV does not require the addition of seeding particles in the flow that would possibly influence the cavitation formation in the orifice and it is therefore a preferable method for cavitating flows compared to Particle Image Velocimetry (PIV) (Mueller et al. 2013). Nevertheless, it must also be noted that filtering of a large number of raw radiographies is required to obtain an adequate dataset of point-velocity measurements, since only structures of small size that remain mainly unaltered during consecutive frames are deemed as suitable for velocimetry.

An extensive dataset of point-velocity measurements enables the calculation of local planar-velocity fluctuations, indicative of the in-nozzle level of turbulence. Figure 8.15 illustrates the fluctuations of axial velocity u_0 normalised by the average flow velocity. The average level of turbulence (denoted by the black line) is reduced as *CN* increases, although the Reynolds number increases as well, from 18,000 (Fig. 8.15a) to 35,500 (Fig. 8.15a). Hence, the presence of coherent, compressible vaporous structures seems to counteract the motion of small-scale vortices and has an overall stabilising effect on the flow field within the nozzle. A similar conclusion regarding the interaction of turbulence and cavitation has been reached through the numerical simulations reported in (Koukouvinis et al. 2017).

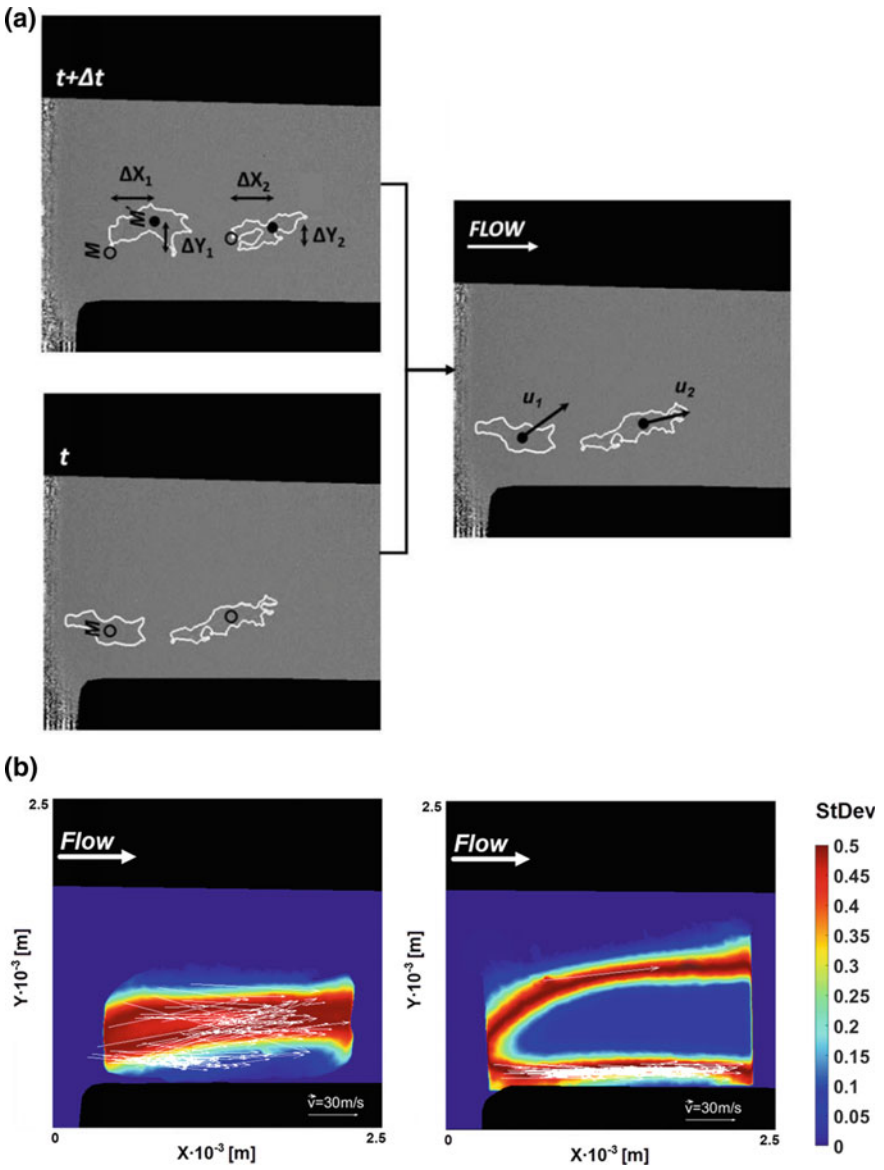

Fig. 8.14 **a** Concept of the PTV method: M and M' is the mass-centre of the identified structure over consecutive frames, with $\Delta t = 1/\text{frame-rate}$ (=67890). From the 16,000 raw images obtained at each location less than 1% was suitable for velocimetry. The maximum dimension of the structures that have been tracked is less than 700 μm and the mean deviation in their projected area over successive frames is ~8% (Karathanassis 2018). **b** Velocity vectors over standard deviation contour plots highlighting indicative locations at which estimates of the local velocity field have been obtained

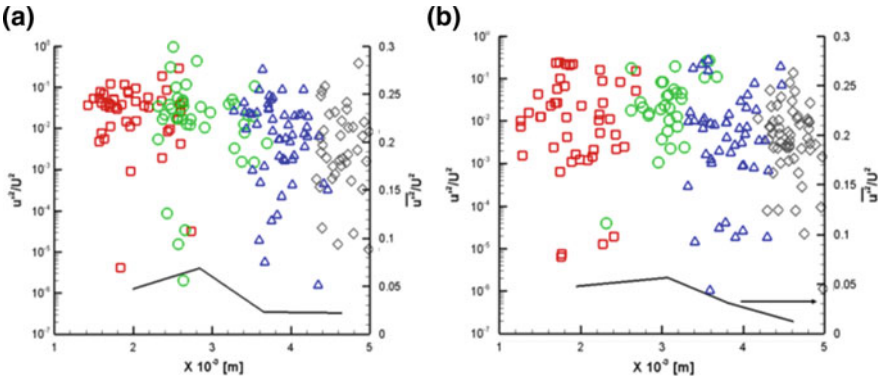

Fig. 8.15 Axial velocity fluctuations (Y ≈ 0.620 ± 0.04 mm based on the coordinates system shown in Fig. 8.14), **a** Re = 18000/CN = 3.2, **b** Re = 35500/CN = 7.7; (□) X = 1.0 mm, (○) X = 2.0 mm, (Δ) X = 3.0 mm, (◊) X = 4.0 mm (Karathanassis 2018)

8.2.3 X-Ray Computed Tomography (CT) Imaging

A shortcoming of optical high-speed imaging is the extensive light-beam scattering due to cavitation presence, which prevents the accurate and volumetric observation of the vaporous structures. Further to that point, the vast majority of optical methods are not capable of correlating the presence of cavitation to the local density of the flow. An alternative to such methods is the utilization of X-ray beams, as has been discussed in the previous paragraphs, which due to their much weaker interaction with matter penetrate the vaporous structures and carry accumulated interaction data through their line of sight. Consequently, their attenuation can be related to the integrated mixture composition along the beam path.

As has been already mentioned in the paragraph discussing XPCI, interaction of an X-ray beam with matter leads to both amplitude decrease and a phase shift of the irradiation wave, as reflected in the complex refractive index through the β and δ coefficients irradiation. Absorption imaging takes advantage especially of the x-ray wave amplitude attenuation and can be employed to derive the vapour mean-path length along the beam line of sight through the Beer-Lambert law (Duke et al. 2013):

$$I = I_0 e^{-\mu_l d}$$

where I and I_0 are the attenuated and initial beam intensity, μ_l is the liquid fuel attenuation coefficient and d is the material thickness. Hence, in order to derive the vapour mean path in a cavitating orifice, a normalisation experiment is also required under conditions where cavitation is absent to acquire a reference attenuated beam intensity considering that d is equal to the liquid path length. The characteristic thickness d in an irradiation event of a cavitating flow will be equal to the difference between the liquid and vapour path lengths.

Computed tomography (CT) imaging can be combined with x-ray imaging to collect radiographies of the attenuated x-ray beam from several angles. Reconstruction

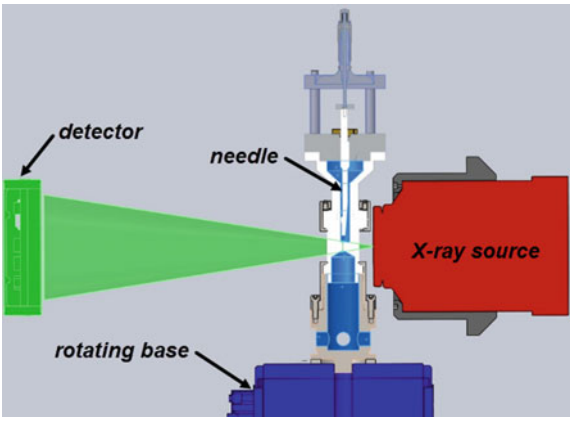

Fig. 8.16 The micro-CT facility employed in (Mitroglou et al. 2016). Projections were obtained at an angular step 0.6° (600 projections in total), with an acquisition time of 1 s per projection

of the obtained data, referred to as sinograms, can produce a 3D topology image of the irradiated sample. In the case of highly-transient cavitating flows, each projection is acquired over a time scale much larger than the manifestation of the flow phenomena and hence the reconstructed image represents the average vapour topology within the orifice. The first work utilizing X-ray CT for studying cavitation was in an enlarged orifice with a diameter of 1 cm, operating with water at pressures of ~0–2 bar (Bauer et al. 2012). The cavitating orifice was examined using a medical scanner, providing volumetric distributions of density inside the orifice. A more recent investigation has been performed at higher pressures (20–40 bar) employing an enlarged injector orifice with internal dimensions identical to the optical part depicted in Fig. 8.5, nevertheless fabricated by a PolyEther-Ether-Ketone (PEEK) plastic polymer (Mitroglou et al. 2016). The experiments were conducted at the prototype micro-CT facility available at the University of Bergamo consisting of a 160 kV @ 400 μA open type cone-beam X-ray source (Lorenzi et al. 2017). A schematic of the experimental layout comprising the x-ray source, irradiated specimen, scintillator plate and rotary base is illustrated in Fig. 8.16.

Figure 8.17 depicts contours plots of the average liquid fraction for different values of the needle lift. It is evident from the plots at the centre plane of the orifice (left panels of Fig. 8.17a and b) that a lower needle lift (0.5 mm instead of 1.0 mm) leads to the formation of a more extensive vapour pocket within the orifice, occupying the entire cross section, as illustrated by the front view also shown in Fig. 8.17a. The increased blockage ratio, as the needle lift decreases, leads to a more violent flow separation downstream the constriction, giving rise to a more pronounced cavity. It is interesting to notice in the front view of Fig. 8.17b that a 'halo' of vapour forms at the periphery of the nozzle yet vapour is absent in the upper part of the channel core. This distinctive cavitation behaviour underlines the shortcomings of optical methods, since visible light would be scattered even by this thin film (refer indicatively to Fig. 8.6) thus giving an overestimating impression of the vapour content in the region.

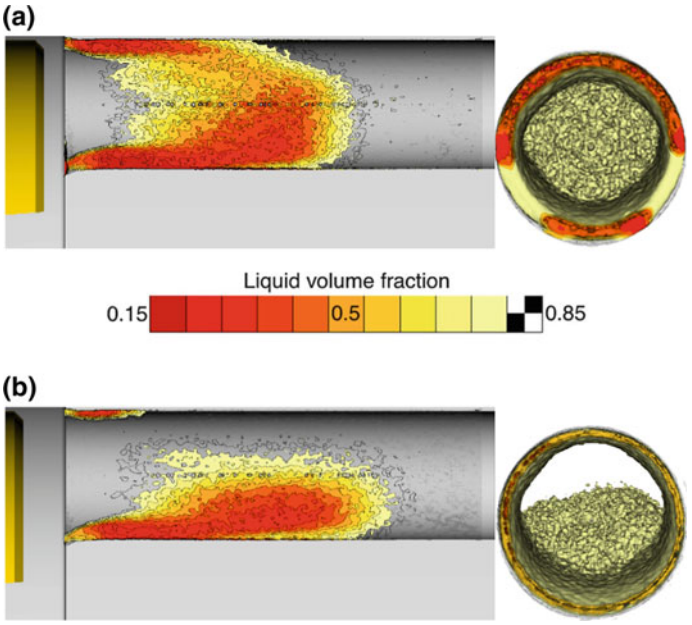

Fig. 8.17 Averaged liquid volume fraction contour plot for CN = 2.1: **a** needle lift of 0.5 mm, Re = 36500 and **b** needle lift of 1 mm, Re = 55500. Left-hand side panels correspond to side-view plots, while right-hand side panels to front-view plots, respectively. Flow is from left to right

8.3 Erosion

A well known ability of cavitation is its property to focus energy to small scales. Indeed, whereas large cavities (characteristic size of 1 mm) have a potential energy in the order of ~0.1–10 mJ, the mechanism of bubble collapse can lead to a concentration of this energy content to sub-micrometer scales, leading to energy density of more than 10 kJ/cm^3 enough to cause damage to metals (erosion). The process of erosion development is a complex topic, depending on material properties, such as its yield strength, ultimate strength or fatigue limit, and on flow mechanics aspects. An additional complexity is the temporal scale disparity between flow development, which may have a characteristic time scale of 10^{-3} s and the actual erosion development which can happen in the course of hours.

In general, the process of erosion is considered to be a work-hardening process and to occur in four successive stages. The first stage is the *incubation* stage, during which cavitation collapses introduce plastic deformation to the solid material, without exceeding the ultimate strength, thus there is no material removal. The next stage occurs once the ultimate strength is exceeded and the material can no longer sustain more plastic strain, hence material loss occurs; often this happens in an accelerating manner, thus it is termed *acceleration* stage. The next stage is the *steady state* stage where material removal rate remains constant over time and finally removal rate may

decrease in the *attenuation* stage. The aforementioned erosion procedure is found in any erosion-prone device; in injectors specifically even the start of material loss is undesired, since it may be associated with:

– strong reduction of performance (Som et al. 2010): alteration of the injector geometry due to erosion may lead to undesired effects on the jet direction and spray characteristics, thus increasing emissions.
– reliability issues: as material is removed from the injector body, stress concentration may occur. This is especially problematic with fuel injectors, as their operating conditions imply very high pressures, potentially leading to catastrophic failure of the injector tip.

  The multi-scale nature of cavitation and erosion renders the derivation of cavitation erosion models difficult and there are ongoing efforts for the formulation of generally applicable models. A well accepted scaling law (Franc and Michel 2005) is that mass loss is proportional to the n-th power of flow velocity, where n is case dependent and varies between 4 and 9. This demonstrates the significance of erosion nuisance in diesel systems, as flow velocity is in the order of several 100 m/s. Identified physical mechanisms of erosion can be separated in the following categories (van Terwisga et al. 2009; Leighton 1994):
– collapse of a single bubble: at the end of the collapse of a spherical bubble high temperatures and pressures have been detected, resulting to a high intensity pressure wave, with pressures levels of the order of 100 MPa.
– microjetting: the existence of pressure gradient around a bubble can lead to an asymmetrical collapse. In that case, part of the bubble collapses faster than the rest of the bubble, forming a characteristic jet with direction opposite to the pressure gradient. This jet may reach velocities up to several 100 m/s, producing water hammer pressures in the order of 1000 bar.
– collective bubble collapse: the collapse of a bubble within a bubble cloud triggers a cascade of implosions, which tends to enhance the collapse velocities of neighbouring bubbles and to increase the intensity and duration of the resulting pressure wave.
– cavitating vortices: such vortices appear in shear flows and at the rear of attached cavities. Cavitating vortices are considered to be the main cause of severe cavitation erosion in hydraulic machinery. Collapse velocities may be higher than 100 m/s and the duration of the stress time is rather long, comparing with the rest mechanisms.

Studies on cavitation erosion span from material science, concerning the resistance of various metals and alloys to cavitation (Franc et al. 2012), to combined studies coupling fluid dynamic observations with material pitting (Petkovšek and Dular 2013). In terms of erosion prediction many models rely on energy transfer mechanisms (Fortes Patella et al. 2013), micro-jet formation (Dular and Coutier-Delgosha 2009), work-hardening process etc. In more recent works (Schmidt et al. 2014; Mihatsch et al. 2015), erosion has been correlated to the localized flow pressure due to the collapse of cavitation structures and scaling laws have been derived to remove the dependency of collapse events from the numerical resolution.

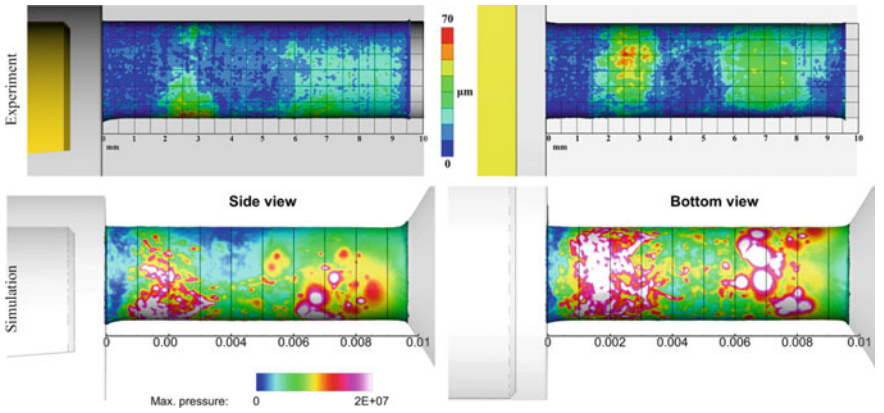

Fig. 8.18 Experimentally observed erosion (top) and numerically obtained locations of high pressures due to cavitation collapse (bottom). Erosion from experiments was obtained by the CT reconstruction of the orifice wall before and after exposure to cavitation. Progression of erosion is shown after a period of 44 h of operation. The orifice operation was at 55 bar (upstream) to 17.4 bar (downstream), CN = 2.2 and Re = 77000. Flow moves from left to right

When considering fuel systems, among the most pioneering works is the systematic investigation of square orifices tested in the Prevero project. In the frame of this project, the cavitation pattern and resulting erosion has been examined in sharp and rounded entrance square orifices operated at pressures of 100–300 bar, using diesel-like test oil (Skoda 2011). The orifices tested were made in a "sandwich" configuration, as a machined metal part placed between two sapphire windows. Depth averaged cavitation probability from high speed imaging and erosion over time were obtained and compared against simulations.

The LES study complemented by an X-ray CT investigation reported by Koukouvinis et al. (Koukouvinis et al. 2017) aimed at the development of validated cavitation models capable of replicating the density distribution and the erosion locations. Indicatively, in Fig. 8.18 the comparison between the experimentally obtained erosion and locations of high pressures from the simulations are shown, demonstrating a good agreement. An important observation of that study was the strong geometrical effects, especially at the orifice entrance, on the cavitating flow.

Moving towards more realistic configurations, relevant to diesel injectors, among the first works aiming to link cavitation and erosion (Gavaises 2008; Gavaises et al. 2007) relied on bubble dynamic sub-models relating damage to radiated acoustic pressure. Investigations based on pure Reynolds-Averaged-Navier-Stokes (RANS) turbulence closures performed in the past, showed situational applicability (Edelbauer et al. 2016; Koukouvinis et al. 2016). Since then, significant advances have been performed, by employing high resolution, compressible simulations capable of resolving large cavitation structures and turbulent scales. Notable contributions in the field involve investigations of rectangular orifices during injection to air or liquid

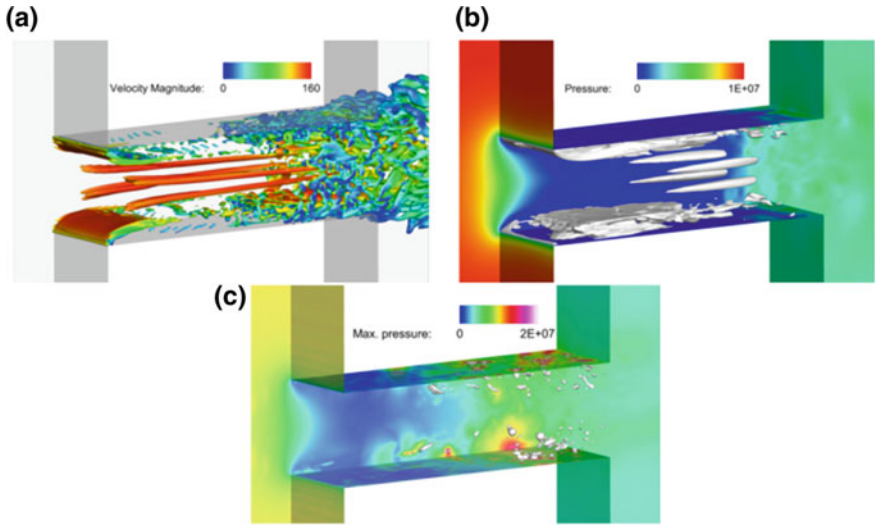

Fig. 8.19 Cavitating flow through a square orifice (cross sections 0.3 mm × 0.3 mm, length 1 mm) (Franc and Michel 2005), upstream pressure 100 bar, downstream pressure 40 bar (CN = 1.5, Re = 20000). **a** Instantaneous vortical structures, represented using the q-criterion (value 10^{12} $1/s^2$), coloured according to the velocity magnitude; four longitudinal vortex tubes are visible **b** Instantaneous pressure field (background) and cavitation clouds (grey iso-surface vapour volume fraction 50%); note the two cavitation types (attached cavities on the wall and vortex, or string, cavitation at the location of longitudinal vortices). **c** Pressure peaks due to the collapse of vapour structures; local maximum in the order of 1000 bar. The flow moves from left to right

(Egerer et al. 2014; Örley et al. 2017; Koukouvinis and Gavaises 2015) (an indicative illustration of the flow in such orifices is provided in Figs. 8.18, 8.19 and 8.20, derived using computational fluid dynamics and showing the prediction of vortical structures, their interaction with turbulence and the resulting pressure peaks leading to erosion).

Whereas studying flows in orifices can provide a better understanding of cavitation and erosion mechanisms, the operation of an actual diesel injector is definitely challenging, involving more complicated, moving geometry. Such investigations are limited due to the high complexity and computational cost. Indicatively, the first work (Örley et al. 2017) to examine computationally diesel injection to air, taking into account compressibility effects, cavitation formation, interaction with non-condensable gas and tracking locations of cavitation collapse required an immense computational cost, with meshes consisting of 35–80 million cells. With the current state of computers, such a simulation is prohibitive from an industrial point of view, due to the computational resources and time scales required. Investigations using simpler models (Koukouvinis et al. 2016) exploiting symmetry planes thus reducing the mesh count and computational cost have also been performed. While such models indeed have inherent limitations in terms of describing turbulence or capturing eccentric needle motion, are more tractable from an industrial perspective

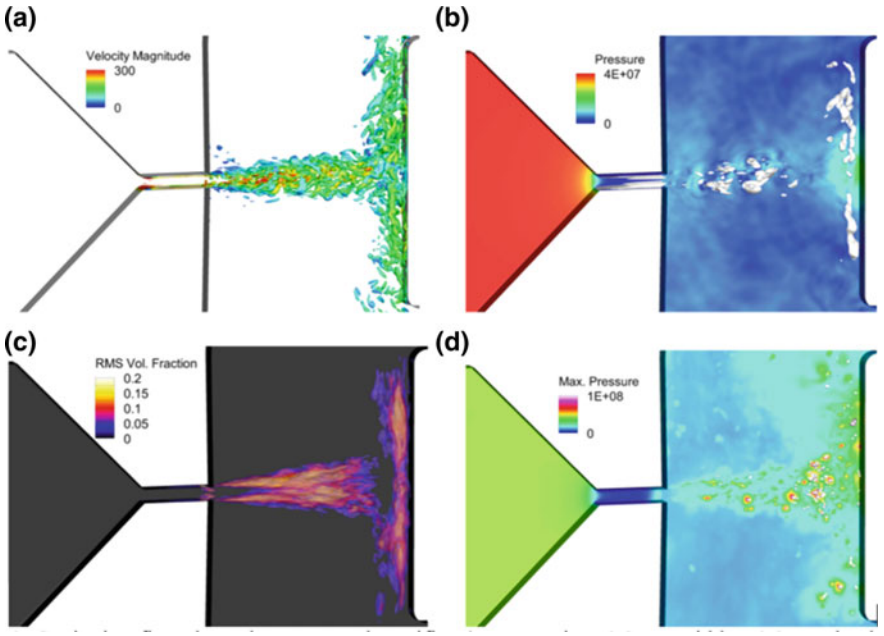

Fig. 8.20 Cavitating flow through a rectangular orifice (cross section: 0.2 mm width × 0.3 mm depth, length 1 mm) (Bauer et al. 2004), under supercavitating conditions; upstream pressure 400 bar downstream pressure 24 bar (CN = 15.6, Re = 40000). Here a target is placed at 2.95 mm from the orifice exit. **a** Instantaneous vortical structures, represented using the q-criterion (value 10^{12} $1/s^2$), coloured according to the velocity magnitude; note that within the orifice turbulence is suppressed due to the formation of stable cavities. Strong turbulence develops at the shear layer of the formed jet. **b** Instantaneous pressure field (background) and cavitation clouds (grey iso-surface vapour volume fraction 10%); cavitation at the shear layer is highly transient, **c** root-mean-square of vapour fraction fluctuation; areas of high fluctuations are regions of erosion **d** pressure peaks due to the collapse of vapour structures; local maximum in the order of 3000 bar

and have shown good replication of erosive patterns on affected injector designs (see Fig. 8.21).

The aforementioned discussion indicates that cavitation erosion effects can be predicted using numerical models. Erosion locations can be determined by tracking locations of cavitation collapse; moreover their erosive potential can be evaluated in terms of the emitted pressure magnitude. Whereas that magnitude itself is resolution dependent, scaling laws can be defined to predict actual material loss, though calibration is required. In general, erosion prediction necessitates refined models such as scale resolving simulations, which are inherently transient, though the computational cost is still tractable from an industrial perspective.

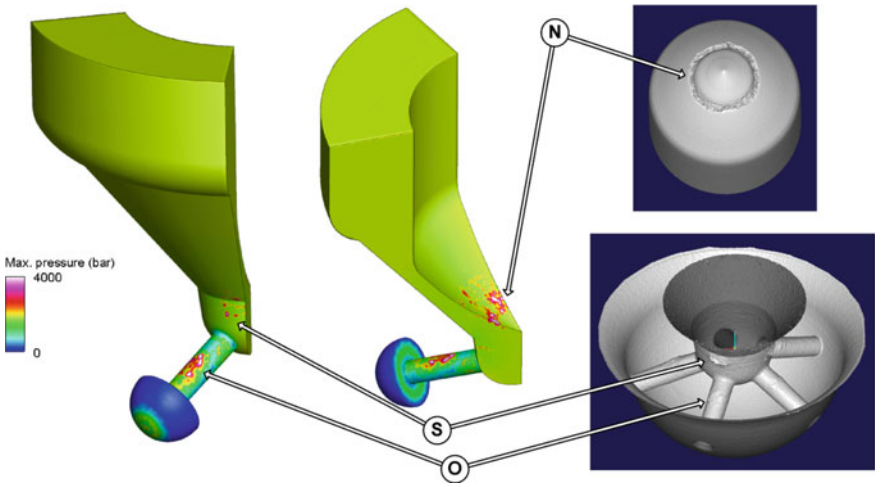

Fig. 8.21 Left: maximum pressures from cavitation collapse on the surfaces of a diesel injector obtained from simulation (Koukouvinis et al. 2016); note that in the simulation only 1/5th of the complete injector is simulated. Right: Indicative erosion patterns obtained from X-ray tomography of diesel injector. The letters in the cycles correspond to "O" for "orifice", "S" for "Sac" and "N" for "needle". The injector operates at a pressure difference of 1800 bar upstream and 50 bar downstream (CN ~ 35 and maximum Re ~ 90000)

8.4 Real-Fluid Thermodynamic Effects

An additional complexity especially relevant to modern engine operation is the large variations of pressures/temperatures that the fuel undergoes. Inarguably, the most extreme variations appear in modern diesel engines; the fuel may undergo pressure variations from effectively 0 bar in cavitating regions up to 2750 bar in the common rail (Egler et al. 2010), and temperatures variations from ambient, 298 K, up to 1000 K when exposed to the hot gases inside the cylinder. These variations imply considerable changes in the properties of diesel fuel, such as density and viscosity; indicatively dynamic viscosity may change up to 86% and density up to 15% (Kolev 2007), see Fig. 8.22.

Variation of properties poses additional challenges in the understanding of fuel systems. A notable effect is the temperature change induced by pressure changes. For incompressible fluids it is known that an ideal, adiabatic (isentropic) process implies constant temperature (Borgnakke and Sonntag 2008). This statement does not hold for real fluids, where pressure affects density and other thermodynamic properties. Indeed, ideal pressurization of a real-liquid in a diesel fuel pump can result to heating up to 20–30 K and fuel expansion during injection can result to localized temperature drop up to 50 K, depending on the discharge coefficient (Strotos et al. 2015), see Fig. 8.23. Similar effects appear in gasoline injection equipment as well, but are less pronounced due to lower pressure ratios in comparison to diesel systems.

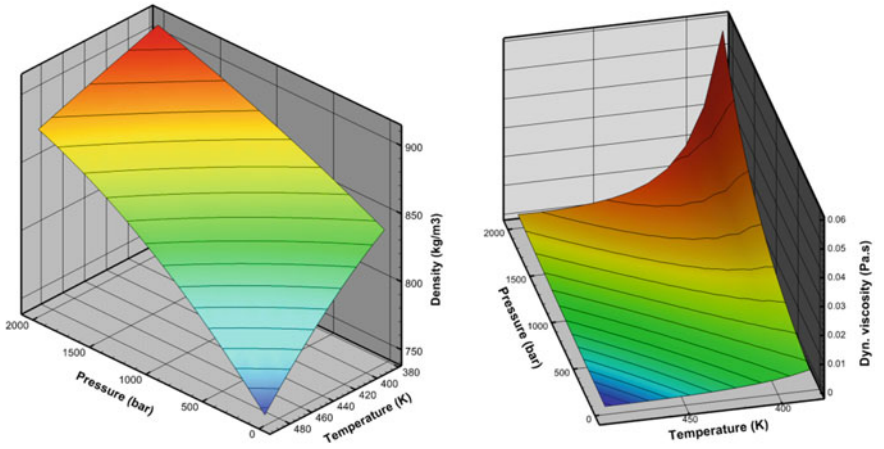

Fig. 8.22 Diesel property variation based on published data (Kolev 2007); density and dynamic viscosity for a range of pressures and temperatures

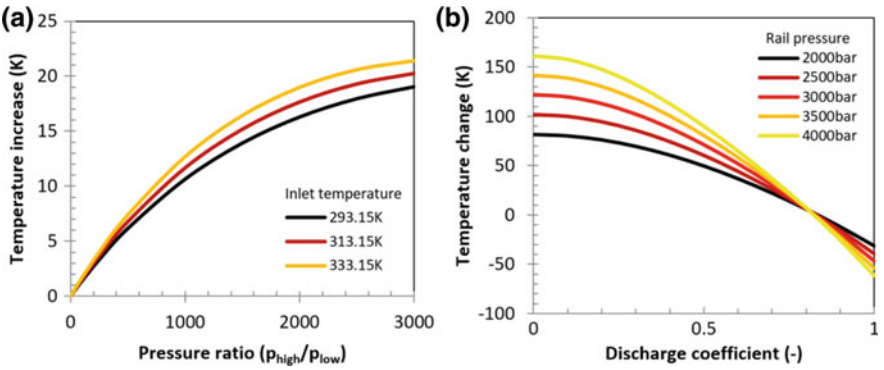

Fig. 8.23 **a** Temperature increase during isentropic diesel fuel compression in pump, for different pump inlet temperatures. Note that the temperature increase applies for ideal compression; actual, non-ideal compression will result to higher temperature increase. **b** Temperature change during fuel passage through a diesel injector, varying the discharge coefficient, c_d, assuming initial fuel temperature of 373 K and downstream pressure of 50 bar. Derivation of thermodynamic properties is based on published data (Kolev 2007)

It must be highlighted that fuel properties are not easy to define and measure, given the fact that fuels are blends of many different components. Also, fuel composition varies depending on the crude oil source and refinery processing. Hence, there has been increasing effort in measuring properties of fuel components and defining surrogates and models that can approximate the behaviour of actual fuels (Vidal et al. 2018). For defining adequate models for fuels and fuel components, it is necessary to describe phase change and transitions around the critical point (see indicatively

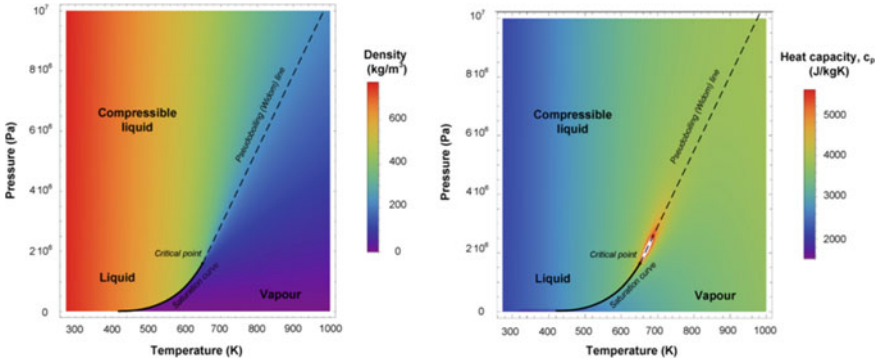

Fig. 8.24 Density (left) and heat capacity (right) variation for different p-T conditions for dodecane, according to NIST Refprop (Lemmon et al. 2018). Note the sharp transition of density along the saturation curve, the smooth variation of density beyond the critical point and the anomalies of heat capacity near the critical point

Fig. 8.24, for dodecane), beyond which there is no distinction between liquid and vapour phases and the latent heat of vaporization is zero.

Traditionally, models that are capable of describing such phenomena are cubic Equations of State (EoS), with perhaps the earliest example being the Van-der-Waals EoS (Borgnakke and Sonntag 2008). Nowadays this formulation has been superseded by more accurate variants, such as the Peng-Robinson or the Redlich-Kwong EoS (Borgnakke and Sonntag 2008), which can give an overall good representation of thermodynamic property variation, with minimum input (practically three parameters, critical temperature, critical pressure and acentric factor). A common shortcoming of such cubic models is the under-prediction of saturated liquid density and the over-prediction of liquid speed of sound. This deficiency of classical cubic EoS models can have an impact on the accurate prediction of mass flow rate for given pressure difference through an injector (Matheis and Hickel 2018). The recent years improvements have been made, capable of much more accurate predictions in relation to traditional cubic models, such as the generalized cubic EoS (Kim et al. 2012) and Perturbed Chain Statistical Association Fluid Theory (PC-SAFT) (Gross and Sadowski 2001) model, however these advanced models have not been explored yet widely in studies. Especially the PC-SAFT model is capable of describing the behaviour of mixtures with input based on the molecular structure of the components and their interaction parameters, to provide detailed and accurate predictions of thermodynamic and transport properties.

When moving towards the critical point, the mixing of fuel and surrounding gas departs from the classical atomization. At conditions below the critical point (subcritical) there is a clear distinction of liquid and gaseous phases and surface tension effects are observable (Crua et al. 2017). As temperature and pressure conditions move towards, or beyond, the critical point, surface tension effects diminish and there is no longer a clear interface between liquid and gas; instead turbulent mixing prevails (see Figs. 8.25 and 8.26). Such effects are especially relevant to diesel

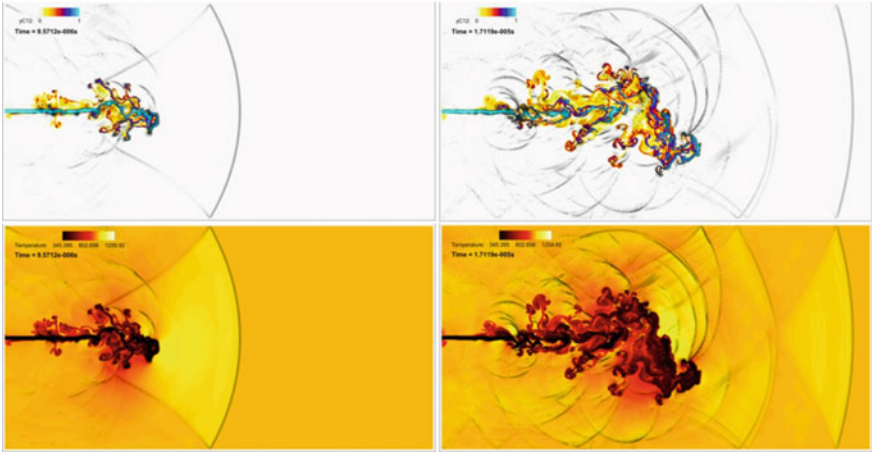

Fig. 8.25 Planar jet of dodecane (363 K, 600 m/s) to nitrogen (973K, 110bar); the jet has a width of 100 μm. Properties based on NIST Refprop (Lemmon et al. 2018). Top row shows mass fraction of dodecane, bottom row shows the temperature distribution. Black shades indicate the formed shock waves from the jet interaction with the stagnant air

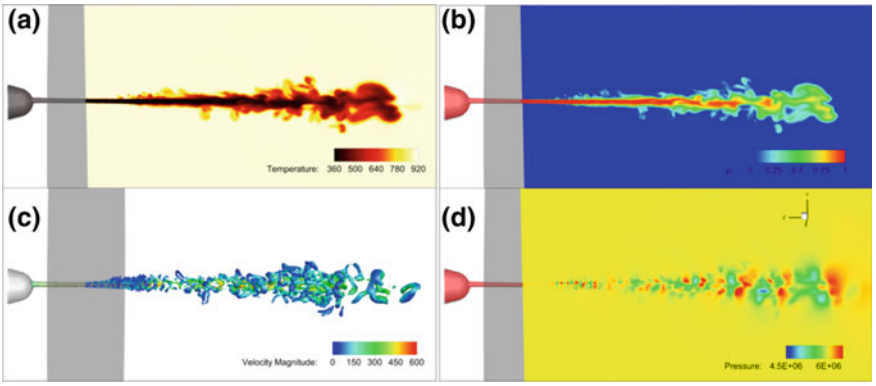

Fig. 8.26 Start-up of ECN Spray-A (non-reacting) configuration; dodecane injection to nitrogen (900 K, 60 bar). Injection mass flow rate based on the online tool available from ECN (http://www.cmt.upv.es/ECN03.aspx) for injection pressure of 1500 bar. Geometry based on published stereolithography (STL) surface. **a** temperature field **b** mass fraction of dodecane **c** pressure field, scaled to min/max at the external of the injector **d** turbulent structures (q-criterion value 10^{12} s^{-2}), coloured according to velocity magnitude. Time 30 μs. Properties based on NIST Refprop (Lemmon et al. 2018)

Table 8.1 Critical point properties for indicative fuel/fuel-surrogate components (Anitescu et al. 2012)

	Components	T_c (K)	P_c (bar)
Gasoline	Hexane	507.82	30.34
	Heptane	540.13	27.36
	Iso-octane	544	25.72
Diesel	Dodecane	658.1	18.17
	Hexadecane	722.1	14.799
	Docosane	792.2	11.74

injection (Dahms and Oefelein 2013); this can be understood when considering the critical point properties of common hydrocarbons (see Table 8.1), that are components of gasoline and diesel. The trend indicates that as the number of carbon atoms increase in the hydrocarbon molecule, the critical temperature increases and the critical pressure decreases. Considering that gasoline injection happens at relatively low pressure and temperature conditions, the operation regime is more towards classical atomization at subcritical conditions. On the other hand, diesel injection occurs at much higher cylinder conditions, at pressures/temperatures well above the critical point of diesel fuel components.

It is highlighted that the aforementioned discussion is a rough approximation, given that it is only applicable to single, pure components. Indeed, mixing of different components, such as diesel and nitrogen, alters the critical conditions of the mixture, so that liquid and vapour can exist even if local pressure/temperature conditions exceed the critical conditions of the pure components involved in the mixing. Figure 8.27 illustrates this effect, showing the pressure-composition lines of nitrogen/dodecane at different temperatures.

Apart from the complex thermodynamic effects taking place, the flow of fuel and its interaction with gases in the cylinder, also poses complexities. The progressive break-up of fuel to smaller scales, finally vaporizing and mixing with the surrounding air, termed as atomization (Tryggvason et al. 2011), is a multi-scale process, strongly affected by turbulence and surface tension. Different levels of approximation are commonly employed depending on the level of accuracy and the computational cost that can be afforded, ranging from interface capturing (Ghiji et al. 2016) (Volume of Fluid or Level-Set) in primary atomization and Eulerian-Eulerian (Vujanović et al. 2015) or Eulerian-Lagrangian (Anez et al. 2019) models for secondary atomization, or dense-fluid (Müller et al. 2016) spray models for supercritical/transcritical regimes.

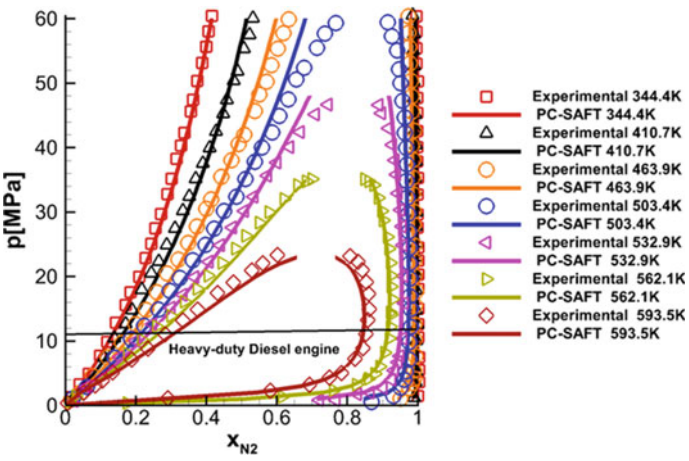

Fig. 8.27 Liquid/vapour saturation lines for different molar compositions of nitrogen/dodecane mixture; comparison between experiments (García-Córdova et al. 2011) and PC-SAFT model predictions (Rodriguez et al. 2018); note that the mixture critical pressure is well above the critical pressure of the individual pure components

8.5 Conclusions

The aforementioned discussion aims to provide a brief overview of multiphase flow phenomena that occur in modern fuel injection systems, with main emphasis in Diesel applications, since those pose the most extreme conditions. Indeed, despite their relative small scale compared to more traditional applications of fluid dynamics (e.g. external aerodynamics), a wealth of phenomena appear combining complex aspects of physics of fluids, such as turbulence, phase transition/vaporization and interfacial flows.

Concerning experimental methods, perhaps one of the most promising and recent developments is the investigation of flow using X-rays. The use of X-rays allows to avoid common drawbacks of optical methods, such as optical scattering at fluid interfaces. Further developments of the method involve temporally resolved densitometry, which can provide quantitative information on transient multiphase flows.

Concerning computational techniques, the advancement of computing power has allowed to incorporation of more elaborate and detailed information to be captured in multiphase, cavitating flows, or flows of sprays and fuel jets, offering unprecedented resolution of turbulence and interfacial dynamics. Unfortunately, the computational cost of such investigations is quite prohibitive from a general perspective, requiring thousands CPU-hours of computing power and often necessitating High Performance Computing (HPC).

References

Andriotis A, Gavaises M (2009) Influence of vortex flow and cavitation on near-nozzle diesel spray dispersion angle. At Sprays 19:247–261

Andriotis A, Gavaises M, Arcoumanis C (2008) Vortex flow and cavitation in diesel injector nozzles. J Fluid Mech 610:195–215

Anez J et al (2019) Eulerian-Lagrangian spray atomization model coupled with interface capturing method for diesel injectors. Int J Multiph Flow 113:325–342

Anitescu G, Bruno TJ, Tavlarides LL (2012) Dieseline for supercritical injection and combustion in compression-ignition engines: volatility, phase transitions, spray/jet structure, and thermal stability. Energy Fuels 26:6247–6258

Arcoumanis C, Gavaises M, Flora H, Roth H (2001) Visualisation of cavitation in diesel engine injectors. Mec Ind 2:375–381

Arndt REA (2002) Cavitation in vortical flows. Annu Rev Fluid Mech 34:143–175

Bardi M et al (2013) Engine combustion network: comparison of spray development, vaporization, and combustion in different combustion vessels. At Sprays 22:807–842

Bauer W, Iben U, Voss M (2004) Simulation of cavitating flow in injection systems. In: Numerical analysis and simulation in vehicle engineering, VDI Berichte, vol 1846

Bauer D, Chaves H, Arcoumanis C (2012) Measurements of void fraction distribution in cavitating pipe flow using x-ray CT. Meas Sci Technol 23:055302

Borgnakke C, Sonntag R (2008) Fundamentals of thermodynamics. Wiley

Crua C, Manin J, Pickett LM (2017) On the transcritical mixing of fuels at diesel engine conditions. Fuel 208:535–548

Dahms RN, Oefelein JC (2013) On the transition between two-phase and single-phase interface dynamics in multicomponent fluids at supercritical pressures. Phys Fluids 25:92103

Dimitropoulos CD, Sureshkumar R, Beris AN (1998) Direct numerical simulation of viscoelastic turbulent channel flow exhibiting drag reduction: effect of the variation of rheological parameters. J Nonnewton Fluid Mech 79:433–468

Dreiss CA (2007) Wormlike micelles: where do we stand? Recent developments, linear rheology and scattering techniques. Soft Matter 3:956

Duke DJ, Kastengren AL, Tilocco FZ, Swantek AB, Powell CF (2013) X-ray radiography measurements of cavitating nozzle flow. At Sprays 23:841–860

Dular M, Coutier-Delgosha O (2009) Numerical modelling of cavitation erosion. Int J Numer Methods Fluids 61:1388–1410

Edelbauer W, Strucl J, Morozov A (2016) Large eddy simulation of cavitating throttle flow: SIMHYDRO 2014. In: Gourbesville P, Cunge JA, Caignaert G (eds) Advances in hydroinformatics, Part III. Springer, Singapore, pp 501–517. https://doi.org/10.1007/978-981-287-615-7_34

Egerer CP, Hickel S, Schmidt SJ, Adams NA (2014) Large-eddy simulation of turbulent cavitating flow in a micro channel. Phys Fluids 26:085102

Egler W et al (2010) Fuel injection systems. In: Mollenhauer K, Tschöke H (eds) Handbook of diesel engines. Springer, Berlin, Heidelberg. https://link.springer.com/chapter/10.1007/978-3-540-89083-6_5

Fortes Patella R, Choffat T, Reboud J-L, Archer A (2013) Mass loss simulation in cavitation erosion: fatigue criterion approach. Wear. https://doi.org/10.1016/j.wear.2013.01.118

Franc JP, Michel J (2005) Fundamentals of cavitation. Kluwer Publishing

Franc J-P, Riondet M, Karimi A, Chahine GL (2012) Material and velocity effects on cavitation erosion pitting. Wear 274–275:248–259

Ganesh H, Mäkiharju SA, Ceccio SL (2016) Bubbly shock propagation as a mechanism for sheet-to-cloud transition of partial cavities. J Fluid Mech 802:37–78

García-Córdova T, Justo-García DN, García-Flores BE, García-Sánchez F (2011) Vapor−liquid equilibrium data for the nitrogen + dodecane system at temperatures from (344 to 593) K and at pressures up to 60 MPa. J Chem Eng Data 56:1555–1564

Gavaises M (2008) Flow in VCO nozzles with cylindrical and tapered holes and link to cavitation erosion and engine exhaust emissions. Int J Engine Res 9:435–447
Gavaises M, Papoulias D, Andriotis A, Giannadakis E, Theodorakakos A (2007) Link between cavitation development and erosion damage in Diesel fuel injector nozzles. In: SAE world congress & exhibition
Gavaises M, Andriotis A, Papoulias D, Mitroglou N, Theodorakakos A (2009) Characterization of string cavitation in large-scale Diesel nozzles with tapered holes. Phys Fluids 21:052107
Ghiji M, Goldsworthy L, Brandner PA, Garaniya V, Hield P (2016) Numerical and experimental investigation of early stage diesel sprays. Fuel 175:274–286
Gopalan S, Katz J (2000) Flow structure and modeling issues in the closure region of attached cavitation. Phys Fluids 12:895
Gross J, Sadowski G (2001) Perturbed-chain SAFT: an equation of state based on a perturbation theory for chain molecules. Ind Eng Chem Res 40:1244–1260
Im K-S, Cheong S-K, Powell CF, Lai MD, Wang J (2013) Unraveling the geometry dependence of in-nozzle cavitation in high-pressure injectors. Sci Rep 3:3–7
Karathanassis IK et al (2018) High-speed visualization of vortical cavitation using synchrotron radiation. J Fluid Mech 838
Karathanassis IK et al (2018) Illustrating the effect of viscoelastic additives on cavitation and turbulence with X-ray imaging. Sci Rep 8:1–15
Kim S-K, Choi H-S, Kim Y (2012) Thermodynamic modeling based on a generalized cubic equation of state for kerosene/LOx rocket combustion. Combust Flame 159:1351–1365
Kitagawa A, Hishida K, Kodama Y (2005) Flow structure of microbubble-laden turbulent channel flow measured by PIV combined with the shadow image technique. Exp Fluids 38:466–475
Kolev N (2007) Multiphase flow dynamics 3. Springer, Berlin, Heidelberg. https://doi.org/10.1007/978-3-540-71443-9
Koukouvinis P, Gavaises M (2015) Simulation of throttle flow with two phase and single phase homogenous equilibrium model. J Phys Conf Ser 656:12086
Koukouvinis P, Naseri H, Gavaises M (2016) Performance of turbulence and cavitation models in prediction of incipient and developed cavitation. Int J Engine Res
Koukouvinis P, Gavaises M, Li J, Wang L (2016b) Large eddy simulation of diesel injector including cavitation effects and correlation to erosion damage. Fuel 175:26–39. https://doi.org/10.1016/j.fuel.2016.02.037
Koukouvinis P, Mitroglou N, Gavaises M, Lorenzi M, Santini M (2017) Quantitative predictions of cavitation presence and erosion-prone locations in a high-pressure cavitation test rig. J Fluid Mech 819:21–57
Leighton TG (1994) The acoustic bubble. Academic Press
Lemmon EW, Bell IH, Huber ML, McLinden MO (2018) NIST Standard Reference Database 23: Reference Fluid Thermodynamic and Transport Properties-REFPROP. Natl Inst Stand Technol Stand Ref Data Progr. https://doi.org/10.18434/t4js3c
Linne M (2012) Analysis of X-ray phase contrast imaging in atomizing sprays. Exp Fluids 52:1201–1218
Lorenzi M, Mitroglou N, Santini M, Gavaises M (2017) Novel experimental technique for 3D investigation of high-speed cavitating diesel fuel flows by X-ray micro computed tomography. Rev Sci Instrum 88
Matheis J, Hickel S (2018) Multi-component vapor-liquid equilibrium model for LES of high-pressure fuel injection and application to ECN Spray A. Int J Multiph Flow 99:294–311
Mihatsch MS, Schmidt SJ, Adams NA (2015) Cavitation erosion prediction based on analysis of flow dynamics and impact load spectra. Phys Fluids 27
Mitra P et al (2019) Identification and characterization of steady spray conditions in convergent, single-hole diesel injectors. SAE Tech Pap Ser 1:1–17
Mitroglou N, McLorn M, Gavaises M, Soteriou C, Winterbourne M (2014) Instantaneous and ensemble average cavitation structures in Diesel micro-channel flow orifices. Fuel 116:736–742
Mitroglou N, Lorenzi M, Santini M, Gavaises M (2016) Application of X-ray micro-computed tomography on high-speed cavitating diesel fuel flows. Exp Fluids 57
Mitroglou N, Stamboliyski V, Karathanassis IK, Nikas KS, Gavaises M (2017) Cloud cavitation vortex shedding inside an injector nozzle. Exp Therm Fluid Sci 84

Mueller A, Dreyer M, Andreini N, Avellan F (2013) Draft tube discharge fluctuation during self-sustained pressure surge: fluorescent particle image velocimetry in two-phase flow. Exp Fluids 54

Müller H, Niedermeier CA, Matheis J, Pfitzner M, Hickel S (2016) Large-eddy simulation of nitrogen injection at trans- and supercritical conditions. Phys Fluids 28:15102

Naseri H et al (2018) Turbulence and cavitation suppression by quaternary ammonium salt additives. Sci Rep: 1–15. https://doi.org/10.1038/s41598-018-25980-x

Naseri H, Koukouvinis P, Malgarinos I, Gavaises M (2018) On viscoelastic cavitating flows: a numerical study. Phys Fluids 30:033102

Örley F, Hickel S, Schmidt SJ, Adams NA (2017) Large-eddy simulation of turbulent, cavitating fuel flow inside a 9-hole diesel injector including needle movement. Int J Engine Res 18(3):195–211. https://doi.org/10.1177/1468087416643901

Pereira AS, Mompean G, Thais L, Soares EJ (2017) Transient aspects of drag reducing plane Couette flows. J Nonnewton Fluid Mech 241:60–69

Petkovšek M, Dular M (2013) Simultaneous observation of cavitation structures and cavitation erosion. Wear 300:55–64

Pickett LM, Kook S, Williams TC (2009) Visualization of diesel spray penetration, cool-flame, ignition, high-temperature combustion, and soot formation using high-speed imaging. SAE Int J Engines 2:439–459

Reid BA et al (2014) On the formation of string cavitation inside fuel injectors. Exp Fluids 55:1–8

Reid BA, Hargrave GK, Garner CP, Wigley G (2010) An investigation of string cavitation in a true-scale fuel injector flow geometry at high pressure. Phys Fluids 22:1–3

Rodriguez C, Vidal A, Koukouvinis P, Gavaises M, Mchugh MA (2018) Simulation of transcritical fluid jets using the PC-SAFT EoS. J Comput Phys 374:444–468

Russo P (2014) Physical basis of x-ray imaging. In: Comprehensive biomedical physics. Elsevier B.V. https://doi.org/10.1016/b978-0-444-53632-7.00201-x

Sathe MJ, Thaker IH, Strand TE, Joshi JB (2010) Advanced PIV/LIF and shadowgraphy system to visualize flow structure in two-phase bubbly flows. Chem Eng Sci 65:2431–2442

Schmidt SJ, Mihatsch MS, Thalhamer M, Adams NA (2014) Assessment of erosion sensitive areas via compressible simulation of unsteady cavitating flows. In: Kim K-H, Chahine G, Franc J-P, Karimi A (eds) Advanced experimental and numerical techniques for cavitation erosion prediction. Springer, Netherlands, pp 329–344. https://doi.org/10.1007/978-94-017-8539-6_14

Skoda R et al (2011) Numerical simulation of collapse induced shock dynamics for the prediction of the geometry, pressure and temperature impact on the cavitation erosion in micro channels. In: WIMRC 3rd international cavitation forum 2011. https://doi.org/10.13140/2.1.2676.9287

Som S, Aggarwal SK, El-Hannouny EM, Longman DE (2010) Investigation of nozzle flow and cavitation characteristics in a diesel injector. J Eng Gas Turbines Power 132:42802–42812

Strotos G, Koukouvinis P, Theodorakakos A, Gavaises M, Bergeles G (2015) Transient heating effects in high pressure diesel injector nozzles. Int J Heat Fluid Flow 51:257–267

Stutz B, Legoupil S (2003) X-ray measurements within unsteady cavitation. Exp Fluids 35:130–138

Tryggvason G, Scardovelli R, Zaleski S (2011) Direct numerical simulations of gas–liquid multi-phase flows. Cambridge University Press

Tsukahara T, Motozawa M, Tsurumi D, Kawaguchi Y (2013) PIV and DNS analyses of viscoelastic turbulent flows behind a rectangular orifice. Int J Heat Fluid Flow 41:66–79

van Terwisga TJC, Fitzisimmons PA, Li ZR (2009) Cavitation erosion—a review of physical mechanisms and erosion risk models. In: 7th international symposium on cavitation

Vidal A, Rodriguez C, Koukouvinis P, Gavaises M, McHugh MA (2018) Modelling of diesel fuel properties through its surrogates using Perturbed-Chain, Statistical Associating Fluid Theory. Int J Engine Res: 146808741880171. https://doi.org/10.1177/1468087418801712

Vujanović M, Petranović Z, Edelbauer W, Baleta J, Duić N (2015) Numerical modelling of diesel spray using the Eulerian multiphase approach. Energy Convers Manag 104:160–169

Westlye FR et al (2017) Diffuse back-illumination setup for high temporally resolved extinction imaging. Appl Opt 56:5028

Part IV
Miscellaneous

Chapter 9
Improvement of Flame Kernel Growth by Microwave-Assisted Plasma Ignition

Joonsik Hwang, Wooyeong Kim and Choongsik Bae

Abstract Due to the depletion of petroleum resources and environmental concerns, automobile industry has been developing new engine technologies with acceptable cost range to consumers. Among many new technologies, application of non-thermal plasma ignition system is considered as a promising path to achieve high-efficiency clean gasoline vehicles. In this study, we developed a microwave-assisted plasma ignition using 3 kW, 2.45 GHz magnetron with customized electric components and ignitor. This system was tested in a constant volume combustion vessel to investigate the effects of microwave ejection on ignition kernel growth. High-speed shadowgraph imaging and hydroxyl (OH) radical imaging were carried out under various air-fuel ratio, ambient pressure, and ignition strategy conditions. The in-cylinder pressure measurement was also performed to compare combustion phase between conventional spark and microwave-assisted plasma ignition system. The experimental result showed that the microwave ejection on the thermal plasma created by conventional discharge had a significant improvement on initial flame development. The microwave-assisted plasma ignition system indicated advanced combustion phase with extended lean limit where conventional spark ignition failed to achieve flame propagation. The OH imaging on propagating flame presented much higher intensity with microwave-assisted plasma ignition case. The analysis on light emission spectrum showed 7,000 K higher electron temperature in the plasma created with microwave ejection. This implies that chemical reactions which could not be progressed with conventional spark ignition was enabled with additional non-thermal plasma induced by electro-magnetic wave. On the other hand, however, the enhancement in flame development was decreased under high pressure condition due to lower reduced electric field.

Keywords Microwave · Non-thermal plasma · Constant volume combustion vessel · Flame kernel · Ignition

J. Hwang · W. Kim · C. Bae (✉)
Department of Mechanical Engineering, Korea Advanced Institute of Science and Technology (KAIST), 291 Daehak-ro, Daejeon, Republic of Korea
e-mail: csbae@kaist.ac.kr

A. P. Singh et al. (eds.), *Simulations and Optical Diagnostics for Internal Combustion Engines*, Energy, Environment, and Sustainability,
https://doi.org/10.1007/978-981-15-0335-1_9

9.1 Introduction

Continuously growing environmental concerns and stringent regulations on fuel economy are driving automobile industry to develop high-efficiency clean vehicles. Spark-ignition engines are known to have greater controllability in terms of combustion phase than compression-ignition engines. However, knocking under advanced ignition timing or higher compression conditions has limited its potential. In response, automobile industry has been adopting gasoline direct injection (GDI) engines. GDI engines are different from conventional port fuel injection (PFI) engines in fuel-air mixing process. GDI engines inject the fuel directly into the combustion chamber so knocking could be mitigated by charge cooling effect during fuel evaporation. Many other advanced engine technologies such as high pressure injection, exhaust gas recirculation (EGR), and multiple injection have been employed to achieve lean burn in GDI engines (Szwaja et al. 2013; Wei et al. 2013; Tang et al. 2015; Oh and Bae 2013). However, improvement in combustion and emission characteristics with those technologies has turned out as minor level. Completely new approaches using new ignition system or combustion concept are required to achieve the required rate of innovation at this moment. Among many new technologies, plasma-assisted combustion has shown great promise for combustion enhancement (Shiraishi and Urushihara 2011; Hampe et al. 2013; Genzale et al. 2011; DeFilippo et al. 2011; Wang et al. 2015; Starikovskii 2005; Starilovskaia 2006). Ignition concepts utilizing thermal plasma as well as non-thermal plasma have been considered as an alternative for conventional spark ignition system. The thermal plasma ignition originated more than one hundred years ago with internal combustion engines and spark ignition systems. However, corrosion and erosion problems are inevitable because of higher charge temperature and thermal quenching to electrodes. Thus in these days, many research facilities are paying attention in application of non-thermal plasma for ignition and combustion. It provides new possibilities for ignition and flame stabilization in more efficient way than thermal plasma system (Fridman 2008).

A number of researchers have examined the potential of microwave ejection on flame enhancement (Wang et al. 2015; Wolk et al. 2013; Luo et al. 2019). Electromagnetic wave from magnetron can heat up free electrons in the discharge stream or flame surface. Two main mechanisms of flame enhancement depending on the wave frequency of applied electro-magnetic wave have been discussed. At first, direct momentum transfers by relatively big ions called ionic wind can promote chemical reactions by low frequency electro-magnetic wave. Ionic wind and ion drift according to the wave frequency could dramatically alter pathways in terms of chemical reactions and be used for soot emission control. Meanwhile, flame coupling was through the collision of free electrons with neutrals under the high frequency regime. The effect of alternating electric field with high frequency has been studied by a number of groups. The measurements showed global increases in flame speed, flame temperatures, and corresponding enhancement in concentrations such as hydroxyl radical. Despite many efforts of previous studies, the effects of microwave ejection

under engine-like condition has not been investigated. The measurements have been carried out relatively low pressure under uncontrolled ambient condition. In this study, microwave-assisted plasma ignition system was applied in a constant volume combustion vessel. The effect of microwave ejection on flame kernel will be discussed based on experimental investigations.

9.2 Experimental Setup

9.2.1 Constant Volume Combustion Chamber System

For a series of combustion test, a vessel which has a volume of 1.4 l was utilized. The combustion vessel was fabricated with carbon steel to withstand maximum in-chamber pressure and temperature of 15 MPa and 2,000 K, respectively. A schematic diagram of the vessel system is presented in Fig. 9.1. The chamber has 6 ports so either quartz window or metal dummy window can be installed according to experimental setup. In this study three quartz windows with a diameter of 9.6 cm were places in two parallel sides for shadowgraph imaging and in the front side for OH radical imaging. In both side windows, only the region of a square (3 cm by 3 cm) around the igniter was uncovered by aluminum plates to minimize microwave leakage to outside of the chamber. As shown in the schematic, premixed mixture of Acetylene (C_2H_2) and air was delivered to the vessel through the intake valve. The equivalence ratio of prepared mixture was calculated using partial pressures of each gas with uncertainty range of

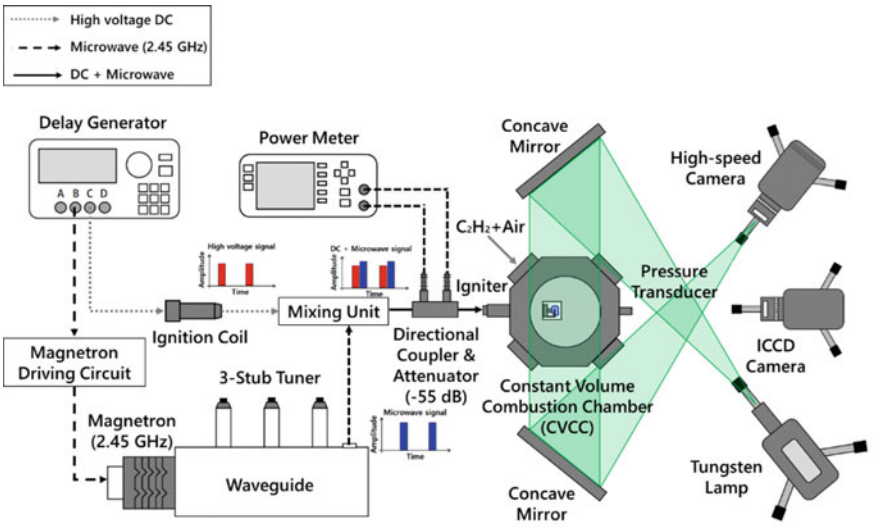

Fig. 9.1 Schematic diagram of experimental setup

$\pm 10^{-4}$ MPa. The initial ambient pressure was also controlled by adjusting the initial mixture quantity. Then, the combustible mixture was ignited by the conventional ignition system and the microwave-assisted plasma ignition system. The pressure rise in the chamber after the ignition was monitored using a piezo-electric pressure transducer (Kistler, 6141B) and a charge amplifier (Kistler, 5011) with a resolution of 50 kHz. At the same time, the ignition process was visualized by a high-speed camera and intensified camera. A tungsten lamp, pin hole, and two identical concave mirrors were utilized for the high-speed shadowgraph imaging. A high-speed digital video camera (MIRO, M 110) equipped with a zoom lens (Nikkor, 80–200 mm f/2.8D) was employed to ignition event and early flame development in the vessel. An electric trigger for the ignition system was also used to trigger the high speed camera for recording. The high-speed camera was set to have a shutter speed of 38,000 frames per second (fps) with image resolution of 192 by 192. The aperture of lens and the exposure time of the high-speed camera were set to 2.8 and 2 μs respectively. This setting was kept through entire experiment. An in-house Matlab code was utilized for flame kernel size measurement. The OH radicals on the flame surface captured utilizing a 310 nm band pass filter (Edmund Optics, 67886 (V097-25)) and intensified charge coupled device (CCD) camera (Princeton Instruments, PI-MAX2) in the front side.

9.2.2 Microwave-Assisted Plasma Ignition System

For a microwave source, 3.0 kW, 2.45 GHz magnetron (National, NL 10250-1) was used. The magnetron was triggered by an insulated gate bipolar transistor (IGBT) which delivered 5 kV. The 100% of duty cycle for the magnetron was utilized by on/off power control. The generated microwave was delivered through a waveguide which has a dimension of 72 mm by 34 mm cross section. The energy loss of microwave was minimized by keeping all the propagating wave in the waveguide. This waveguide was designed to have transverse electric 010 (TE_{010}) mode thus the peak power was occurring in the centerline of the waveguide. The TE_{010} mode is known as the simplest mode in a cavity which has symmetrical electric field distribution along the propagating direction. Impedance matching was performed by 3-stub tuners (ASTeX, AX3041) installed in the middle of the waveguide to minimize power reflection in the waveguide. An antenna was installed at about 30 mm ($\lambda_{microwave}/4$) from the end of the waveguide wall to extract the microwave energy from the waveguide. A N-type coaxial cable was selected as a transmission line which connects waveguide to mixing unit and mixing unit to igniter. In the mixing unit, direct current (DC) voltage and microwave were mixed and transferred to the igniter. The microwave-assisted plasma ignition concept uses not only conventional spark discharge but also microwave ejection so the mixing unit was necessary. The mixing unit was composed of a coil which blocks microwave and a capacitor which minimize the interference caused by DC. The mixing unit was manufactured as a type of micro-strip circuit. It has a dimensions of 50 mm (width) by 75 mm

(length) by 1 mm (height). Measurement of transmitting microwave power was performed using a directional coupler and a power meter (Agilent, E4417A). These units were installed between the mixer and the igniter to measure the forwarded and reflected microwave power. It is known that the absorption of electromagnetic energy by a material is depending on their dielectric properties (Thostenson and Chou 1999). Thus, microwave power on the combustion system was calculated by considering reflected power and forwarded power. Two identical attenuators with −55 dB were installed in the directional coupler to protect the power meter from excessive microwave power that could damage the device. Internal resistor in the spark plug block most of the microwave thus non-resistor spark plug was designed and manufactured. The N-type connector was placed at the end of ignitor so it can be connected with mixing unit directly. The high DC was delivered through the central electrode in the ignitor whereas the microwave was transferred through a space in the electrode shell.

9.2.3 Experimental Conditions

The combustion test conditions are summarized in Table 9.1. The equivalence ratio and initial in-chamber pressure were varied from 0.4 to 1.6 and 0.1 Mpa to 0.7 MPa, respectively. Again, the mixture composition and initial pressure were set by controlling partial pressure of C_2H_2 and Air. The chamber was not heated by external heating source but kept at room temperature around 300 K. Electric durations of 2 and 2.5 ms were used for microwave ejection and coil charging time. The corresponding spark and microwave energies were 135 and 125 mJ per event. The microwave ejection timing was changed between 500 μs before and after the spark event to investigate the effect of microwave ejection timing on combustion. An ensemble averaged combustion results from five different ignition cases were compared between the conventional spark ignition system and the microwave-assisted plasma ignition system. An error analysis on in-chamber pressure analysis showed ±0.09 MPa range in

Table 9.1 Test conditions

Item	Level
Equivalence ratio	0.4–1.6
In-chamber pressure (MPa)	0.1–0.7
In-chamber temperature (K)	300
Spark energizing time (ms)	2
Applied microwave duration (ms)	2.5
Microwave energy (mJ)	125
Microwave ejection timing according to spark signal (μs)	−500 to 500 (250 μs step)

the peak of in-chamber pressure. The base line data using conventional spark ignition was carried out with all ignition components but microwave was not applied by turning off during the test.

9.3 Results and Discussions

9.3.1 Comparison of Discharge Characteristics

Figure 9.2 presents averaged OH radical intensity by the ignition itself under the initial ambient pressure of 0.3 and 0.5 MPa at 0.5 ms after the spark event. Microwave

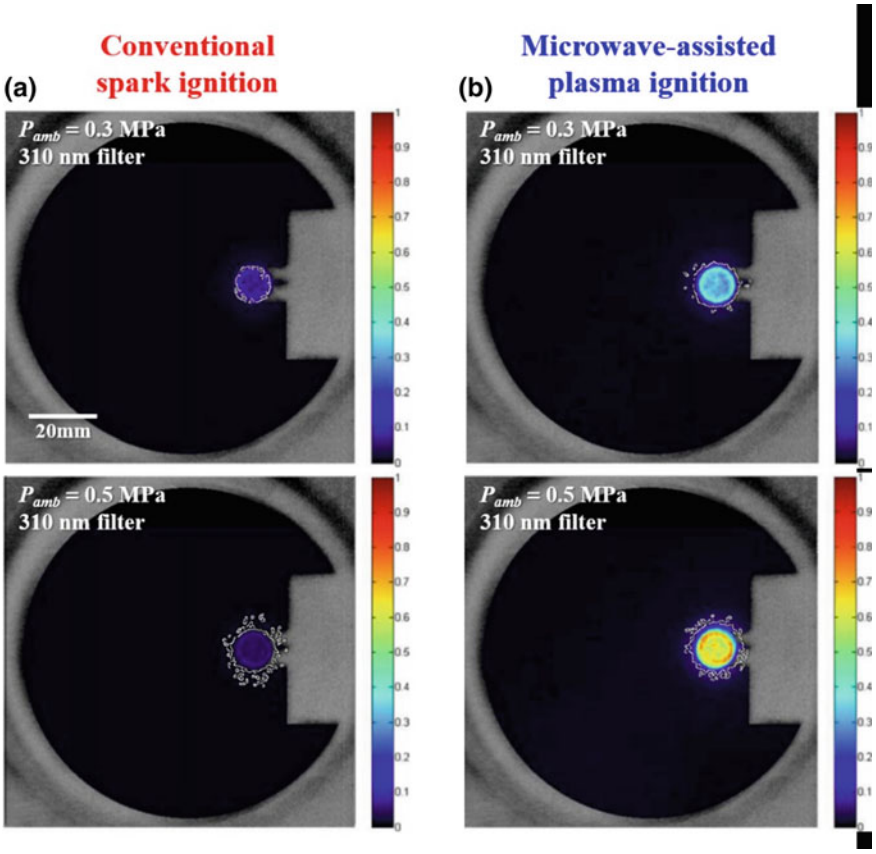

Fig. 9.2 Comparison of OH radicals generated by **a** conventional spark ignition and **b** microwave-assisted plasma ignition. The image shows ensemble averaged OH intensity of five different discharge events. White outline in the discharge differentiate discharge area

ejection timing was 250 μs prior to the spark event. The intensity as well as covered area by OH radial with microwave ejection is greater than the conventional spark ignition. This implies that even though the ignition itself was initiated by a thermal plasma by the conventional discharge, the expansion of plasma was governed by non-thermal process (Sun et al. 2016). It is possible that both electrons and ions interacted with the microwave and finally turned into high energy state (Bittencourt 2004). The electrons in plasma can easily be accelerated because of small mass. They can absorb much energy from the external electric field produced by 2.45 GHz microwave. Ju et al., elucidated that the temperature of electrons in microwave-assisted ignition was higher than conventional coil ignition case (Ju and Sun 2015). The highly energized electrons then transfer their energy through collisions to relatively heavy molecules and finally cause ionization and dissociation of the molecules. Therefore, the reactive radicals such as OH were produced more efficiently with microwave ejection than the conventional spark ignition.

Emission spectrum of microwave-assisted plasma ignition and conventional spark ignition was compared in Fig. 9.3. The discharge repeated 5 Hz and the data acquisition time for conventional spark and microwave-assisted ignition cases were 4 s and 0.4 s, respectively to avoid saturation. Typical vibrational structure of molecular emission spectra of N_2 and N_2^+ can be seen in the conventional spark ignition case. Meanwhile, a number of emission lines from monoatomic and the nitrogen molecular remains almost at background level with microwave-assisted plasma ignition

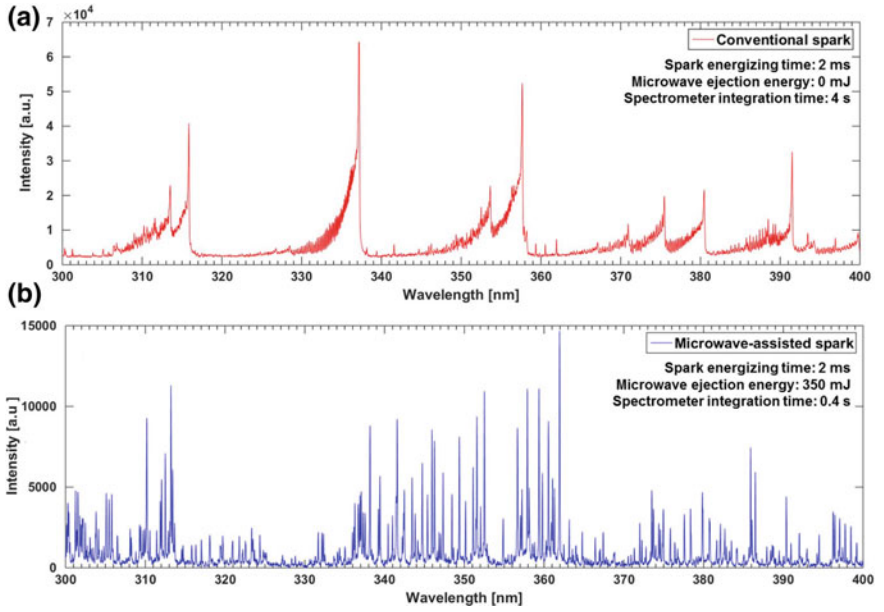

Fig. 9.3 Optical emission spectroscopy using **a** conventional spark ignition and **b** microwave-assisted plasma ignition under 1 bar ambient pressure condition

case. Our analysis on electron temperature using SPARTAN revealed that the electron temperatures under microwave ejection and conventional spark ignition were 23,500 K and 17,300 K respectively (Hwang et al. 2017). This result explains that the microwave ejection can effectively increase the T_e, or correspondingly the kinetic energy of free electrons than conventional spark discharge.

The intensity of OH radicals on the flame surface is shown in Fig. 9.4. The image shows the ensemble averaged OH intensities from five different events. The images were captured at 6 ms and 4 ms for lambda of 1.67 and 1.25, respectively. It is clear that the OH radicals on the flame surface was larger with microwave ejection case than conventional spark ignition. This result clearly indicates that the combustion occurred more vigorously due to higher electron temperature and rich reactive radicals. Electrons in the surface of flame front can be activated by oscillating microwave

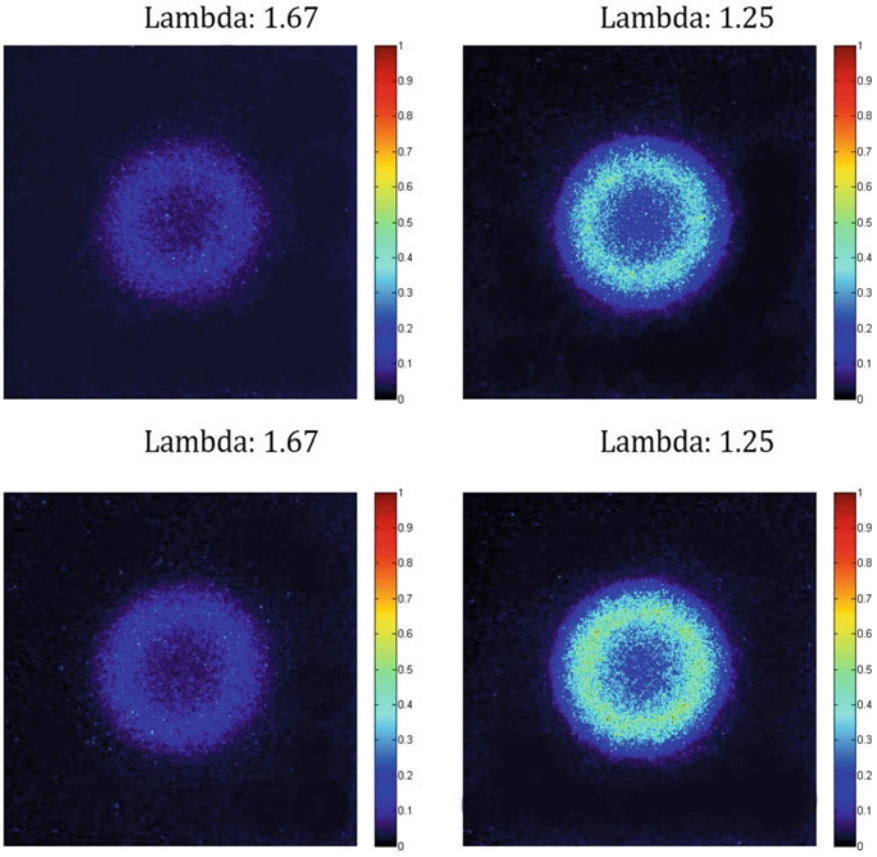

Fig. 9.4 OH radical intensity on the flame front upper figures present conventional spark ignition, bottom figures show microwave-assisted plasma ignition under ambient pressure of 0.3 MPa

and this is an effective source for enhancement on chemical kinetics because the electron density is high ($10^{18}/m^3$) which is two to three orders of magnitude higher than in the burnt downstream gases (MacLatchy 1979). The high electron density in the flame front implies that the electric conductivity of the flame front is high and thus ohmic heating occurs due to the field (Maclatchy et al. 1982). The excited electrons are considered as a catalyst in the chemical reaction as they promote reaction rate. Stockman et al., measured OH radicals by planar laser induced fluorescence (PLIF) and the result showed that the peak OH-number density increased by 6.5% with the microwave application (Stockman et al. 2009). The temperature increase in the post-flame gases was corresponded to 20–40 W and this was estimated approximately 2.3% of magnetron power.

9.3.2 *Effect of Microwave Ejection on Combustion Phase and Lean Limit*

Flame development time (FDT) defined as a timing when 10% of total net heat release depending equivalence ratio is presented in Fig. 9.5. The initial ambient pressure and microwave ejection timing was fixed at 0.1 MPa and 250 μs before the spark event. Under the equivalence ratio of 0.4, both ignition system had misfires, however, microwave-assisted plasma ignition extended lean limit up to 0.5. The possible reason for the extended lean limit is larger initial flame kernel due to higher electron temperature and enhanced chemical kinetics as we discussed above. The extended lean limit can provide many advantages to internal combustion engines in terms of fuel efficiency as well as emission characteristics (Zhao et al. 1999; Ceviz et al. 2012; Zhuang and Hong 2014). The lean-burn concept can be especially applied to reduce the fuel consumption when the engine is under idling condition and

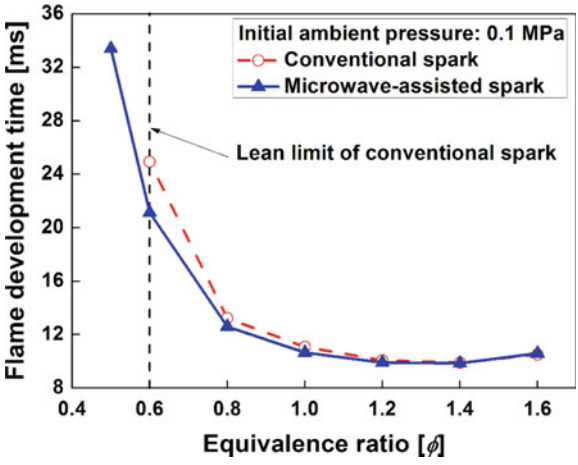

Fig. 9.5 Comparison of flame development time using conventional spark ignition and microwave-assisted plasma ignition under 0.1 MPa ambient condition

to avoid the lean limit flame out. The reduction of nitrogen oxides (NO_x) is also able to achieve by applying this lean-burn concept. In terms of the combustion phase, the microwave-assisted plasma ignition showed advanced FDT, especially under lean fuel-air mixture conditions. Meanwhile, the difference between the conventional spark ignition and microwave-assisted plasma ignition seemed negligible under rich mixture where the flame propagation speed is already high enough. In this aspect, the newly developed system can provide an option of on/off function depending on the engine operating conditions.

The representative shadowgraph images which are closest to the mean value of the flame is shown in Fig. 9.6. The averaged flame kernel size is also presented in Fig. 9.6b. The flames from both ignition systems are laminar flame showing spherical smooth flame front. As confirmed in the combustion phase result, we can expect larger flame kernel with microwave-assisted plasma ignition than using conventional spark ignition. The flame kernel size was defined as a largest distance in width direction from the shadowgraph images. Based on our measurement, the flame speed was increased up to 20% under lean condition, the equivalence ratio of 0.6. It is known that the faster flame growth is beneficial to mitigate knock tendency in spark ignition engines (Heywood 1988). Thus the fuel economy can be enhanced by advancing the spark timing thanks to the faster flame propagation. However, as it confirmed in combustion phase result, the enhancement in the flame speed was disappeared under fuel rich condition. On possible reason is that the time for energy deposition on the flame front got shorter due to the higher flame propagation speed under rich condition. From the previous study, it is known that the microwave power was attenuated by the third power of distance from the electrode (Ikeda et al. 2009). Thus if the flame front is out of spark plug region, microwave ejection is no longer effective.

9.3.3 *Effect of Ambient Pressure on Combustion Enhancement by Microwave Ejection*

The effect of initial pressure on enhancement by microwave ejection was compared under equivalence ratio of 0.6. The microwave ejection timing was varied from 500 μs before the spark event to 500 μs after the spark event. The index of combustion (I_c) was defined to evaluate the performance of a plasma igniter under various ambient pressure conditions (Hwnag et al. 2016). The I_c was calculated based on in-cylinder pressure measurement. It is presented by an Eq. (9.1) below.

$$\text{Index of combustion } (I_c) = (P_{max,p}/P_{max,con})/(t_p/t_{con}) \tag{9.1}$$

where $P_{max,p}$ is the maximum in-chamber pressure with microwave ejection, t_p is the time of the peak pressure with the microwave ejection, $P_{max,con}$ is the maximum in-chamber pressure with the conventional spark, and t_{con} is the time of the peak

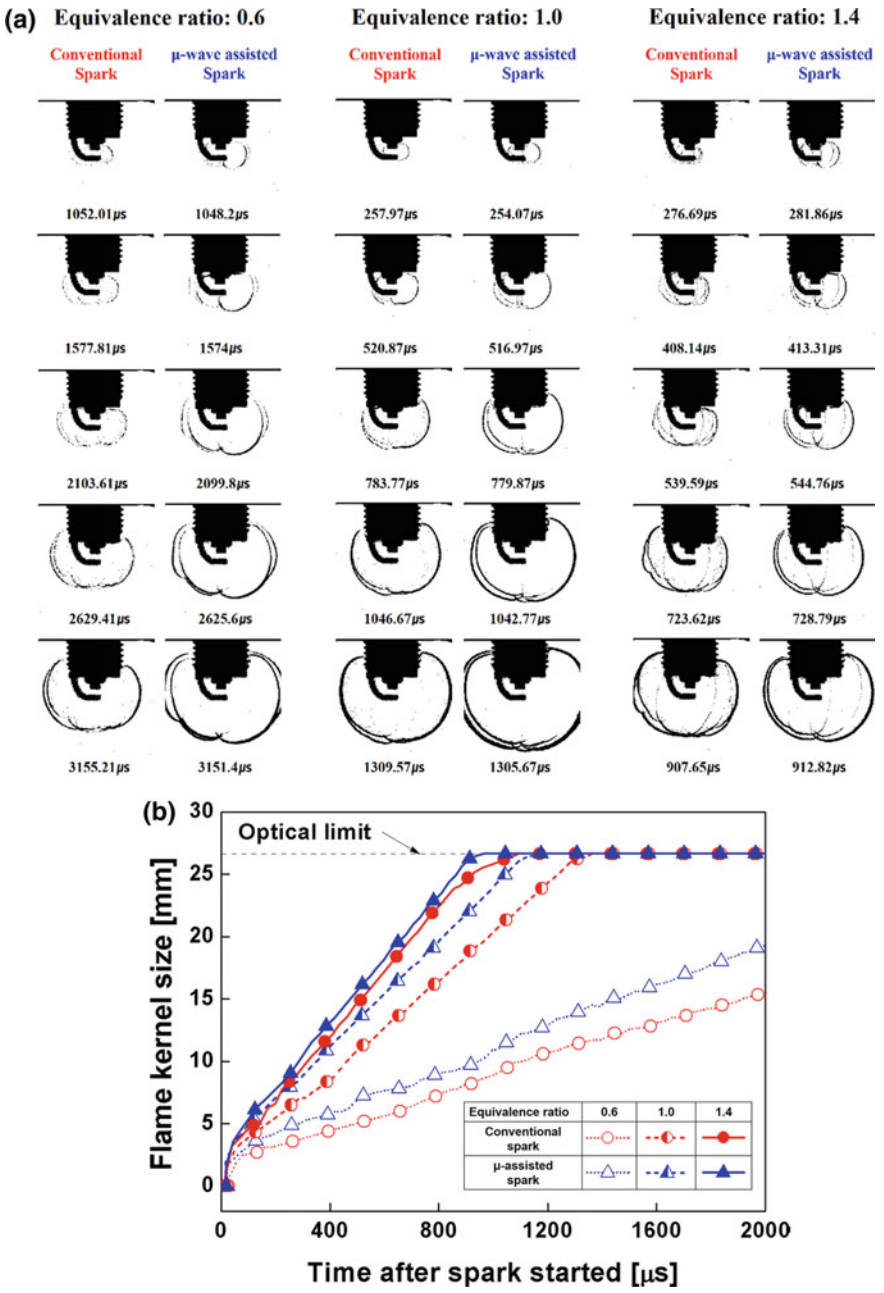

Fig. 9.6 **a** Consecutive flame images under three different equivalence ratio and **b** comparison of flame kernel size according to time after spark started

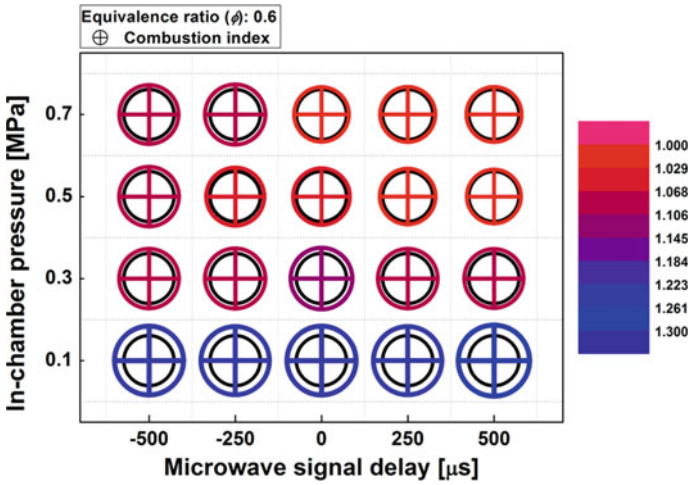

Fig. 9.7 Combustion index calculated at the equivalence ratio of 0.6 and various initial ambient pressure and microwave ejection timing

pressure with the conventional spark. The microwave-assisted plasma ignition system was effective when the index of combustion was greater than 1.

The index of combustion at the equivalence ratio of 0.6 is shown in Fig. 9.7. The black circle represents the performance of conventional spark ignitor, and the cross circles are from microwave-assisted plasma ignition. If the cross circle is bigger than black circle, it means the effectiveness of microwave ejection is larger. The color bar on the right side indicates absolute value of the combustion index. The measurement showed that the enhancement by microwave ejection is noticeable under low initial in-chamber pressure conditions. On the other hands, the effect of the microwave-assisted plasma ignition system was getting smaller under higher initial ambient pressure especially with the retarded microwave timing conditions. There was no noticeable difference over 0.5 MPa with microwave ejection timings of +0, +250 μs, and +500 μs cases. Meanwhile, the early microwave ejection case maintained the combustion index of approximately 1.1 even 0.5 MPa conditions. The reason is that the microwave energy was being able to be transferred not only to the fuel-air mixture but also to the flame front by the early microwave ejection.

9.4 Conclusions

The influence of microwave-assisted plasma ignition on flame development was investigated in a constant volume combustion chamber. The new system using 2.45 GHz magnetron with 3 kW power, mixing unit and a non-resistor sparkplug was developed to apply high voltage DC as well as microwave simultaneously.

High-speed shadowgraph imagine and OH radical imaging were carried out with in-cylinder pressure analysis. The major findings of this study are summarized as below.

(1) The initial flame kernel growth could be enhanced with microwave ejection because of the larger plasma region which contained abundant radical pool and hotter electrons. The OH imaging for the flame front indicated higher OH intensity with microwave ejection than conventional spark ignition. This explains that the enhancement mechanism is driven by non-thermal plasma.
(2) The flame propagation speed with microwave ejection was increased 20% under fuel lean condition showing larger initial kernel growth by shadowgraph imaging. However, enhancement of flame kernel was reduced under fuel rich condition where the flame propagation speed was fast enough.
(3) Index of combustion analysis showed that the effect of microwave ejection under high ambient condition was decreased. The possible reason is that the energy loss due to more frequent collisions between the electrons and gas molecules got larger under dense ambient conditions. This implies that energy deposition by microwave got lower. However, at this situation, earlier microwave ejection strategy kept the index of combustion larger than 1.

References

Bittencourt J (2004) Fundamentals of plasma physics. Springer

Ceviz MA, Sen AK, Kuleri AK, Oner IV (2012) Engine performance, exhaust emissions, and cyclic variations in a lean-burn SI engine fueled by gasoline-hydrogen blends. Appl Therm Eng 36:314–324

DeFilippo A, Saxena S, Rapp V, Dibble R, Chen JY, Nishiyama A, Ikeda Y (2011) Extending the lean stability limits of gasoline using a microwave-assisted spark plug. SAE Technical Paper No. 2011-01-0663

Fridman A (2008) Plasma chemistry, 1st ed. Cambridge University Press

Genzale CL, Pickett LM, Hoops AA, Headrick JM (2011) Laser ignition of multi-injection gasoline sprays. SAE Technical Paper No. 2011-01-0659

Hampe C, Bertsch M, Beck KW, Spicher U, Bohne S, Rixecker G (2013) Influence of high frequency ignition on the combustion and emission behavior of small two-stroke spark ignition engines. SAE Technical Paper No. 2013-32-9144

Heywood JB (1988) Internal combustion engine fundamentals. McGraw-Hill

Hwang J, Kim W, Bae C, Choe W, Cha J, Woo S (2017) Application of a novel microwave-assisted plasma ignition system in a direct injection gasoline engine. Appl Eng 205:562–576

Hwnag J, Bae C, Park J, Choe W, Cha J, Woo S (2016) Microwave-assisted plasma ignition in a constant volume combustion chamber. Combust Flame 167:86–96

Ikeda Y, Nishiyama A, Kaneko M (2009) Microwave enhanced ignition process for fuel mixture at elevated pressure of 1 MPa. In: 47th AIAA aerospace sciences meeting including the new horizons forum and aerospace exposition

Ju Y, Sun W (2015) Plasma assisted combustion: dynamics and chemistry. Prog Energy Combust Sci 48:21–83

Luo Y, Alger T, Mangold B, Gingrich J, Kinkler S (2019) Microwave enhancement of lean/dilute combustion in a constant-volume chamber. SAE Technical Paper No. 2019-01-1198

MacLatchy C (1979) Langmuir probe measurements of ion density in an atmospheric pressure air-propane flame. Combust Flame 36:171–179
Maclatchy C, Clements R, Smy P (1982) An experimental investigation of the effect of microwave radiation on a propane-air flame. Combust Flame 45:161–169
Oh H, Bae C (2013) Effects of the injection timing on spray and combustion characteristics in a spray-guided DISI engine under lean-stratified operation. Fuel 107:225–235
Shiraishi T, Urushihara T (2011) Fundamental analysis of combustion initiation characteristics of low temperature plasma ignition for internal combustion gasoline engine. SAE Technical Paper No. 2011-01-0660
Starikovskii AY (2005) Plasma supported combustion. Proc Combust Inst 30:2405–2417
Starilovskaia SM (2006) Plasma assisted ignition and combustion. J Phys D Appl Phys 39:265–299
Stockman E, Zaidi S, Miles R, Carter C, Ryan M (2009) Measurements of combustion properties in a microwave enhanced flame. Combust Flame 156:1453–1461
Sun J, Wang W, Yue Q, Ma C, Zhang J, Zhao X, Song Z (2016) Review on microwave-metal discharge and their applications in energy and industrial processes. Appl Eng 175:141–157
Szwaja S, Jamrozik A, Tutak W (2013) A two-stage combustion system for burning lean gasoline mixtures in a stationary spark ignited engine. Appl Energy 105:271–281
Tang H, Pennycott A, Akehurst S, Brace CJ (2015) A review of the application of variable geometry turbines to the downsized gasoline engine. Int J Engine Res 16:810–825
Thostenson ET, Chou TW (1999) Microwave processing: fundamentals and applications. Compos Part A Appl Sci 30:1055–1071
Wang Z, Huang J, Wang Q, Hou L, Zhang G (2015) Experimental study of microwave resonance plasma ignition of methane-air mixture in a constant volume cylinder. Combust Flame 162:2561–2568
Wei H, Zhu T, Shu G, Tan L, Wang Y (2013) Gasoline engine exhaust gas recirculation—a review. Appl Energy 99:534–544
Wolk B, DeFilippo A, Chen JY, Dibble R, Nishiyama A, Ikeda Y (2013) Enhancement of flame development by microwave-assisted spark ignition in constant volume combustion chamber. Combust Flame 160(7):1225–1234
Zhao F, Lai MC, Harrington DL (1999) Automotive spark-ignited direct-injection gasoline engines. Prog Energy Combust Sci 25:437–562
Zhuang Y, Hong G (2014) Effects of direct injection timing of ethanol fuel on engine knock and lean burn in a port injection gasoline engine. Fuel 135:27–37

Chapter 10
Laser Ignition Technology for Gaseous Fuelled Automotive Engines

Dhananjay Kumar and Avinash Kumar Agarwal

Abstract Most SI engine globally use conventional electric spark plug as an ignition source. Electric spark plugs have limitations in achieving higher efficiency and reducing emissions from gaseous fuelled automotive engine. In contrast to conventional electrical spark plugs, laser spark plugs are apt for use at higher in-cylinder pressures. Laser Ignition technology is capable of igniting leaner fuel-air mixture, which cannot be successfully ignited by conventional spark plugs. Laser ignition has proven its worth in defence and rocketry industry by replacing traditional spark ignition systems globally. Laser ignited combustion can be controlled by only few critical parameters, which makes it useful for implementation in variety of practical applications. Controlled combustion using laser plasma which requires minor engine hardware modifications is the key to implement it for variety of applications. Laser pulse generated plasma at the focal point, which is much more intense than conventional electrical spark plasma, can successfully ignite lean fuel-air mixtures. Main advantages of laser ignition technology include the possibility of igniting leaner fuel-air mixtures and flexibility to freely choose location of the igniting plasma. These interventions lead to lower NOx emissions, increased efficiency while avoids quenching effects due to electrodes, reduced electrode wear and consequently increased the lifetime of the electrodes. Laser ignition can be used for multi-cylinder engine by employing fiber optics and a single laser source. This chapter reviews laser ignition of gaseous fuel-air mixture as well as technology adaptation for implementation of laser ignition in automotive sector.

Keywords Laser ignition · Alternate ignition system · Gaseous fuelled engine · Conventional spark ignition

D. Kumar · A. K. Agarwal (✉)
Department of Mechanical Engineering, Indian Institute of Technology Kanpur, Kanpur, Uttar Pradesh, India
e-mail: akag@iitk.ac.in

A. P. Singh et al. (eds.), *Simulations and Optical Diagnostics for Internal Combustion Engines*, Energy, Environment, and Sustainability,
https://doi.org/10.1007/978-981-15-0335-1_10

10.1 Introduction

In recent years, laser ignition systems have attracted attention as an alternative to conventional electrical spark plugs in lean-burn gas engines because of their ability to improve engine performance and reduce exhaust emissions simultaneously. In late 1960s, the first laser spark assisted ignition of combustible mixture was achieved (Knystautas and Lee 1969). Dale et al. (1978) demonstrated the laser ignition on the engine using a CO_2 laser for the first time. Today, various researchers (Weinrotter et al. 2005; Yalin et al. 2006; Dearden and Shenton 2013; Agarwal et al. 2017; Pavel et al. 2018) are working on conducting feasibility studies for implementation of laser ignition in automotive engines. Studies have shown that laser ignition can be a potential candidate for operations in lean limits (Kopecek et al. 2005; Phuoc 2006). A conventional electric spark plug has various disadvantages such as corrosion of electrodes, and increased voltage requirements with increasing in-cylinder pressure, and electrode acting as a heat-sink to plasma generated heat inside the cylinder (Phuoc 2000). On another side, the laser ignition system provides flexibility to freely choose the plasma location anywhere inside the combustion chamber by selecting optimized focus. One major challenge for implementing laser ignition system for practical applications is the need for a robust delivery system for laser beam from the laser head to the cylinder; and fiber-optics delivery is emerging as an appropriate choice for this application. The open beam path approach that is generally followed at the laboratory scale cannot be considered for practical field applications because of safety, maintenance, and vibration issues of the engine.

Gases have relatively high breakdown intensity nearly 100–1000 GW/cm^2 (Turcu et al. 1997; Phuoc 2000) hence fiber delivery of laser remains challenging as of now (Stakhiv et al. 2004). For gaseous fuel operated multi-cylinder engines, various approaches were investigated (McMillian et al. 2003; Weinrotter et al. 2004–2005; Yalin et al. 2006) for successful implementation of laser ignition system. In the first approach, use of a single laser per cylinder (McMillian et al. 2003), and in another approach, use of a single laser to multiple cylinders with multiplexing was suggested (Yalin et al. 2006). A third and intermediate approach was also explored, in which gain element (amplifiers) was mounted on each cylinder, where pump light was delivered through optical fiber (Weinrotter et al. 2004–2005). All these approaches are discussed in detail in the following section. Laser ignition seems to be more promising to the gaseous fuels such as hydrogen, compressed natural gas (CNG), Hydrogen enriched compressed natural gas (HCNG), and liquefied petroleum gas (LPG), since it allows extended lean limit operation having numerous advantages. Pal and Agarwal (2015) performed experiments on a laser ignited hydrogen engine and reported higher peak cylinder pressure, higher heat release rate (HRR) and shorter combustion duration compared to hydrogen fueled conventional electrical spark ignition engine. Recent studies showed that laser ignition of HCNG-air mixture was more promising than laser ignition of CNG and hydrogen individually.

10.2 Laser Ignition: Opportunities and Challenges for the Development of Gaseous Fuelled Engines

Engine with a laser ignition system offers several advantages over the conventional electric spark ignition system. For gaseous fuelled engine equipped with laser ignition system, initial flame propagation was much faster than electrical spark plug, since flame kernel growth was protected by focusing the laser plasma away from the cylinder walls, leading to lower possibility of flame kernel quenching. Consequently, mass burn duration and ignition delay were shorter, and in-cylinder peak pressure was higher, leading to superior fuel efficiency and lower NO_x emissions. Yalin et al. (2005a, b) studied laser ignition performance by performing experiments on a six-cylinder engine, in which they ignited one cylinder using laser. They reported that the in-cylinder pressure increased faster, and peak in-cylinder pressure was relatively higher compared to other cylinders also mass burned fraction is quicker compared to the electric spark plug.

Herdin et al. (2005) investigated ignition delay and rate of burning using natural gas and concluded that ignition delay was shorter for laser ignition compared to conventional spark ignition. A higher air-fuel ratio can be employed using laser ignition for extending lean limits, which can ensure lower combustion temperature and hence lower NOx emissions along with higher fuel efficiency. Other benefits include more precise spark timings, and opportunity for multi-point ignition, wherein multiple sparks can be generated in the cylinder concurrently. Advantages of gaseous fuel engine equipped with laser ignition system are shown in Fig. 10.1.

Laser ignitions faces many challenges in order to commercialize e.g. laser ignition systems are expensive, hence there is a need for development of compact, economical

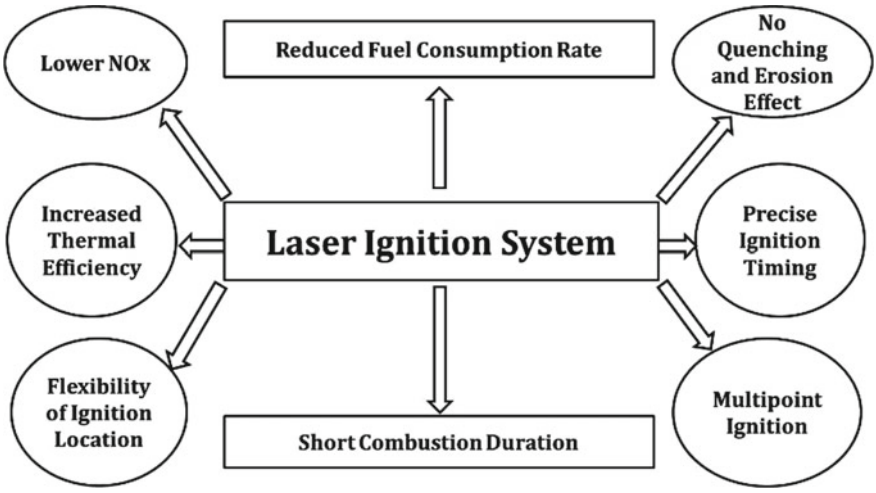

Fig. 10.1 Advantages of laser ignition system (LIS)

laser having robust beam delivery system. Yalin et al. (2006) studied the feasibility of different types of optical fiber cables used for transmission of high power laser pulses. LIS must be robust enough to withstand engine vibrations, mechanical and thermal stresses. Performance of solid-state laser is influenced by ambient temperature of the engine environment since the laser system gives the best performance at temperature up to 100 °C (Wintner and Kofler 2015). External cooling system may be coupled with the engine cooling for better performance. Windows contamination may also be a problem, since it affects the laser performance by creating hurdles in forming the plasma.

10.3 Laser Ignition of Combustible Charge: Modes of Ignition

There are primarily four different means (Phuoc 2006) by which a laser beam can interact with the ignitable mixture to initiate ignition, as shown in Fig. 10.2.

(a) **Photochemical ignition**: Photochemical ignition entails a close match between laser wavelength and absorption wavelength of the molecules. Photochemical ignition does not involve breakdown of gaseous molecules since laser photon absorption takes place in the combustible mixture molecules, which dissociate into atoms and radicals. Dissociation of photons and production of radicals lead to a branched chain reaction, and if the production rate of radicals is higher than their recombination rate, then this reaction leads to the ignition of combustible charge.

(b) **Thermal ignition**: Similar to photochemical ignition, thermal ignition does not involve an electrical breakdown of molecules. Here the kinetic energy of mixture molecules is increased in rotational, translational or vibrational modes by absorbing laser beam energy, which leads to breaking of molecular bonds of combustible mixture molecules and chemical reactions start. In the thermal ignition, mixture must absorb the laser beam energy resonantly. For this, combustible charge must have the resonant species, which match with the laser wavelength.

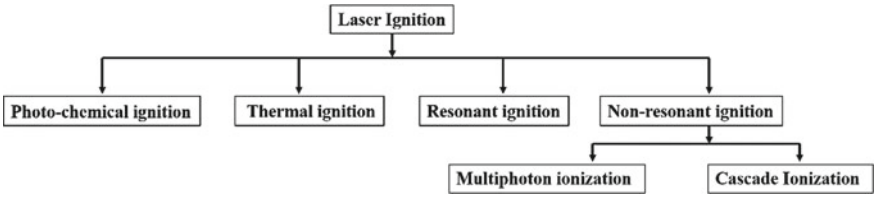

Fig. 10.2 Laser ignition mechanisms

(c) **Resonant ignition**: Laser-induced resonant ignition involves multi-photon non-resonant photochemical dissociation of combustible mixture molecules and resonant multi-photon ionization of atoms produced by photo-dissociation. Henceforth, free electrons are generated, which absorb the laser energy through Inverse Bremsstrahlung effect, leading to an avalanche of electrons, thus causing the breakdown of gases.

(d) **Non-resonant ignition**: Non-resonant breakdown is the most appropriate ignition mechanism since it does not require the mixture molecule should resonate with the laser wavelength (Kopecek et al. 2003). Laser-induced non-resonant breakdown of gaseous particles is generally achieved by multi-photon ionization and cascade ionization. Simultaneous absorption of laser photon by target material takes place in multi-photon ionization, and if absorbed energy is more than ionization potential of the target molecules, then liberated electrons may ionize a particle, leading to production of two electrons of lesser energy. This process is repeated consistently leading to electron avalanche and hence breakdown of combustible charge molecules. Cascade ionization entails two essential environments for the breakdown of gaseous molecules which require that free electron must be available in the focal volume, and free electron must gain the energy from the laser radiation which should be higher than the potential energy of the gas molecules (Radziemski and Cremers 1989). Cascade ionization is generally preferred at elevated pressures and for long pulse laser because the threshold energy required for the breakdown of gases decrease with increasing pressure at specific limits and then increase (Gili and Dougal 1965). Multi-photon ionization mechanism is preferred over cascade ionization at lower pressure and appropriately short laser pulses are required (Phuoc 2000).

It is notable that short and intensified laser pulses can deliver an "optical breakdown" of air. Required intensity for this breakdown is about 100–1000 GW/cm^2 (Turcu et al. 1997; Phuoc 2000). Under such an intense environment, dissociation and ionization of gaseous fuel-air mixture, and molecules take place. Consequently, hot plasma is generated in the vicinity of the focal spot of the laser beam. Focal spot diameter (d) of tightly focused laser light depends on unfocused beam diameter (D) and corresponding wavelength and directing optics (Koechner 1999).

$$d = \frac{4M^2\lambda F}{\pi D} \tag{10.1}$$

where,

M^2 beam quality factor
D initial beam diameter
d focused beam diameter
λ wavelength at initial beam diameter D
F focal length of the optical element.

A sensible diameter is in the range of 200 μm, and within a spherical volume (V) the number of particles depends on the temperature (T) and pressure (P) according to the ideal gas law equation (Liedl et al. 2005):

$$N = \frac{PV}{KT} \tag{10.2}$$

where,

N number of particles present in the focal spot volume
K Boltzmann's constant (1.38×10^{-23})

Ionization and dissociation of gaseous particles entail certain extent of energy, which has to be supplied by the laser beam. Figure 10.3 (Pavel et al. 2018) explains

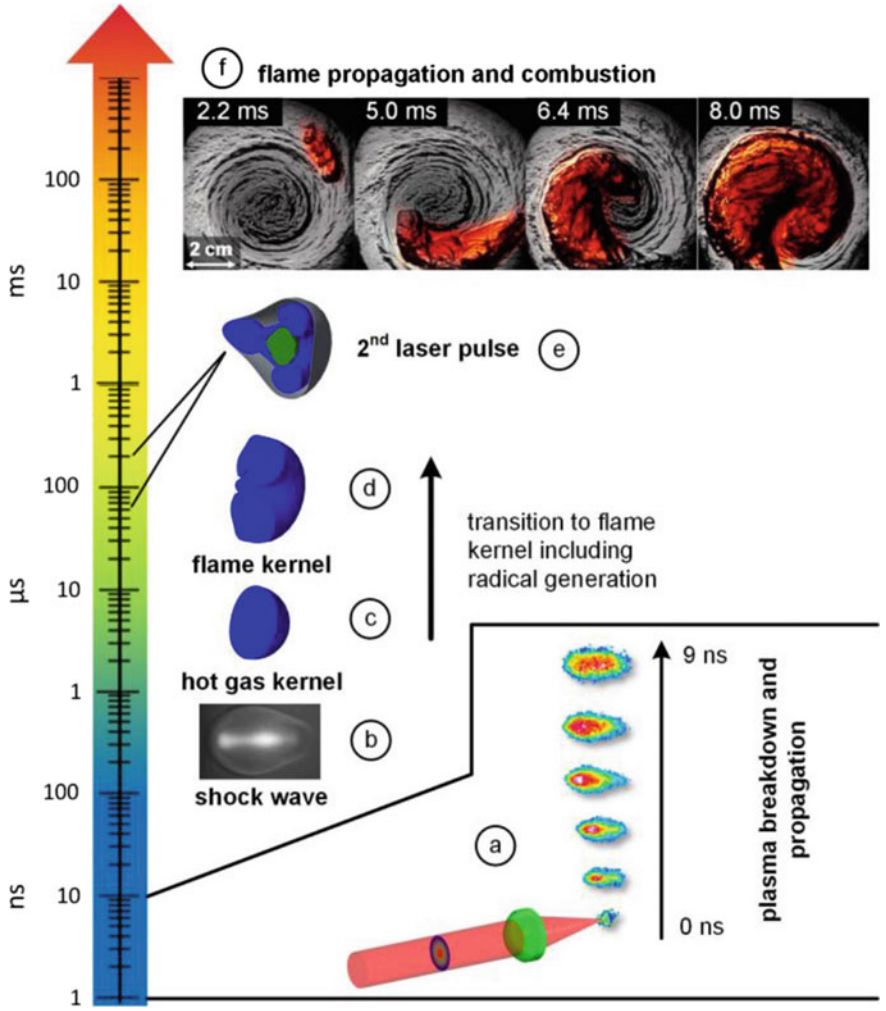

Fig. 10.3 Temporal progress of non-resonant laser ignition process (Pavel et al. 2018)

different stages of laser ignition interaction through non-resonant breakdown mechanism. The mechanism requires multiphoton ionization, which generates free electrons. Figure 10.3a shows plasma breakdown and propagation within 0-9 ns. After few 10th to 100th of a nanosecond, a shockwave is released because of rapid increase in temperature and pressure (Bradley et al. 2004; Phuoc 2006) and propagates towards colder ambient gas with supersonic speed (Gregorčič et al. 2013). Residual hot gases formed a spherical shape (Fig. 10.3c), which collapsed after a few microseconds and then a donut-like structure was observed (Fig. 10.3d). Interaction of second kernel flame with the first one is shown in Fig. 10.3e and is formed in the center of the first kernel. The shockwave propagation of the second kernel is faster inside the first kernel, which may be because of relatively inferior concentration of hot gases. For successful ignition, persistent flame propagation (Fig. 10.3e) leads to complete combustion of a charged particle.

10.4 Methods of Laser Beam Delivery for Engine Ignition

One of the significant concerns for the application of laser ignition in the automotive industry is the delivery of laser beam from the source to the engine cylinders. For implementation of laser delivery in an engine conditions, several challenges are required to be overcome such as vibrations, dirt, heat, and vapors. Concerns related to high costs, ease of use and maintenance, and safety have also prohibited this technology from being used extensively. Researcher have various proposed solutions over time about the benefits and challenges of using laser ignition. Some of the approaches are discussed in the following section.

10.4.1 Open Path Beam Delivery Approach

This approach is widely used in the lab scale experiment. In this approach, a laser is employed near the engine along with a set of mirror and lenses, which direct the laser beam to the engine combustion chamber. Various studies (Herdin et al. 2005; Ahrens et al. 2005; Srivastava et al. 2014; Singh et al. 2017) have been performed using open beam path approach. The advantage of this approach includes ease of developing the experimental setup in the lab and freedom to measure various parameters during the engine operation. Hence, it is a right approach for lab scale testing and demonstration, where various controls are preferred however for the use at Industrial scale, this approach will not be a right choice. For successful plasma generation, precise alignment of laser beam with appropriate focusing optics is essential. Engine vibrations relative to laser source may lead to beam misalignment, and the system may not work. Engine environment is often full of vapors, dust, and particulates and may contaminate the mirror and lenses, leading to transmission losses, poor beam quality,

and eventually damage to the optics. Due to these factors, open path approach is not appropriate for the industry use.

10.4.2 Single Laser per Cylinder

An alternative to open beam approach may be placing a compact laser directly on top of each cylinder (Fig. 10.4). This approach will ensure that there is no exposure to the laser light near the engine, hence avoiding creation of hazardous situation for the personnel, and avoiding the challenge of misalignment of laser beam simultaneously. In this strategy, lasers have to pass through a limited number of optics, and hence problems accompanying energy and transparency loss are avoided. The challenges involved here is to develop a compact laser that could be fitted on the engine cylinder head and would provide sufficient power for the breakdown of gaseous molecules in the engine combustion chamber. Several probable systems have been demonstrated by the researchers.

A miniature diode pumped laser was designed by Kroupa et al. (2009). They used Cr: YAG saturable absorbing agent as Q-switch. This miniature laser yields 25 mJ energy at a frequency of up to 100 Hz. Breakdown in the air was easily attainable at focal lengths up to 80 mm by utilizing appropriate focusing elements. Kroupa et al. (2009) successfully tested it on the engine and found it to be reliable. They further extended the lean limit ignition compared to conventional spark plugs. Another similar Q-switch diode pumped laser was designed and patented by Inohara et al. (2009). The laser emitted a sequence of pulses with a total energy of approx. 7 mJ and temporal spacing between pulses of 10 to 300 μs. A slight extension of lean limit was also achieved by this laser when tested on the engine. While results of these

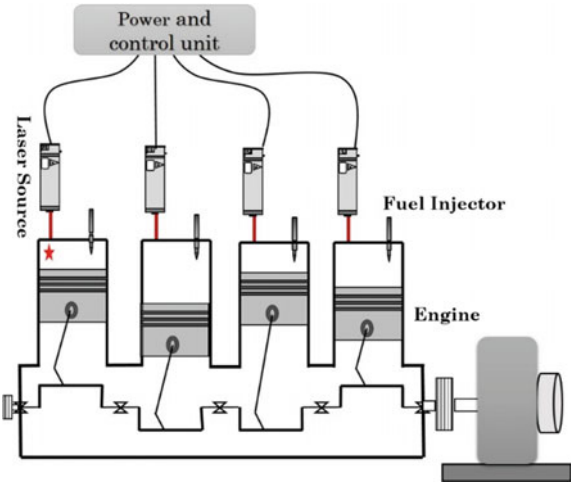

Fig. 10.4 Schematic showing single laser per cylinder

improvements demonstrate the capability of the ignition system for a multi-cylinder engine, many factors limit their pragmatism in real applications. This was because the laser unit was directly installed on the cylinder head therefore a separate dedicated cooling system was required to prevent wavelength drifting. Engine undergoes constant vibrations that may misalign the laser cavity. Finally, the cost issues do not support this approach for practical usage, especially in multi-cylinder engines.

10.4.3 Use of Optical Fibers for Laser Beam Delivery

The above approach has practical limitations and is not economically viable due to requirement of multiple laser sources for multi-cylinder engines. Optical fiber provides an edge to overcome the engine vibrations and ensures safety from the high-intensity laser beam. In the following section, different types of fibers are explained along with their suitability for laser spark formation.

10.4.3.1 Fiber Delivered Diode Pump/Laser Pulse

One economical alternative to placing one laser per-cylinder can be direct installation of the gain medium on each cylinder head and utilizing the pumping light from a single source through fiber optics using a suitable multiplexer system. This requires one laser gain crystal for each cylinder that makes it is costly but less costly compared to installing one laser per cylinder. Adequate cooling system will be required since the gain medium is situated very close to the combustion chamber. This type of laser was built by Kofler et al. (2007) which produced 6 mJ pulse energy with <1.5 ns pulse duration at a pump power of 300 W. They also concluded that pump geometry was a very sensitive parameter for the laser performance. However, no on-engine investigation was implemented. The researchers acknowledged that further study was required to determine the influence of temperature and mechanical vibrations from the engine on this system.

Another practical approach may be direct delivery of laser pulses through optic fibers. This way, one can install the laser source far from the combustion chamber, and will be able to overcome challenges due to vibrations and heating of the gain medium. In this approach, only one laser source is required, which will help to make this technology cost-effective. Laser beam is multiplexed into optical fiber cable, whose one end is connected to the optical spark plug containing collimating and focusing elements, which form the spark inside the cylinder. A simple schematic of this concept is shown in Fig. 10.5. The main challenges include limitations of utilizing optical fiber cable for beam delivery. For multi-cylinder engine, multiplexing laser into multiple fibers accurately is a challenging task. Optical fiber faces generally have a diameter less than 1 mm, and beam has to be align accurately at rates up to 240 Hz, which requires precise optical components.

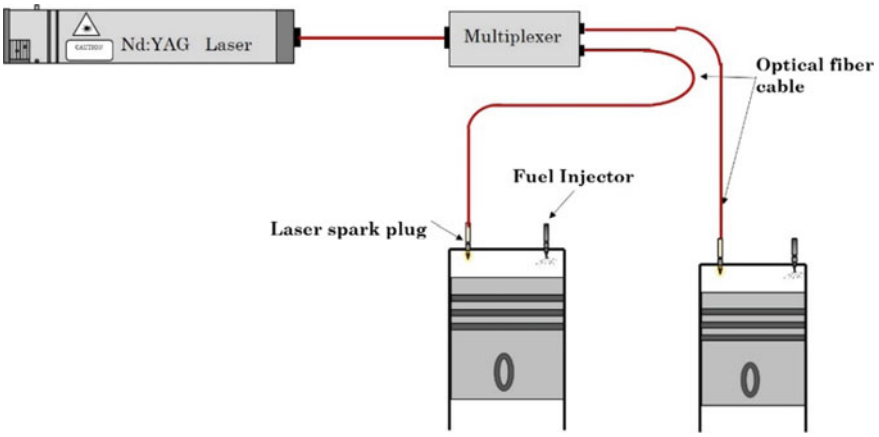

Fig. 10.5 Schematic of laser beam delivery through optical fiber

10.4.3.2 Hollow Core Fibers Delivery

Now-a-days, use of hollow core fiber is emerging as promising solution for delivering of high energy pulses. Hollow glass fiber and dielectric capillaries with olefin polymer-coated silver have been tested for laser ignition applications for the engine. The dielectric capillary type hollow fiber uses a simple glass conduit that guides the beam by total internal reflection at a glass-air interface. It is not considered for the practical use though because it encounters high transmission loss and the fibers are not very flexible, thus dampening the main advantage sought from the optical fiber laser beam delivery. On the other hand, cyclic olefin polymer-coated silver hollow fibers are capable of providing better transmission efficiency and they are much more flexible hence they are preferred for laser pulse delivery. These fibers use much thinner glass conduit having polymer and silver layers inside to direct the light.

The first use of hollow core fiber to deliver nanosecond laser was claimed by Yalin et al. (2005a, b) in which they successfully generated plasma in the atmospheric air. They used 700 μm core diameter, 1 m long fiber having a transmission efficiency of ~80% at lower power and ~70% at a peak power of 47 mJ. Beam quality factor M^2 was reported to be in the range of 11–26 for different launch condition; lower M^2 value was found for smaller launch divergence angle. They observed ~97% success in spark formation rate with tight focusing of the fiber. Slightly longer fiber of 2 m having 1 μm core diameter was tested by Reynolds (2011) which delivered similar results and slight improvement in M^2 at best launch conditions. A term, figure of merit (FOM) was used by Joshi et al. (2007) to compare different type of optical fibers and they reported that hollow core fiber exhibited the highest FOM as shown in Table 10.1.

Table 10.1 Calculated FOM values for different fibers (Joshi et al. 2007)

Fiber type	I_{exit} (GW/cm^2)	θ_{exit}	FOM
Solid core silica fiber (base NA)	3	0.05	0.34
Coated hollow fiber	2	0.01	5.6
Photonic crystal fiber	12	0.04	2.8
Fiber laser	8	0.02	4.9

where,

I_{exit} Intensity of laser pulse at fiber exit
θ_{exit} Angular divergence of light at fiber exit.

10.4.3.3 Solid Core Fibers

These fiber types have long been used widely for communication purposes in telecom industry. These are conventionally thought to be incapable of high energy laser beam delivery. Solid core fibers are not very frequently used for engine application because of difficulties in mode coupling and deprivation of laser quality. A couple of engine test were conducted to study the feasibility of solid core fibers for laser pulse delivery. Mullet et al. (2009) performed an experiment with fibers of 400 and 600 μm core and ignited one of four-cylinder using the laser system; however, they observed significant misfire in the cylinder, which was ignited by the laser. They compared the successful ignition rates to be 13% and 44% out of 300 consecutive combustion cycles for 400 μm and 600 μm core optical fibers respectively. Biruduganti et al. (2004) performed an experiment using 1 mm core fiber, and they could ignite the engine without any misfire; however, they were not able to initiate the ambient air breakdown.

10.4.3.4 Photonic Crystal Fibers (PCFS) and Hollow Core Photonic Bandgap (PBG) Fibers

Photonic crystal fibers (PCFs) and Photonic bandgap (PBG) fibers have periodic hole structures inside the fiber material, which can guide the laser light in an effective manner, including single mode operation. These are new class of optical fibers, which offer several unique properties such as they take advantage of crystal structures. Matsuura et al. (1998) successfully demonstrated PBG fibers with a laser pulse energy of 0.37 mJ at 1064 nm having 65 ns pulse duration. Joshi et al. (2007) investigated PCF with a core 25 μm and fiber length of 2 m. M^2 ~ 1.4 was observed when a spatial filter was used. They found the maximum achievable output of 0.55 mJ with energy input of 1.3 mJ. Hence this fiber has not shown significant real potential for laser beam delivery for the engine application; however, in future, there is quite

high chance of developments in the laser energy carrying capacity of such fibers, which will make it potentially useful for engine application.

10.5 Multiplexing

An impending advantage of fiber delivery approach is to utilize a single laser source to a number of cylinders via multiplexing. Multiplexing is a process of utilizing a single laser for multiple cylinders of an engine using appropriate sequential laser beam delivery system.

10.5.1 Why Multiplexing?

For laser ignition in IC engines, the approach generally followed is that of a direct-mounted laser source for each cylinder. This approach is quite expensive for multi-cylinder engines due to high cost of laser system, even in batch production. Researchers therefore prefer open beam path system for transferring the beam to the engine combustion chamber; however optical fiber delivery system coupled with multiplexer is preferred over the open beam path beam delivery systems for numerous reasons, as summarized:

(a) **Alignment Issues**: In open beam path system, required optical components in-between the laser source and the engine cylinder must be held accurately aligned despite momentous vibrations in the engine. Further, this alignment should be sustained over a long operational period. On the other hand, optical fibers give the flexibility of not getting affected by engine vibrations hence significantly reduce the beam misalignment issues.
(b) **Safety Issues**: In open laser beam path approach, safety is a big concern since both infrared and visible light lasers are invisible when they propagate through the ambient space. Hence there are high chances of laser beam to get interrupted by some reflective objects and deviate from its original path and move around the open space near the engine. This leads to a potential threat to personnel operating in the vicinity of the engine. On the other hand, safety increases with the use of optical fibers since they contain the entire beam between the multiplexer and the engine. Hence this system offers enhanced safety compared to open beam path approach.

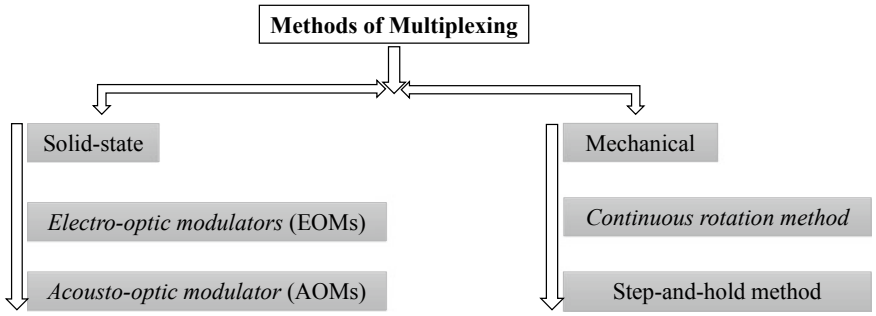

Fig. 10.6 Different multiplexing types

10.5.2 Methods of Multiplexing

There are two main types of multiplexing method, namely (i) Solid-state, and (ii) Mechanical. Further classification are shown in Fig. 10.6.

10.5.2.1 Solid-State Multiplexing

Solid-State Multiplexing can be utilized in high-speed multiplexing without any moving parts, however these systems are relatively expensive since they require N-1 number of an optical modulator, where N is the number of fibers. Optical modulators are expensive.

Electro-optic modulators consist of non-linear optical crystal, which utilizes the electric field for changing the optical properties (Paschotta 2008). To achieve the objective of multiplexing, electro-optic modulator, for instance, Pockels cells which rotate the beam polarization, can be used alongside polarizers and polarization dependent glasses (Early and Lester 1999). This method relies on polarity, and hence laser polarity is achieved first using a polarizer. Thereafter the beam passes through an optical modulator, which rotates the polarization of the beam through 90°, when active otherwise not. The laser beam then goes through a polarizing splitter, which permits the beam to pass through unaffected in one particular polarized direction, but reflects the beam by 90° in the opposite direction for another polarized beam. The arrangement of beam-splitter has to be in such a way that the beam will pass without reflection, when optical modulator, which is installed just before it, is passive, but when optical modulator is active, the beam will be reflected by 90° and focused into an optical fiber, which is connected to one of the engine cylinders. This way, multiplexing is achieved by electro-optic modulators.

In acousto-optic modulator, light diffracts along a different path, when the acoustic effect is utilized. To induce the acoustic waves in the material and hence to change the optical properties, a piezoelectric transducer is used (Paschotta 2008). Acousto-optic modulators can be utilized similar to an electro-optic modulator.

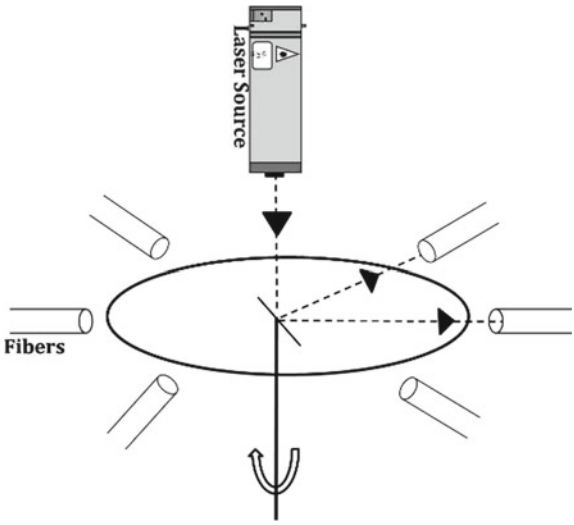

Fig. 10.7 Continuous rotation method for multiplexing

10.5.2.2 Mechanical Multiplexing

Mechanical multiplexing method utilizes a set of mirrors, which physically rotate in the direction of an incoming laser beam, and direct it into the desired fiber. Mechanical multiplexing can be classified further into two categories viz. continuous rotation method and step-and-hold method. In continuous rotation approach, multiplexing is achieved by fixing a mirror on the motor shaft at 45°, in such a way that laser beam encountering the mirror get reflected to an angular direction, depending on the speed of the motor. Optical fiber is installed radially in such a manner that with positional feedback, laser beam can be coupled to each fiber in a proper sequence. Schematic of this approach is shown in Fig. 10.7.

Continuous rotation approach is relatively simple in design and cost-effective since it utilizes set of a mirrors and a motor however on another hand, this method does not give flexibility for instant timing alterations, and it entails a very high sensitivity positional feedback from the motor to focus the beam into each fiber.

Another method of mechanical multiplexing is step and hold approach. In this approach, a mirror is focused at a particular fiber and seized there for some time, and then the laser is fired. Thereafter the mirror is centered to the next fiber for ignition in the next engine cylinder. A schematic of this step-and-hold multiplexing system is shown in Fig. 10.8.

High precision piezoelectric stacks can be utilized for switching by fixing the mirror with them in such a way that expansion or contraction of one (or two) stack(s) cause the mirror to rotate along the fiber direction. Even with high precision stacks,

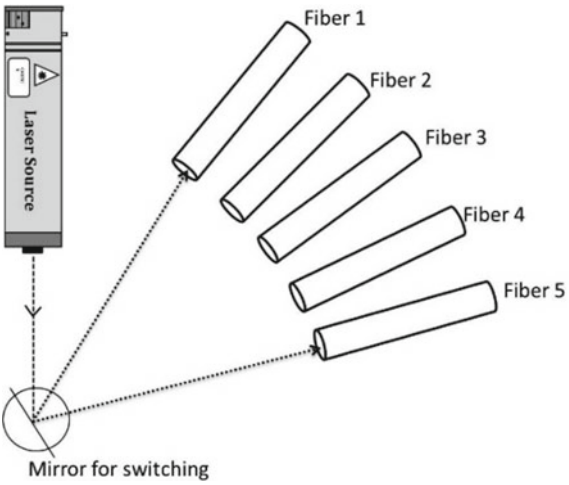

Fig. 10.8 Schematic of step-and-hold multiplexing approach

this system does not have enough range for multi-cylinder engine application (Thorlab catalog). Use of galvanometer can be alternative to switching the mirror in step-and-hold approach. Galvanometer has a magnetic coil that can rotate the attached part (mirror in this case) in any direction in its range.

10.6 Case Studies of Successful Laser Ignited Engine

For preliminary studies of the laser ignition system, several researchers have performed experiments on a constant volume combustion chamber for simulating engine like conditions before moving to a real engine experiments. Some case-studies are discussed in the following section, which incorporate successful laser ignition system demonstrations.

Case Study 1: Constant volume combustion chamber studies

Understanding of flame kernel growth is essential when it comes to gaseous fuel operated vehicles since this is the point where combustion gets initiated. For SI engines, compressed natural gas (CNG) can be used as an alternative fuel because it possesses high octane number and the laser ignited engines can be operated at higher compression ratios (Srivastava and Agarwal 2014) which will offer superior thermal efficiency and reduced emissions compared to conventional spark ignited engines. CNG has relatively slower flame speed (Srivastava and Agarwal 2014; Karim et al. 1996), and this problem can be overcome by enriching the mixture with hydrogen or by creating higher in-cylinder turbulence. However, there will be more heat losses when turbulence is increased (Karim et al. 1996); hence it is not a suitable technique to be used in a practical engine.

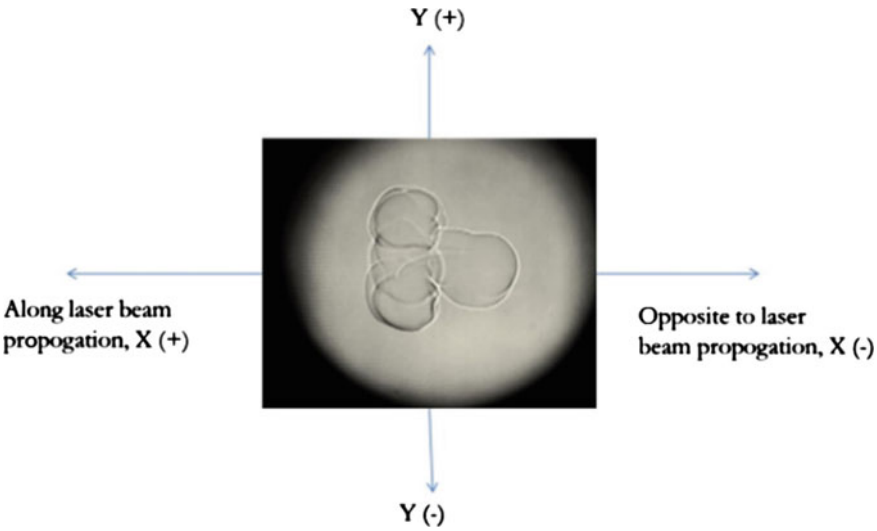

Fig. 10.9 Flame propagation of HCNG-air mixture in CVCC using laser ignition. (Prasad et al. 2017)

Prasad et al. (2017) used a constant volume combustion chamber (CVCC) to study the flame kernel evolution when ignited with laser plasma. They simulated the compression stroke engine condition in cylindrical shape CVCC of diameter 72 mm and length 220 mm. A Q-switched Nd: YAG laser (Litron; Nano L series) was employed at the fundamental wavelength (1064 mm) to ignite the combustible mixture with suitable optical arrangement. Shadowgraphy was done for analysing the flame kernel evolution, and temporal flame kernel growth was analyzed using the image analysis. Flame evolution was studied in two directions opposite to laser propagation and orthogonal to the laser beam, as shown in Fig. 10.9.

They captured images using shadowgraphy technique by employing a high-speed CCD camera operating at 54,000 fps, taking pictures at an interval of 18.5 μs with three different fuel-air equivalence ratio ($\lambda = 1.1, 1.3, 1.5$) and compared different mixtures of hydrogen enriched CNG mixtures filled at 5 bar and 10 bar initial chamber filling pressures (Fig. 10.10). Prasad et al. (2017) reported that instantly after the breakdown, asymmetric expansion of laser plasma with movement towards the optical element was faster than alongside the laser beam propagation path. Further, they reported that combustion duration increased with increasing λ for HCNG-air mixture and flame kernel evolution was faster for H_2 enriched mixtures for a particular λ and initial chamber condition, which led to reduced combustion duration. However, flame kernel evolution retarded when the initial chamber filling pressure increased to 10 bar while maintaining all other parameters identical. They also concluded that flame evolution speed decreased with increasing equivalence ratio.

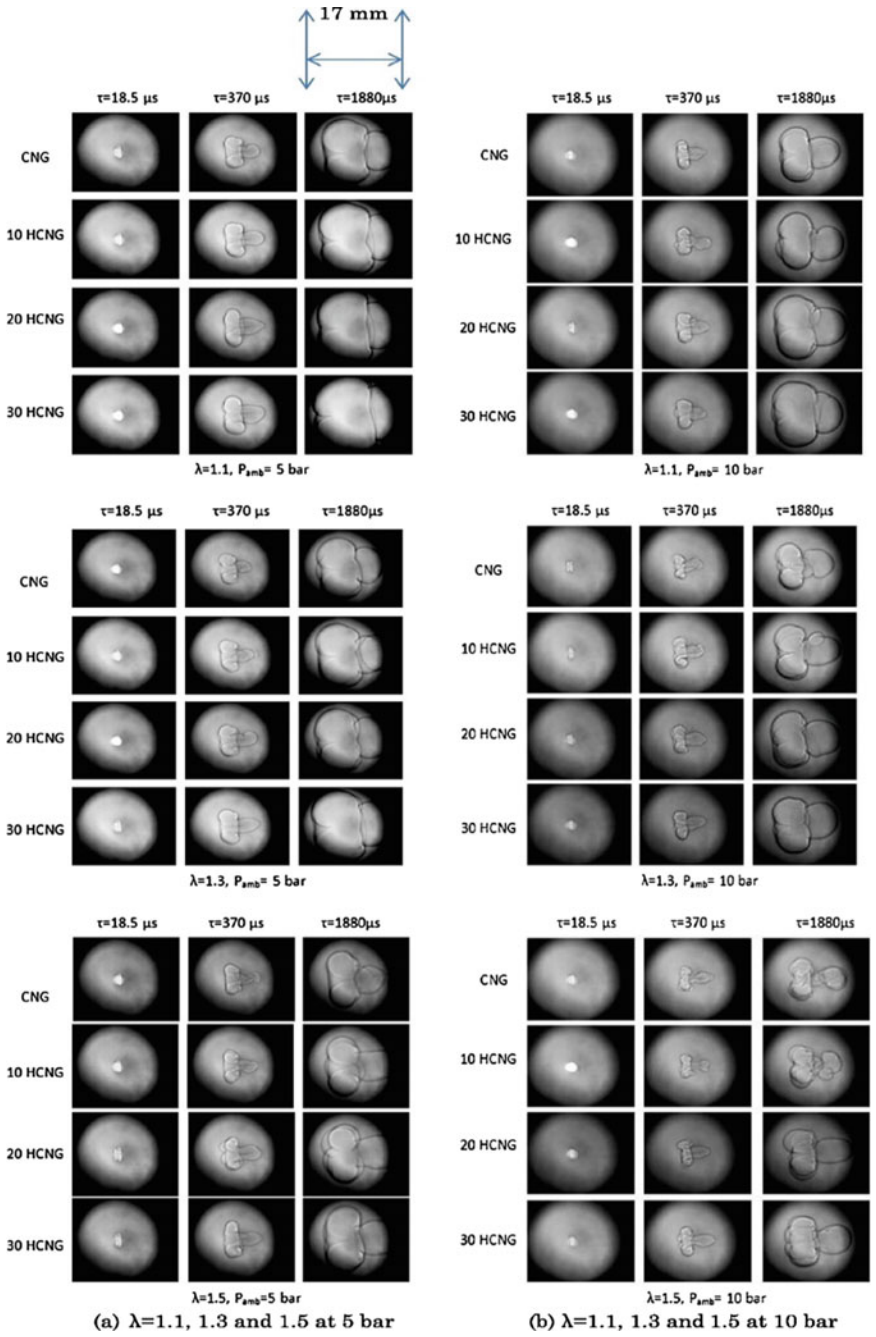

Fig. 10.10 Flame kernel evolution of HCNG air mixture using laser ignition (Prasad et al. 2017)

Case Study 2: On engine test with laser ignition

Mullet et al. (2009) performed a comparative analysis of LI system and electric SI system using gasoline for a multi-cylinder engine. They claimed that it was the first time, when all engine cylinders were ignited using laser spark (open beam path approach). They used two Nd: YAG solid state lasers operated at a fundamental wavelength of 1064 nm. They reported with LI, there is a reduction in coefficient of cyclic variations (CCV) and faster combustion for a range of loads, speeds and ignition timings and they were also able to ignite leaner fuel-air mixture more consistently compared to conventional SI system. Srivastava and Agarwal (2014) performed experiments using a single cylinder engine and reported higher peak cylinder pressure for LI compared to SI system. They varied the λ from 1.35 to 0.9 by keeping the ignition timing fixed at 25° bTDC for both LI and SI. They reported the highest flame speed for the slightly richer mixture ($\lambda \sim 0.9$), which decreased with further enrichment or leaning of the mixture. It can be observed from Fig. 10.11 that as λ decreased, differences in peak cylinder pressure between LI and SI decreased. At $\lambda = 1.2$ peak cylinder pressure for SI was 37.9 bar while for LI, it was 41.5 bar, as shown in Fig. 10.11. Hence they reported higher peak cylinder pressure for LI compared to conventional SI system.

10.7 Closure

In this chapter, potential of laser ignition system has been discussed. Furthermore, different ignition mechanisms by which the laser interacts with fuel-air mixture are explained briefly. Non-resonant breakdown mechanism was found to be the most suitable candidate for engine application since it does not require charge species characteristic wavelengths to resonate with laser wavelength. With the laser ignition system, one can ignite leaner charge, which is not possible to be ignited by conventional SI systems. This simultaneously enhances the engine efficiency and reduces engine-out NOx emissions. However for application of LI system in commercial engines, there is a need for further development of cheaper and compact solid-state lasers in addition to robust delivery system for laser beams. Different approaches have been discussed for laser beam delivery. Different type of multiplexer designs have also been discussed. At the end, couple of case studies of LI in CVCC and engine are also discussed.

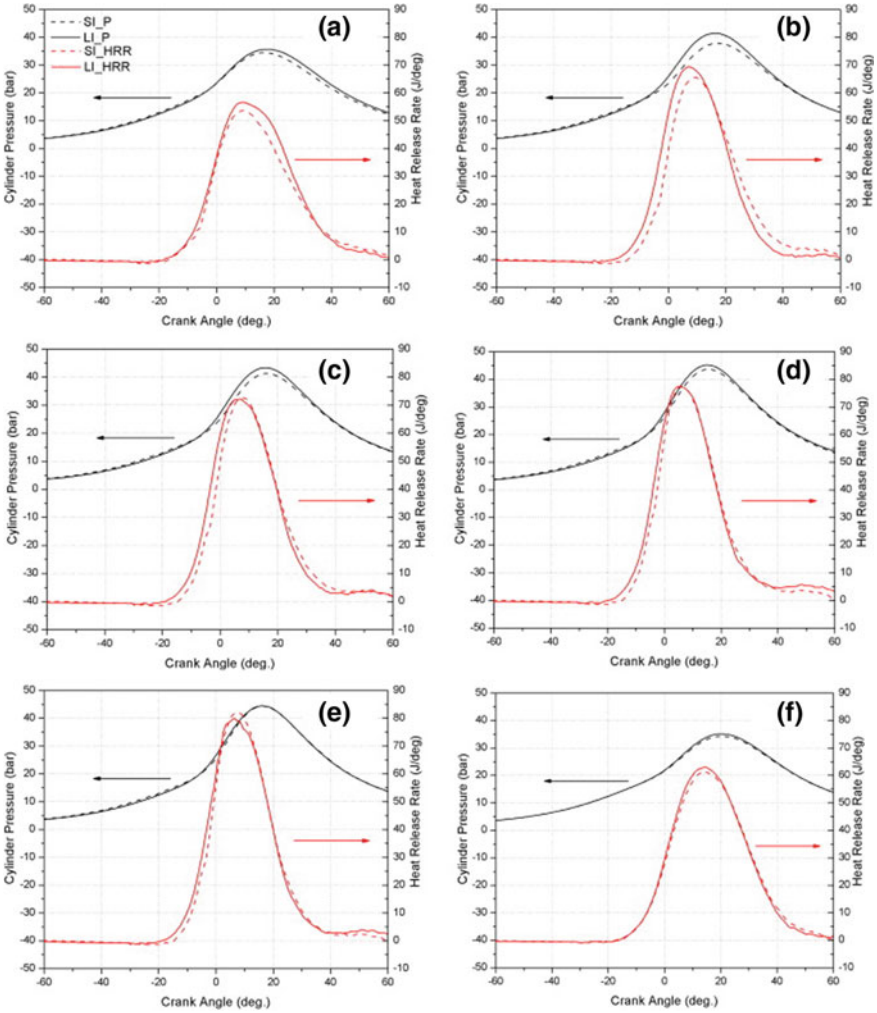

Fig. 10.11 Pressure and RoHR curve with Crank angle position for **a** $\lambda = 1.35$, **b** $\lambda = 1.2$, **c** $\lambda = 1.15$, **d** $\lambda = 1.10$, **e** $\lambda = 1.00$, and **f** $\lambda = 0.90$ at ignition timing of 25° bTDC. (Srivastava and Agarwal 2014)

References

Agarwal AK, Singh AP, Pal A (2017) Effect of laser parameters and compression ratio on particulate emissions from a laser ignited hydrogen engine. Int J Hydrogen Energy 42(15):10622–10635

Ahrens DL, Yalin AP, Olsen DB, Kim GH (2005) Development of an open path laser ignition system for a large bore natural gas engine: part 1—system design. In: ASME 2005 internal combustion engine division spring technical conference 2005 Jan 1, pp 489–498. American Society of Mechanical Engineers

Biruduganti MS, Gupta SB, Bihari B, Klett G, Sekar R (2004) Performance analysis of a natural gas generator using laser ignition. In: ASME 2004 internal combustion engine division fall technical conference 2004 Jan 1, pp 857–863. American Society of Mechanical Engineers
Bradley D, Sheppard CG, Suardjaja IM, Woolley R (2004) Fundamentals of high-energy spark ignition with lasers. Combust Flame 138(1–2):55–77
Dale JD, Smy PR, Clements RM (1978) Laser ignited internal combustion engine—an experimental study. SAE Transactions. 1:1539–1548
Dearden G, Shenton T (2013) Laser ignited engines: progress, challenges and prospects. Opt Express 21(106):A1113–A1125
Early JW, Lester CS (1999) Optical fiber switch. US Patent OCE, February. Patent number 6,351,579
Gili DH, Dougal AA (1965) Breakdown minima due to electron-impact ionization in super-high-pressure gases irradiated by a focused giant-pulse laser. Phys Rev Lett 15(22):845
Gregorčič P, Diaci J, Možina J (2013) Two-dimensional measurements of laser-induced breakdown in air by high-speed two-frame shadowgraphy. Appl Phys A 112(1):49–55
Herdin G, Klausner J, Wintner E, Weinrotter M, Graf J, Iskra K (2005) Laser ignition: a new concept to use and increase the potentials of gas engines. In: ASME 2005 internal combustion engine division fall technical conference 2005 Jan 1, pp 673–681. American Society of Mechanical Engineers
Inohara T, Ando A, Kido N (2009) Inventors; Denso Corp, Nippon Soken Inc, assignee. Laser ignition system. United States patent application US 12/264,280. 2009 May 28
Joshi S, Yalin AP, Galvanauskas A (2007) Use of hollow core fibers, fiber lasers, and photonic crystal fibers for spark delivery and laser ignition in gases. Appl Opt 46(19):4057–4064
Karim GA, Wierzba I, Al-Alousi Y (1996) Methane-hydrogen mixtures as fuels. Int J Hydrogen Energy 21(7):625–631
Knystautas R, Lee JH (1969) Laser spark ignition of chemically reactive gases. AIAA Journal. 7(2):312–317
Koechner W (1999) Solid-state laser engineering, vol 1. Springer
Kofler H, Tauer J, Tartar G, Iskra K, Klausner J, Herdin G, Wintner E (2007) An innovative solid-state laser for engine ignition. Laser Phys Lett 4(4):322–327
Kopecek H, Charareh S, Lackner M, Forsich C, Winter F, Klausner J, Herdin G, Weinrotter M, Wintner E (2005) Laser ignition of methane-air mixtures at high pressures and diagnostics. J Eng Gas Turbines Power 127(1):213–219
Kopecek H, Maier H, Reider G, Winter F, Wintner E (2003) Laser ignition of methane–air mixtures at high pressures. Exp Thermal Fluid Sci 27(4):499–503
Kroupa G, Franz G, Winkelhofer E (2009) Novel miniaturized high-energy Nd-YAG laser for spark ignition in internal combustion engines. Opt Eng 48(1):014202
Liedl G, Schuoecker D, Geringer B, Graf J, Klawatsch D, Lenz HP, Piock WF, Jetzinger M, Kapus P (2005) Laser-induced ignition of gasoline direct-injection engines. In: XV international symposium on gas flow, chemical lasers, and high-power lasers 2005 Mar 23, vol 5777, pp 955–961. International Society for Optics and Photonics
Matsuura Y, Hanamoto K, Sato S, Miyagi M (1998) Hollow-fiber delivery of high-power pulsed Nd: YAG laser light. Opt Lett 23(23):1858–1860
McMillian MH, Woodruff SD, Ontko JS, Richardson SW, McIntyre DL (2003) Laser-spark ignition for natural gas fueled reciprocating engines. In: Natural gas technologies conference and exposition, Orlando, Florida, Sept 2003 Oct
Mullett JD, Dearden G, Dodd R, Shenton AT, Triantos G, Watkins KG (2009) A comparative study of optical fibre types for application in a laser-induced ignition system. J Opt A Pure Appl Opt 11(5):054007
Pal A, Agarwal AK (2015) Effect of compression ratio on combustion, performance and emissions of a laser ignited single cylinder hydrogen engine. Int J Hydrogen Energy 40(36):12531–12540
Paschotta R (2008) Encyclopedia of laser physics and technology. Wiley. Electro-optic modulators. http://www.rp-photonics.com/electro_optic_modulators.html

Pavel N, Bärwinkel M, Heinz P, Brueggemann D, Dearden G, Croitoru G, Grigore OV (2018) Laser ignition-Spark plug development and application in reciprocating engines. Prog Quantum Electron 1(58):1–32

Phuoc TX (2000) Laser spark ignition: experimental determination of laser-induced breakdown thresholds of combustion gases. Optics Commun 175(4–6):419–423

Phuoc TX (2006) Laser-induced spark ignition fundamental and applications. Opt Lasers Eng 44(5):351–397

Prasad RK, Jain S, Verma G, Agarwal AK (2017) Laser ignition and flame kernel characterization of HCNG in a constant volume combustion chamber. Fuel 15(190):318–327

Radziemski LJ, Cremers D (1989) Laser-Induced plasmas and applications. Marcel Dekker Inc., New York

Reynolds A (2011) Development and testing of a multiplexing system for laser ignition of large bore natural gas engines. Master's Thesis, Colorado State University

Singh AP, Pal A, Gupta NK, Agarwal AK (2017) Particulate emissions from laser ignited and spark ignited hydrogen fueled engines. Int J Hydrogen Energy 42(24):15956–15965

Srivastava DK, Agarwal AK (2014) Comparative experimental evaluation of performance, combustion and emissions of laser ignition with conventional spark plug in a compressed natural gas fuelled single cylinder engine. Fuel 1(123):113–122

Srivastava DK, Wintner E, Agarwal AK (2014) Effect of focal size on the laser ignition of compressed natural gas–air mixture. Opt Lasers Eng 1(58):67–79

Stakhiv A, Gilber R, Kopecek H, Zheltikov AM, Wintner E (2004) Laser ignition of engines via optical fibers? Laser Phys 14(5):738–747

Thorlabs catalog: modular piezoelectric actuators. http://www.thorlabs.com/catalogPages/291.pdf

Turcu IC, Gower MC, Huntington P (1997) Measurement of KrF laser breakdown threshold in gases. Optics communications. 134(1–6):66–68

Weinrotter M, Iskra K, Al-Janabi AH, Kopecek H, Wintner E (2004–2005) Laser ignition of engines: multipoint, fiber delivery, and diagnostics. In Advanced laser technologies 2004–2005 Jun 7, vol 5850, pp 88–100. International Society for Optics and Photonics

Weinrotter M, Kopecek H, Tesch M, Wintner E, Lackner M, Winter F (2005) Laser ignition of ultra-lean methane/hydrogen/air mixtures at high temperature and pressure. Exp Thermal Fluid Sci 29(5):569–577

Wintner E, Kofler H (2005) Laser ignition for more than four decades: solutions and current problems. In: Laser Ignition Conference 2015 Apr 27, pp T5A-1. Optical Society of America

Yalin AP, DeFoort M, Willson B, Matsuura Y, Miyagi M (2005a) Use of hollow-core fibers to deliver nanosecond Nd: YAG laser pulses to form sparks in gases. Opt Lett 30(16):2083–2085

Yalin AP, Defoort MW, Joshi S, Olsen D, Willson B, Matsuura Y, Miyagi M (2005b) Laser ignition of natural gas engines using fiber delivery. In: ASME 2005 Internal Combustion Engine Division Fall Technical Conference 2005 Jan 1, pp 633–641. American Society of Mechanical Engineers

Yalin AP, Reynolds AR, Joshi S, Defoort MW, Willson B, Matsuura Y, Miyagi M (2006) Development of a fiber delivered laser ignition system for natural gas engines. In: ASME 2006 Internal Combustion Engine Division Spring Technical Conference 2006 Jan 1, pp 117–122. American Society of Mechanical Engineers